

**Finite element modeling of thermo-hydro-mechanical coupled processes in  
saturated and unsaturated frozen soils**

Emad Norouzi

A Thesis  
In the Department  
Of

Building, Civil and Environmental Engineering

Presented in Partial Fulfillment of the Requirements

for the Degree of

Doctor of Philosophy (Civil Engineering) at

Concordia University

Montréal, Québec, Canada

August 2024

© Emad Norouzi, 2024

**CONCORDIA UNIVERSITY  
SCHOOL OF GRADUATE STUDIES**

This is to certify that the thesis prepared

By: Emad Norouzi

Entitled: Finite element modeling of thermo-hydro-mechanical coupled processes in saturated and unsaturated frozen soils

and submitted in partial fulfillment of the requirements for the degree of

**Doctor of Philosophy (Civil Engineering)**

complies with the regulations of the University and meets the accepted standards with respect to originality and quality.

Signed by the final examining committee:

_____	Chair
Dr. Chunyan Lai	
_____	External Examiner
Dr. Agus Pulung Sasmito	
_____	Arm's Length Examiner
Dr. Sixu Deng	
_____	Examiner
Dr. Adel M. Hanna	
_____	Examiner
Dr. Ahmed Soliman	
_____	Thesis Supervisor
Dr. Biao Li	
_____	Thesis Supervisor
Dr. Emre Erkmen	

Approved by

2024-10-11 \_\_\_\_\_  
Date of Defence

\_\_\_\_\_  
Dr. Po-Han Chen, Graduate Program Director

\_\_\_\_\_  
Dr. Mourad Debbabi, Dean, Gina Cody School of Engineering and Computer Science

# Abstract

## **Finite element modeling of thermo-hydro-mechanical coupled processes in saturated and unsaturated frozen soils**

**Emad Norouzi, Ph.D.**

**Concordia University, 2024**

In line with the sustainable development of northern Canada, extensive construction activities are taking place in local communities where the ground is composed of clay deposits. With a changing climate, the clay soil is expected to undergo more freeze-thaw cycles. This degradation poses a major threat to newly constructed infrastructure. Since soil is an essential part of the built environment, it is crucial to understand its behavior under freezing and thawing conditions. This thesis presents a comprehensive study on the mechanical and thermal-hydro-mechanical (THM) behaviors of frozen soils, focusing on both theoretical developments and practical applications. To achieve this, the research pays close attention to the interface between the compounds. It introduces a stiffness interface parameter to define complex interactions between clay-water composites and non-clay minerals at different temperatures. The key contribution of using this parameter includes developing a numerical homogenization model with the eXtended Finite Element Method (XFEM) to estimate the elastic properties of frozen clay soils. Subsequently, considering the interface between air-water capillary pressure and cryosuction, a two-dimensional THM finite element model was developed using the Finite Element Method (FEM) to analyze the coupled processes in unsaturated freezing soils by incorporating temperature-dependent properties and phase changes. Finally, the behavior of permafrost under the operation of Ground Source Heat Pump

(GSHP) systems in thawing permafrost regions has been analyzed as part of a geo-energy and geological engineering project in the subarctic region of Umiujaq in northern Quebec.

The study begins with an extensive literature review to establish the current state of knowledge and identify gaps in existing research. It then details the development and validation of numerical models, including their application to real-world scenarios. The findings highlight the importance of considering imperfect bonds between soil components, the complex interaction between air-water capillary pressure and cryosuction, the influence of phase change-induced strain, and the benefits and challenges of using GSHP systems in cold climates.

Despite the significant advancements made, the research acknowledges several limitations, such as the need for more complex soil structure representations and broader validation efforts. Recommendations for future work emphasize enhancing model complexity, conducting long-term studies, and integrating field data to improve the accuracy and applicability of the models.

Overall, this thesis advances the understanding of frozen soil mechanics and provides valuable tools for engineering applications in Arctic and subarctic regions. It contributes to the development of sustainable and resilient solutions for climate adaptation.

**Keywords:** THM modelling of frozen Soil, Numerical Homogenization, Imperfect bound, Climate adaptation, Ground Source Heat Pump

## Acknowledgments

I would like to express my deepest gratitude to my primary supervisor, Professor Biao Li, for his unwavering support, invaluable guidance, and insightful advice throughout my PhD journey. His expertise and encouragement have been pivotal in shaping this work, and I am truly fortunate to have had the opportunity to learn from him.

I would also like to extend my sincere thanks to my second supervisor, Professor Emre Erkmen, for his thoughtful feedback, constructive criticism, and consistent support. His contributions have been instrumental in refining this research and ensuring its academic rigor. I want to acknowledge Professor Liangzhu Leon Wang for his supports.

Additionally, I am deeply grateful to my parents, whose love, patience, and sacrifices have been the foundation of my academic pursuits. Their belief in me has been a constant source of motivation. I would also like to thank my two brothers, Amir and Ehsan, for their unwavering encouragement and for always being there to provide support when I needed it the most. Their presence in my life has been a source of strength and inspiration.

I am also grateful to the members of our research group for their collaborative spirit, stimulating discussions, and the sense of camaraderie we have shared. Their perspectives and insights have enriched my research experience. Finally, my heartfelt thanks go to my friends, whose encouragement and companionship have been invaluable throughout this journey. Their support has helped me navigate the challenges of this academic endeavor.

I also would like to acknowledge the fund provided by NSERC Discovery Grant Canada (NO. RGPIN-2017-05169).

## Dedication

To my parents, whose unwavering love, support, and sacrifices have been the cornerstone of my success. Your belief in me has been my greatest source of strength and motivation.

To my brothers, Amir and Ehsan, for their constant encouragement, understanding, and companionship. Your presence in my life has made this journey not only possible but also meaningful.

Thank you for always being there for me.

## List of Publications

Refereed journal papers composing this thesis:

- **Norouzi, E.**, Li, B. Wang, L., Raymond, J., Gaur, A., and Zou, J., 2024. Numerical evaluation of ground source heat pumps in a thawing permafrost region. *Journal of Building Engineering*, 98, p.111035.  
<https://www.sciencedirect.com/science/article/pii/S2352710224026032>
- **Norouzi, E.**, Li, B. and Erkmen, R.E., 2024. Estimating equivalent elastic properties of frozen clay soils using an XFEM-based computational homogenization. *Cold Regions Science and Technology*, 226, p.104292.  
<https://www.sciencedirect.com/science/article/pii/S0165232X24001733>
- **Norouzi, E.**, Li, B., 2024 Finite element modeling of thermal-hydro-mechanical coupled processes in unsaturated freezing soils considering air-water capillary pressure and cryosuction. *Int J Numer Anal Methods Geomech*, 48, p.2944–2970.  
<https://doi.org/10.1002/nag.3761>

Other refereed journal papers published during the Ph.D. program

- **Norouzi, E.**, Li, B. and Erkmen, R.E., 2022. Modelling equivalent elastic properties of imperfectly bonded soil-rock mixtures using an XFEM-based computational homogenization. *Computers and Geotechnics*, 144, p.104638.
- Sojoudi, M., Li, B., **Norouzi, E.**, 2024. Thermal-hydro-mechanical modeling of short-term ground responses due to the borehole thermal energy storage operations in a Canadian subarctic region. *Renewable Energy*, 229, p.120753.
- Sojoudi, M., Li, B. and **Norouzi, E.**, 2024. Finite element modeling of thermo-hydro-mechanical coupled processes in clay soils considering bound water dehydration. *Acta Geotechnica*, pp.1-16. <https://doi.org/10.1007/s11440-024-02262-7>
- Li, B., **Norouzi, E.**, Zhu, H.H. and Wu, B., 2024. A thermo-poromechanical model for simulating freeze–thaw actions in unsaturated soils. *Advances in Water Resources*, 184, p.104624.

Conference proceedings papers and presentation:

- **Norouzi, E.**, Li, B., and Zhu, H.H. 2022, October. Thermo-hydro-mechanical coupled modelling of frost actions in unsaturated soils. In 75th Canadian Geotechnical Conference.
- **Norouzi, E.**, Li, B., and Raymond, J. 2022, June. Numerical modeling of thermo-hydro-mechanical processes related to geothermal heat pump operations in a subarctic climate. In 56th US Rock Mechanics/Geomechanics Symposium.
- **Norouzi, E.**, Li, B., and Erkmen, E.R. 2022, March. Numerical homogenization of anisotropic static elastic properties of soft mudrocks. In Geo-Conference 2022/American Society of Civil Engineers
- **Norouzi, E.**, Li, B., and Erkmen, E.R. 2021, September. On the subsidence of a geothermal energy storage ground due to seasonal freezing and thawing in a subarctic region. In 74th Canadian Geotechnical Conference.
- **Norouzi, E.**, Li, B., and Erkmen, E.R. 2021, June. Computational homogenization to identify elastic properties of soil-rock mixtures at normal and freezing temperatures. In 55th US Rock Mechanics/Geomechanics Symposium.

## Contribution of Authors

The content of this thesis reflects the author's unique and independent contributions to the research.

The candidate took primary responsibility for model formulation, Finite Element Method (FEM) implementation, and the development of innovative enhancements. These tasks were carried out under the close guidance and supervision of Professor Biao Li.

In Chapter 3, the formulation and coding of numerical homogenization is supported by Professor Emre Erkmen.

In Chapter 5, the data regarding air temperatures in Umiujaq was provided by Professor Liangzhu (Leon) Wang from Concordia University, Abshieck Gaur from NRC Canada, and Dr. Jiwei Zou, a Postdoctoral Fellow at Concordia University. Additionally, the design of the Ground Source Heat Pump (GSHP) system was conducted under the close guidance of Professor Jasmine Reymond from INRS.

All authors have reviewed and approved the final manuscript.

# Table of Contents

Abstract.....	iii
Acknowledgments.....	v
Dedication.....	vi
List of Publications.....	vii
Contribution of Authors.....	ix
Table of Contents.....	x
List of Figures.....	xvi
List of Tables.....	xxii
Chapter 1.....	1
1 Introduction.....	1
1.1 Context and Inspiration for the Study.....	1
1.2 Objectives and scope.....	4
1.3 Original contribution.....	6
1.3.1 Numerical Homogenization Model:.....	7
1.3.2 Multidimensional THM Analysis:.....	7
1.3.3 Integration of Plasticity Models:.....	7
1.4 Thesis organization.....	7
Chapter 2.....	9
2 Literature review.....	9
2.1 Introduction.....	9
2.2 Mechanical properties of frozen clay soil at different temperatures.....	9
2.3 Computational homogenization.....	10

2.4	Thermo-Hydro-Mechanical behavior of frozen soil .....	12
2.5	Numerical simulation of frozen soil .....	13
2.6	Climate change and permafrost degradation in north of Quebec .....	18
2.7	Application of Ground Source Heat Pump in permafrost region .....	19
2.8	Summary .....	20
	Preface to Chapter 3 .....	22
	Chapter 3 .....	23
3	Estimating equivalent elastic properties of frozen clay soils using an XFEM-based computational homogenization .....	23
3.1	Abstract .....	23
3.2	Introduction .....	25
3.3	Basic physical properties .....	28
3.4	Analytical homogenization methods .....	29
3.5	Numerical homogenization .....	31
3.5.1	Equilibrium of a deformable body .....	31
3.5.2	The first order of homogenization .....	32
3.5.3	The variational setting for homogenization .....	34
3.5.4	REV boundary value problem .....	35
3.6	Verification and numerical simulations .....	37
3.6.1	Model verification .....	37
3.6.2	Mechanical properties of artificial frozen sandy clay soils .....	39
3.7	Discussion .....	45
3.7.1	Higher volumetric fraction of non-clay materials .....	45
3.7.2	Comparison with other analytical and numerical solutions .....	46
3.7.3	Randomly generated models .....	48

3.7.4	Limitations .....	52
3.8	Conclusions.....	53
	Preface to Chapter 4.....	55
	Chapter 4.....	56
4	Finite element modeling of thermal-hydro-mechanical coupled processes in unsaturated freezing soils considering air-water capillary pressure and cryosuction. ....	56
4.1	Abstract.....	56
4.2	Introduction.....	58
4.3	Mathematical models of unsaturated frozen medium.....	62
4.3.1	Volumetric relation .....	63
4.3.2	Capillary pressure .....	64
4.3.3	SWCC and SFCC.....	65
4.3.4	Darcy's law .....	68
4.3.5	Fick's law .....	69
4.3.6	Fourier's law .....	69
4.3.7	Material nonlinearity.....	70
4.3.8	Elasticity in a partially saturated frozen soil.....	71
4.4	Balance equations .....	71
4.4.1	Linear momentum balance equation.....	72
4.4.2	Mass balance equations.....	72
4.4.3	Energy balance equation .....	74
4.5	Variational formulations .....	74
4.6	FEM implementation .....	79
4.6.1	Spatial discretization.....	79
4.6.2	Temporal discretization .....	80

4.7 Numerical verification .....	82
4.8 Discussions .....	88
4.8.1 Effect of phase change strain .....	88
4.8.2 Pore pressure variations .....	90
4.8.3 Freezing induced plastic strain.....	92
4.8.4 Limitations .....	94
4.9 Conclusions.....	95
Preface to Chapter 5.....	103
Chapter 5.....	104
5 Numerical evaluation of ground source heat pumps in a thawing permafrost region .....	104
5.1 Abstract.....	104
5.2 Introduction.....	105
5.3 THM model of saturated frozen soil.....	110
5.3.1 Conservation of mass .....	111
5.3.2 Conservation of energy .....	112
5.3.3 Conservation of linear momentum.....	113
5.3.4 Spatial and time discretization .....	115
5.4 Validation of the numerical tool .....	116
5.5 FEM modeling of a GSHP well in Umiujaq.....	119
5.5.1 Model description .....	120
5.5.2 Mesh sensitivity analysis .....	125
5.5.3 Temperature variations .....	127
5.5.4 Pore water pressure distributions .....	128
5.5.5 Ice saturation variations .....	130
5.5.6 Ground subsidence.....	132

5.6	Discussions .....	133
5.6.1	Effect of GSHP operation on the ground subsidence .....	133
5.6.2	Effect of GSHP running time on ground subsidence.....	136
5.6.3	Limitations .....	140
5.7	Conclusions.....	142
Chapter 6	.....	145
6	Conclusions, limitations, and recommendations for future work .....	145
6.1	Conclusion .....	145
6.1.1	Estimating Equivalent Elastic Properties of Frozen Clay Soils Using an XFEM-Based Computational Homogenization (Chapter 3):.....	145
6.1.2	Finite Element Modeling of Thermal-Hydro-Mechanical Coupled Processes in Unsaturated Freezing Soils Considering Air-Water Capillary Pressure and Cryosuction (Chapter 4):.....	146
6.1.3	Numerical Evaluation of Using Ground Source Heat Pump for Renewable Energy Generation and Climate Adaptation in a Thawing Permafrost Region (Chapter 5): .....	146
6.2	Limitations .....	146
6.2.1	Simplified Models:.....	147
6.2.2	Scope of Validation: .....	147
6.2.3	Geographical and Temporal Constraints: .....	147
6.3	Recommendations for Future Work.....	147
6.3.1	Enhanced Model Complexity: .....	148
6.3.2	Broader Validation Efforts:.....	148
6.3.3	Exploration of Dynamic Temperature Management: .....	148
6.3.4	Regional and Long-Term Studies: .....	148
6.3.5	Interfacial and Micromechanical Investigations: .....	149
6.3.6	Integration of Field Data:.....	149

6.3.7 Development of User-Friendly Simulation Tools: .....	149
Bibliography .....	151

## List of Figures

Figure 1-1 Construction issue in permafrost regions due to degradation ( <a href="#">Hjort et al., 2022</a> ). .....	2
Figure 1-2 (a) Settlement of permafrost due to thawing ( <a href="#">Hjort et al., 2022</a> ) and (b) installation of GSHP in subarctic region.....	3
Figure 1-3 (a) Schematic model of saturated frozen soil at micro-scale ( <a href="#">Bekele et al; 2017</a> ) (b) Heat, liquid, water, and air movement in a schematic unsaturated frozen soil ( <a href="#">Li et al; 2021</a> ). ....	4
Figure 1-4 Flow chart showing the contribution of the thesis. ....	6
Figure 2-1 Numerical homogenization procedure ( <a href="#">Meng et al., 2018</a> ) .....	11
Figure 2-2 Comparison between numerical simulations and experimental data (Peng et al. 2016) .....	15
Figure 2-3 Results of simulation of <a href="#">Bai et al., (2020)</a> : (a) total volumetric water content at the end of the experiment and (b) frost heave with different values of effective strain ratio.....	17
Figure 3-1 Representation of slow and fast coordinates in a heterogeneous framework: (a) a sample, (b) a REV at the micro-scale model, and (c) a REV converted to the fast coordinate, after <a href="#">Norouzi et al. (2022)</a> .....	33
Figure 3-2 The flowchart of the proposed comprehensive numerical approach for estimating elastic properties of frozen clay soils. ....	37

Figure 3-3 Elastic modulus of soil-rock mixtures: comparison between analytical and numerical methods for (a) normal and (b) freezing temperatures. ....	39
Figure 3-4 Elastic modulus and Poisson’s ratio of (a) Kaolinite-sand, and (b) Bentonite-sand, data is from Girgis et al. (2020).....	41
Figure 3-5 The inversion algorithm to find elastic properties of clay-water composites using DEM, modified after (Li and Wong, 2017). ....	42
Figure 3-6 Inversion algorithm: Using DEM method to find the elastic properties of (a) Kaolinite-sand and (b) Bentonite-sand versus temperature .....	43
Figure 3-7 Numerical meshing of REV’s employed in current numerical homogenization method: (a) Kaolinite-sand and (b) Bentonite-sand .....	44
Figure 3-8 Calibrated interface stiffness parameter versus temperature (a) Kaolinite-sand and (b) Bentonite-sand .....	45
Figure 3-9 Elastic properties of Kaolinite-sand at selected temperatures with different volume fractions of clay-water composites for the cases with (a) 1 mm/min and (b) 9mm/min loading .	46
Figure 3-10 Elastic properties of Bentonite-sand at selected temperatures with different volume fractions of clay-water composites for the cases with (a) 1 mm/min and (b) 9mm/min loading .	46
Figure 3-11 Modeling of elastic modulus of Kaolinite-sand at $T = -0.5\text{ }^{\circ}\text{C}$ (first row) and $T = -15\text{ }^{\circ}\text{C}$ (second row) with different volume fraction of clay-water composites: Comparison of modeled elastic modulus between Reuss, DEM, Rigid bond, and XFEM for the cases with (a) 1 mm/min and (b) 9mm/min loading.....	48

Figure 3-12 Modeling of elastic modulus of Bentonite-sand at  $T = -0.5\text{ }^{\circ}\text{C}$  (first row) and  $T = -15\text{ }^{\circ}\text{C}$  (second row) with different volume fraction of clay-water composites: Comparison of modeled elastic modulus between Reuss, DEM, Rigid bond, and XFEM for the cases with (a) 1 mm/min and (b) 9mm/min loading..... 48

Figure 3-13 Numerical meshing of REV's with randomly generated of Kaolinite-sand with  $f_{nc}=0.27$  with (a) 14, (b) 15, (c) 13 inclusions and Bentonite-sand with  $f_{nc}=0.18$  with (d) 9, (e) 10, (f) 11 inclusions. .... 49

Figure 3-14 The von Misses stress contours of sample (c) of Kaolinite-sand at (a)  $T = -0.5\text{ }^{\circ}\text{C}$ , (b)  $T = -5\text{ }^{\circ}\text{C}$ , (c)  $T = -10\text{ }^{\circ}\text{C}$ , and (d)  $T = -15\text{ }^{\circ}\text{C}$  in horizontal direction and (e)  $T = -0.5\text{ }^{\circ}\text{C}$ , (f)  $T = -5\text{ }^{\circ}\text{C}$ , (g)  $T = -10\text{ }^{\circ}\text{C}$ , and (h)  $T = -15\text{ }^{\circ}\text{C}$  in vertical direction with imperfect bonding between matrix and inclusions..... 51

Figure 3-15 The von Misses stress contours of sample (c) of Kaolinite-sand at (a)  $T = -0.5\text{ }^{\circ}\text{C}$ , (b)  $T = -5\text{ }^{\circ}\text{C}$ , (c)  $T = -10\text{ }^{\circ}\text{C}$ , and (d)  $T = -15\text{ }^{\circ}\text{C}$  in horizontal direction and (e)  $T = -0.5\text{ }^{\circ}\text{C}$ , (f)  $T = -5\text{ }^{\circ}\text{C}$ , (g)  $T = -10\text{ }^{\circ}\text{C}$ , and (h)  $T = -15\text{ }^{\circ}\text{C}$  in vertical direction with rigid bonding between matrix and inclusions. .... 52

Figure 4-1 Sketch showing the configuration of different phases of an unsaturated frozen soil.. 63

Figure 4-2 Sketch showing the problem domain and boundary conditions with primary variables (modified after (Khoei and Mortazavi, (2020))). ..... 75

Figure 4-3 FEM mesh and boundary conditions of both ends for the numerical test..... 83

Figure 4-4 Simulated temperature evolvments at different heights (measured data is from <a href="#">Bai et al., (2020)</a> .....	85
Figure 4-5 Simulated and measured total volumetric water contents at the end of the test ( $t = 100$ hrs) (measured data is from <a href="#">Bai et al., (2020)</a> ). .....	86
Figure 4-6 Simulated contours of total volumetric water contents at: (a) initial condition, (b) $t = 10$ hrs, (c) $t = 25$ hrs, (d) $t = 50$ hrs, (e) $t = 75$ hrs, and (f) $t = 100$ hrs. ....	86
Figure 4-7 Plots showing the profile developments of total water content, air content, and ice content.....	87
Figure 4-8 Simulated and measured frost heave developments with time (measured data is from <a href="#">Bai et al., (2020)</a> ). .....	88
Figure 4-9 Simulated porosity contours at the end of numerical tests: (a) with phase change strain, (b) without phase change strain ( $t = 100$ hrs). ....	89
Figure 4-10 Simulated pore pressure and freezing temperature point profiles at different times of the numerical test: (a) total pore pressure, (b) vapor pressure, (c) dry air pressure, (d) freezing temperature point. ....	91
Figure 4-11 Simulated pore pressure development at three key monitoring points (height = 2 cm, 5 cm, and 8 cm).....	92
Figure 4-12 Simulated von Mises equivalent plastic strain contours at: at: (a) initial condition, (b) $t = 10$ hrs, (c) $t = 25$ hrs, (d) $t = 50$ hrs, (e) $t = 75$ hrs, and (f) $t = 100$ hrs. ....	93

Figure 4-13 Simulated effective stress paths and accumulated plastic strains at the three key points. .....	93
Figure 5-1 Schematic of a ground source heat pump system in a discontinuous permafrost region. .....	106
Figure 5-2 The numerical mesh and boundary conditions of the numerical test for validation.	117
Figure 5-3 Comparison of simulated and experimental data for the freezing test. ....	119
Figure 5-4 (a) Schematic representation of the 2D model used for investigating the ground response of a GSHP system in Umiujaq and (b) a cross section of a borehole heat exchanger.	121
Figure 5-5 (a) Maximum, minimum, and mean measured air temperatures in Umiujaq and (b) temperature variations of air and GHE in the current simulation. ....	123
Figure 5-6 Calibration of the SFCC model parameters based on lab data.....	124
Figure 5-7 The selected FEM mesh and monitoring points for numerical analysis. ....	126
Figure 5-8 Curves showing the mesh sensitivity analysis results: (a) the displacement around borehole (P1), and (b) the temperature at the right edge with a depth of 3 m (P6). ....	126
Figure 5-9 Simulated temperature (°C) contours over selected time frames within two years. .	128
Figure 5-10 Water pressure distribution contours over selected time frames within two years.	130
Figure 5-11 Simulated ice saturation over selected time frames within two years .....	131
Figure 5-12 Ground subsidence contours over selected time frames within two years.....	133

Figure 5-13 Displacement data for the three monitoring points: (a) P2, (b) P3, (c) P4, and (d) P5 over the two years, with and without GSHP operation..... 134

Figure 5-14 Comparison between the accumulated plastic strain of the model at the end of the simulation (a) with GSHP operation, and (b) without GSHP operation..... 136

Figure 5-15 Displacement data for monitoring points: (a) P2, (b) P3, (c) P4, and (d) P5 over the two years under three scenarios: with GSHP operation for 10 months, without GSHP operation, and with GSHP temperature kept constant at -5 °C..... 138

Figure 5-16 Simulated displacement rates at monitoring points: (a) P2, (b) P3, (c) P4, and (d) P5 over two years under three different scenarios. .... 139

## List of Tables

Table 3-1 Elastic properties of soil, rock and interface stiffness parameter applied to current numerical model.....	38
Table 3-2 Kaolinite-sand and Bentonite-sand: Experimental setup and properties.....	40
Table 3-3 Volumetric and elastic properties of non-clay minerals, applied to DEM.....	42
Table 3-4 The results of simulated elastic properties of Kaolinite-sand with randomly generated inclusions in xx and yy directions and absolute error ratio with respect to experimental data at different temperatures .....	50
Table 3-5 The results of simulated elastic properties of Bentonite-sand with randomly generated inclusions in xx and yy directions and absolute error ratio with respect to experimental data at different temperatures .....	50
Table 4-1 Material properties for the unsaturated soil in the 1D freezing (Bai et al., 2020).....	84
Table 5-1 Thermal, hydraulic, and mechanical properties of the numerical THM model. ....	117
Table 5-2 Thermal and hydraulic propeties of the current simulation.....	124
Table 5-3 Temperature-dependent mechanical parameters of geomaterials used in the modeling at the Umiujaq site. ....	125

# Chapter 1

## 1 Introduction

### 1.1 Context and Inspiration for the Study

During the ground freezing process, the freezing front gradually penetrates downward into the soil. Frost heave can occur due to the volumetric expansion caused by the water-ice phase change and the formation of ice lenses. Frost heave is a common cause of engineering disasters in cold regions, such as pipe ruptures and foundation damage. Upon ground thawing, geo-disasters like significant ground settlements or landslides may be triggered.

Recently, there has been an increase in construction projects in frozen layers, including natural foundations, highways, and railways. Additionally, the application of artificial ground freezing (AGF) in mining and tunneling engineering has become more widespread (Xu et al., 2019). Many construction issues have been observed during and after the construction process due to the deformation of the frozen medium. Recent studies have shown that the freeze-thaw process severely damages infrastructure in cold regions (Na and Sun, 2017). As an example, Figure 1-1 shows a runway and taxiways at Iqaluit international airport cracked and warped due to permafrost thaw.



Figure 1-1 Construction issue in permafrost regions due to degradation (Hjort et al., 2022).

Canada is one of the UN countries that are taking decarbonization actions to achieve the Sustainable Development Goals by 2030. Additionally, new infrastructure needs are arising in permafrost regions that are experiencing thermal impacts due to climate change. Thermo-hydro-mechanical (THM) responses of ground soils are heavily involved in these projects. For example, the applications of Borehole Thermal Energy Storage (BTES) and Ground Source Heat Pumps (GSHP) have increased recently. These are recognized as renewable energy storage solutions. Given that solar energy is insufficient during winter, BTES and GSHP systems are suggested in subarctic regions as an alternative way to store energy during summer and provide it in winter. Quebec has a significant opportunity to utilize BTES and GSHP systems for both electricity and heating, reducing the need to ship fuel by boat and replacing fossil fuels (Gunawan et al., 2020). Figure 1-2 schematically depicts the installation of GSHP in a vertical orientation within a subarctic region.

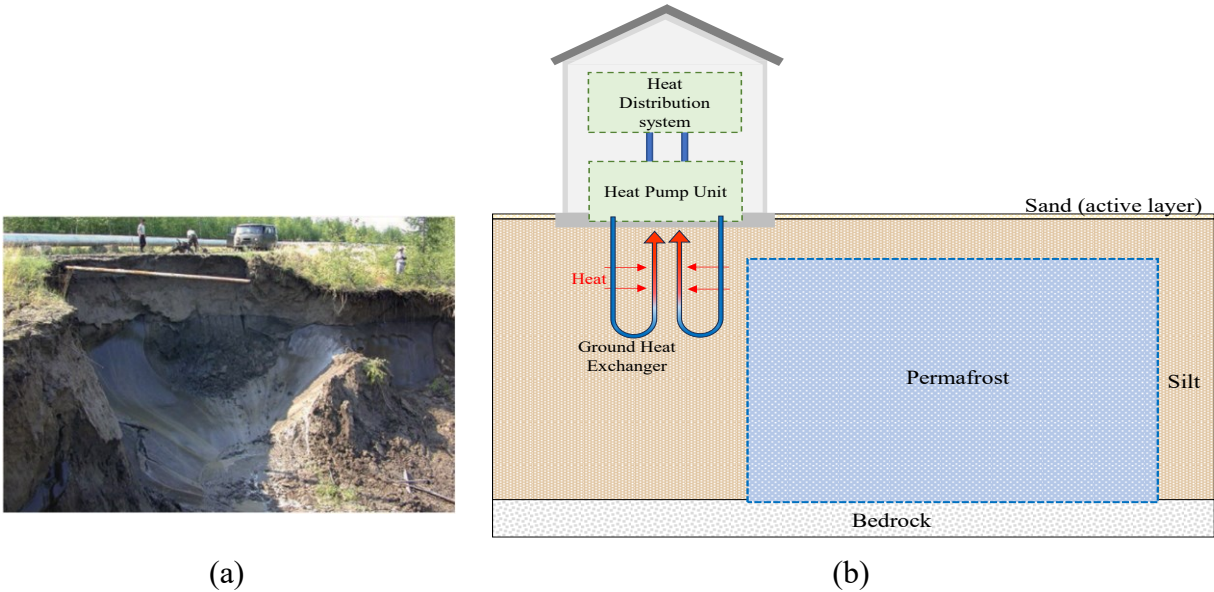


Figure 1-2 (a) Settlement of permafrost due to thawing (Hjort et al., 2022) and (b) installation of GSHP in subarctic region

Currently, there is a lack of comprehensive and inclusive numerical modeling tools to simulate large-scale THM processes in saturated and unsaturated frozen soils. Engineering designs often rely on oversimplified assumptions, which can underestimate related geo-risks. Reliable models are needed to accurately quantify freeze-thaw actions in soils, which are porous media containing solid soil particles, ice, liquid water, and air. There is also a high demand for quantitative models to characterize the evolution of Arctic tundra hydrology and its impact on Arctic ecosystems. Therefore, understanding the behavior of frozen soil is essential.

Frozen soils are composed of soil particles, water, ice, and air. They naturally occur in the seasonal frozen and permafrost layers of Arctic and subarctic regions, as well as in loess sediments. Regions such as Siberia, Canada, Greenland, Antarctica, and Alaska, located in the Northern and Southern Hemispheres, experience prolonged freezing temperatures (Kadivar and Manahiloh, 2019). Additionally, the use of artificial ground freezing in civil and mining projects has recently increased to control ground and groundwater movement. Frozen soils are generally classified as

either saturated (in the absence of air) or unsaturated (when air is present in the medium) (Figure 1-3).

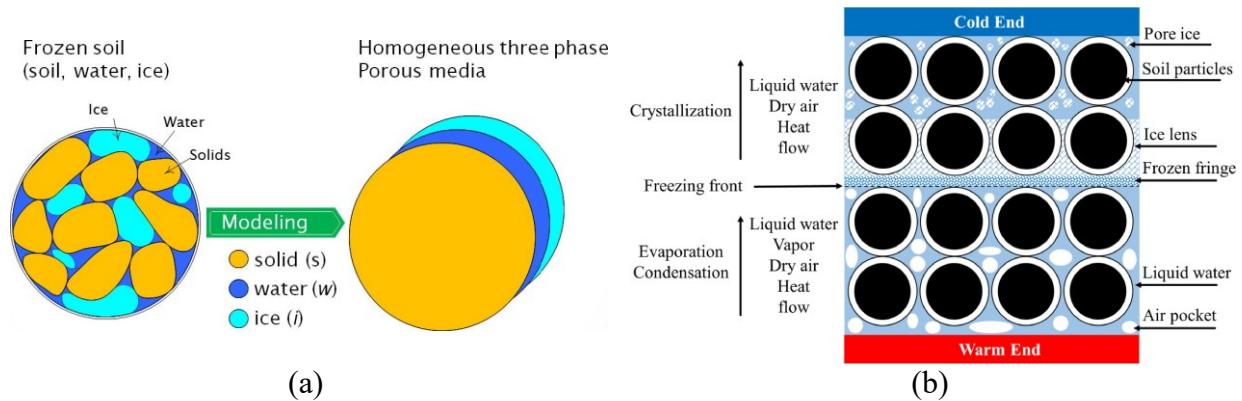


Figure 1-3 (a) Schematic model of saturated frozen soil at micro-scale (Bekele et al; 2017) (b) Heat, liquid, water, and air movement in a schematic unsaturated frozen soil (Li et al; 2021).

The hydro-mechanical behavior of both saturated and unsaturated frozen soils under varying temperatures and with different volumetric contents has been studied from various perspectives. Given that frozen soils are heterogeneous materials with varying volume ratios of their components and different temperatures, their mechanical behavior can change significantly. This study aims to introduce new methodologies to create numerical models of frozen soil compounds with different volumetric contents of soil, water, ice, and air under varying temperatures.

## 1.2 Objectives and scope

This study aims to address the following issues:

- 1- Existing methods to estimate the mechanical properties of frozen soil typically average the mechanical properties of the components. This study proposes developing a numerical homogenization model to evaluate the temperature-dependent properties of frozen soils by considering the flexible interactions between the components at the meso-scale. The goal is to create a more accurate model at the macro-scale.

- 2- Develop a two-dimensional fully coupled THM numerical analysis based on a finite element framework to investigate the geo-risk of ground subsidence due to cyclic freeze-thaw action in saturated and unsaturated porous media. Fully saturated and unsaturated frozen soil simulations have often been based on biaxial models, particularly in the modeling of unsaturated and shallow soils, which is currently limited to 1-D simulations. It is necessary to create multidimensional THM models incorporating phase changes to study real investigation sites.
- 3- By including a plasticity model with calibrated parameters from experimental data, the model can be extended to a general one, particularly for frozen conditions. Hardening parameters, which are functions of pressure and temperature, should be added to the numerical THM model.
- 4- After verifying the developed numerical THM model with experimental data, it can be used to simulate geo-engineering projects in cold regions. By employing field data, the model can investigate temperature variations, water movement, volumetric ice content, and the deformation of the medium.
- 5- Finally, based on previous objective, a numerical simulation of operation of GSHP in cold regions has been conducted to study the application to a geo-energy and geological engineering project in Arctic and subarctic regions. [Figure 1-4](#) illustrates the flowchart of the proposed method in this thesis.

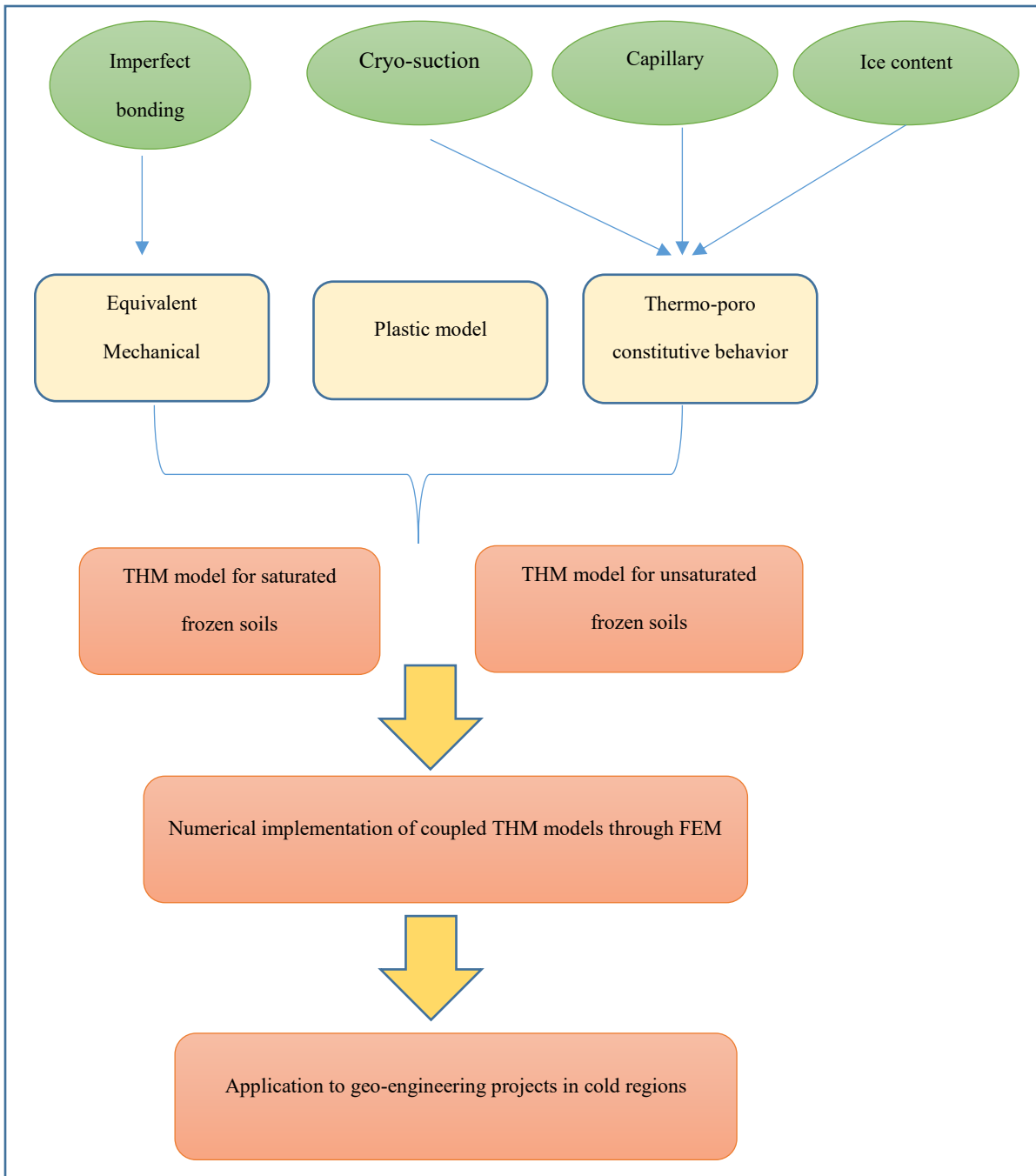


Figure 1-4 Flow chart showing the contribution of the thesis.

### 1.3 Original contribution

This research introduces several original contributions to the field of frozen soil mechanics and its application in geo-engineering:

### **1.3.1 Numerical Homogenization Model:**

Development of a novel numerical homogenization model that evaluates the temperature-dependent properties of frozen soils. This model considers the flexible interactions between the soil, water, ice, and air components at the meso-scale, providing a more accurate representation at the macro-scale compared to traditional averaging methods.

### **1.3.2 Multidimensional THM Analysis:**

Creation of a two-dimensional fully coupled thermo-hydro-mechanical (THM) numerical analysis framework. This framework incorporates the effects of cyclic freeze-thaw actions on ground subsidence in both saturated and unsaturated porous media, overcoming the limitations of current biaxial and 1-D models.

### **1.3.3 Integration of Plasticity Models:**

Inclusion of a plasticity model with calibrated parameters from experimental data, specifically designed to address the unique conditions of frozen soils. The model integrates hardening parameters that are functions of pressure and temperature, enhancing the accuracy and applicability of the numerical THM model.

## **1.4 Thesis organization**

This thesis follows a manuscript-based format, with three of the six chapters comprising journal article manuscripts that have either been published or under review, as detailed in the list of publications. With the exclusion of this particular chapter, the thesis is structured in the subsequent manner:

Chapter 2 provides a comprehensive review of the current literature, delineating the specific challenges at hand and delineating suggested analytical and numerical approaches for resolution.

Chapter 3 explores the development of a novel approach to estimate the elastic properties of frozen clay soils by integrating analytical and numerical models. It highlights the critical impact of inclusion volume fraction on the accuracy of elastic property estimation.

Chapter 4 of the thesis presents a comprehensive computational model for analyzing THM coupled processes in unsaturated porous media under frost actions. The model's robustness is demonstrated through validation against experimental data.

Moving on to chapter 5, it evaluates the potential of Ground Source Heat Pump systems to mitigate ground subsidence in thawing permafrost areas. The study focuses on the interactions between thermal regulation and ground stability.

Finally, Chapter 6 synthesizes the key findings of the research, identifies the limitations encountered, and provides recommendations for future work to enhance the understanding and modeling of frozen soils.

## Chapter 2

### 2 Literature review

#### 2.1 Introduction

In this section, a comprehensive review of existing literature on the behavior and applications of frozen clay soil is provided. By examining various aspects of frozen soil research, this section aims to establish a solid foundation for understanding the complexities involved in studying and utilizing frozen soils, especially in the context of climate change and engineering applications.

#### 2.2 Mechanical properties of frozen clay soil at different temperatures

Frozen clay soils, distinguished by their heterogeneous composition of clay-water composites and non-clay minerals, display significant sensitivity to temperature and the applied load conditions. A comprehensive understanding of the mechanical behaviors of frozen clay soils is essential in the investigation of geological disasters such as permafrost slumps, infrastructure damage due to seasonal freeze-thaw actions, or engineering projects related to artificial ground freezing (An et al., 2022; Andersland and Ladanyi, 2013; Girgis, 2019; Li et al., 2024; Ma et al., 2023; S. Wang et al., 2016).

Previous research has involved extensive experimental studies to investigate the mechanical responses of frozen clay soils under various temperature and loading rate conditions (Girgis et al., 2020; Li and Akhtar, 2022). These studies have summarized laboratory data to establish empirical temperature-dependent mechanical property relations for frozen soils (Li et al., 2004; Ma et al., 2017; Shi et al., 2023; Zhu et al., 2020). For example, Xu et al., (2017) conducted uniaxial

compressive tests on saturated frozen Helin loess, covering five distinct strain rates and four different temperatures, to examine the influence of temperature and strain rate on the mechanical properties of frozen loess.

Furthermore, [Girgis et al., \(2020\)](#) conducted laboratory tests on two artificial frozen clay soils to gauge the rate dependency of uniaxial axial compressive behavior at temperatures ranging from  $-15^{\circ}\text{C}$  to  $0^{\circ}\text{C}$ . These studies highlight the marked influence of minerals, void ratio, stress history, and pore fluid salinity on the rate-dependent uniaxial compressive behavior of frozen clay soil. The temperature-dependent uniaxial compressive mechanical properties were measured and modeled using empirical relations, exhibiting a high dependency on the applied deformation rate.

### **2.3 Computational homogenization**

Achieving a comprehensive understanding of the rate-dependent behavior of frozen clay soils and its correlation with temperature necessitates a significant number of specimens with similar compositions and microstructures. However, obtaining in-situ frozen clay soil samples involves sophisticated procedures and challenges, delaying theoretical studies of their behavior. Laboratory tests offer limited characterization results, and uncertainties persist regarding the intrinsic anisotropic properties of samples with varying clay fractions. Understanding how these properties change with different clay fractions is crucial. Recently, researchers have turned to homogenization methods to determine the equivalent properties of heterogeneous mediums like frozen soils by dividing the composite material into multiple scales. Various endeavors, guided by homogenization theory, have been made to model the behavior of frozen soils ([Chang et al., 2019](#); [Zhang et al., 2019](#); [Zhou and Meschke, 2018](#)). Furthermore, numerical homogenization offers insight into the mechanical behavior of materials by assuming periodicity. This method involves representing a Representative Elementary Volume (REV), containing micro-level properties,

throughout the heterogeneous material at the macro level. Figure 2-1 schematically shows the homogenization procedure of a heterogeneous material.

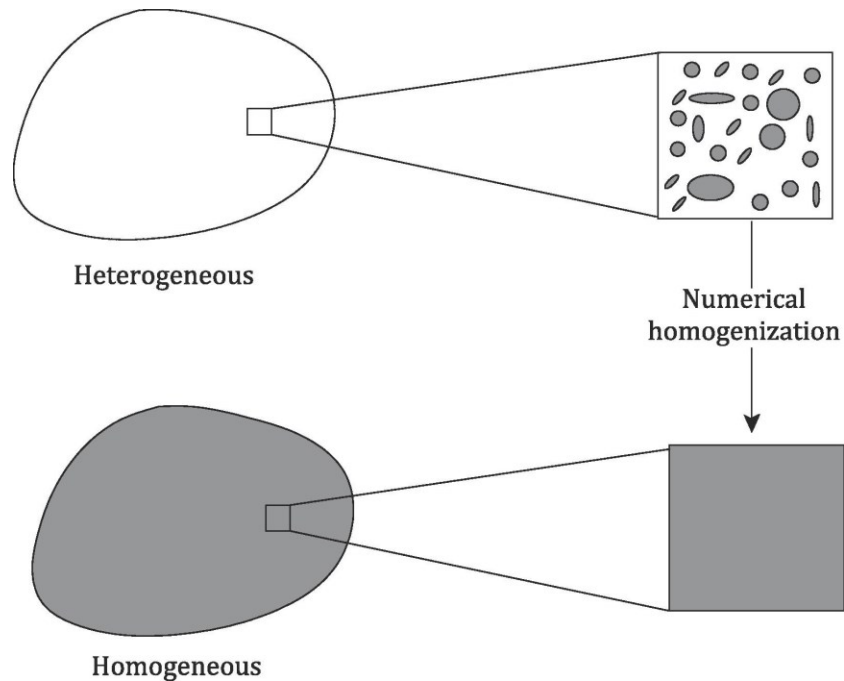


Figure 2-1 Numerical homogenization procedure (Meng et al., 2018).

Numerical homogenization entails computationally modeling the REV with appropriate boundary conditions and loading to calculate localized fields. These fields are then homogenized to derive effective properties of heterogeneous composites. Geers et al., (2010) and Otero et al., (2018) provide comprehensive reviews of the diverse applications of numerical homogenization. Several studies have employed various numerical methods to model the effective properties of artificial frozen soil, as demonstrated in the works of Meng et al., (2020, 2018). However, challenges persist, including the complexity of accounting for microstructures and the reliance on simplifying assumptions regarding constituent interactions. To address the interaction between compounds in a heterogeneous medium, Zhang et al., (2020) introduced a micromechanics-based constitutive model within the continuum micromechanics and homogenization theory framework. This model considers interactions between the matrix (bonded element) and inclusions (frictional element).

Similarly, [Norouzi et al., \(2022\)](#) utilized a two-dimensional numerical homogenization model. They incorporated cohesiveness between compounds and introduced stiffness interface parameters using the eXtended Finite Element Method (XFEM). Incorporating extra degrees of freedom, XFEM enables the modeling of various types of discontinuities, including cohesiveness between matrix and inclusions, and has found successful application in numerical homogenization ([Erkmen and Dias-da-Costa, 2022](#); [Erkmen and Dias-da-Costa, 2021](#); [Nguyen et al., 2020](#)). Both analytical and numerical homogenization approaches have been employed to characterize elastic properties, each with its advantages and limitations. Analytical solutions have been shown to yield ineffective elastic properties in cases with a high-volume fraction of inclusions ([Li and Wong, 2016](#)). For frozen geomaterials, a numerical homogenization approach must appropriately consider the interfacial effect among frozen and unfrozen media. Additionally, obtaining the elastic properties of each compound, crucial inputs for numerical homogenization, is typically not feasible from experimental data. Thus, there's a lack of comprehensive analytical or numerical approaches that can adequately address these challenges.

## **2.4 Thermo-Hydro-Mechanical behavior of frozen soil**

Frozen soils, consisting of soil particles, water, ice, and air, are naturally abundant in various geographical regions, including seasonal frozen and permafrost layers, arctic and subarctic zones, and loess sediments. These regions experience prolonged periods of freezing temperatures ([Kadivar and Manahiloh, 2019](#)). Additionally, there has been a recent increase in the use of the Artificial Ground Freezing (AGF) technique in civil engineering applications such as tunneling, pipelining, mining, and slope constructions. AGF is employed to temporarily enhance soil bearing capacity and regulate ground and groundwater movement ([Vitel et al., 2015](#); [Xu et al., 2019](#)). However, the cyclic freezing and thawing processes pose risks, including infrastructure damage,

subsidence, and borehole failures. Concerns are exacerbated by the effects of climate change, leading to more frequent and severe weather events (Na and Sun, 2017). Frozen soils are divided into two categories: saturated, lacking air, and unsaturated, where air is present within the medium. Freezing processes in both saturated and unsaturated frozen soil can lead to frost heave, causing an expansion of the soil volume. Frost heave occurs when freezing increases water migration and crystallization, resulting in the separation of soil particles. This phenomenon poses a significant risk in cold regions, often causing engineering disasters like pipe ruptures and foundation damage. In saturated soils, where all pores are filled with pore water, the increased volume of water migration and crystallization leads to frost heave. However, in unsaturated cases, part of the volume expansion initially fills the pores, with the remaining increased volume causing frost heave (Bai et al., 2020). Predicting frost heave becomes more complex as it cannot be solely determined by variations in total water and air content. Unlike saturated soil, predicting frost heave in unsaturated soil requires consideration of additional physical variables such as air flux (Li et al., 2021).

## 2.5 Numerical simulation of frozen soil

Efforts to simulate frozen soil can be broadly categorized into thermo-hydro (TH), thermo-mechanical (TM), and thermo-hydro-mechanical (THM) modeling (Arzanfudi and Al-Khoury, 2018). TH modeling involves studying temperature variations and the movement of water, vapor, and ice in the medium by considering mass and energy balance equations. Numerous studies have sought to incorporate the complex behavior of freeze-thaw phenomena through analytical, experimental, and numerical approaches. These aspects encompass phase transition, cryo-suction, and premelting dynamics (Mikkola and Hartikainen, 2001; Zhou and Meschke, 2013).

To determine the total water content in unsaturated frozen soil, [Kurylyk and Watanabe, \(2013\)](#) conducted a comprehensive mathematical study elucidating various forms of the Clapeyron equation and the relationship between the soil moisture curve and soil freezing curve under both saturated and unsaturated freezing conditions. They also developed a model to estimate the hydraulic conductivity of partially frozen soil.

[Bi et al., \(2023\)](#) examined 29 models and categorized them into four groups: theoretical models, soil water characteristic curve (SWCC)-based models, empirical models, and estimation models. Several TH models have been developed and validated using experimental data. [Mizoguchi, \(1990\)](#) conducted experiments to measure the variation of total water content during freezing using a vertical biaxial sample. These experiments have been utilized to validate numerical simulations by [Liu and Yu, \(2011\)](#), [Painter, \(2011\)](#), [Peng et al., \(2016\)](#), and [Stuuroop et al., \(2021\)](#).

[Hansson et al., \(2004\)](#) provided a list of inputs for a thermo-hydro numerical simulation. They developed numerical simulations using a mixed formulation for both water flow and heat transport without considering vapor movement and frost heave. They employed a combination of the [Van Genuchten, \(1980\)](#) soil water characteristic (SWC) curve and a modified Clapeyron equation to estimate liquid and ice saturations during freezing in unsaturated soils. Lower freezing temperatures were determined for unsaturated soil due to pre-freezing pressures (suction). [Dall'Amico et al., \(2011\)](#) proposed that the total water content could be determined independently of temperature using the van Genuchten equation. To enhance the understanding of freezing processes, it's crucial to establish comprehensive constitutive equations describing the relationship between cryogenic suction and capillary pressure. [Painter and Karra, \(2014\)](#) introduced a constitutive relation to calculate ice, water, and air saturations for unsaturated frozen soils, considering temperature, water pressure, and air pressure.

Another benchmark experimental data of soil freezing was reported by [Jame and Norum, \(1980\)](#). Similar to the previous case, they conducted a set of 1D freezing experiments but in a horizontal direction. The numerical inputs for different cases and boundary conditions are available in [Painter, \(2011\)](#) and [Peng et al., \(2016\)](#). Peng's model, based on non-equilibrium ice-water interfaces and utilizing the central Finite Difference Method (FDM) to discretize equations in both spatial and temporal domains, was verified using the aforementioned experimental data ([Peng et al., 2016](#)). [Figure 2-2](#) shows the comparison between experimental data and numerical simulations.

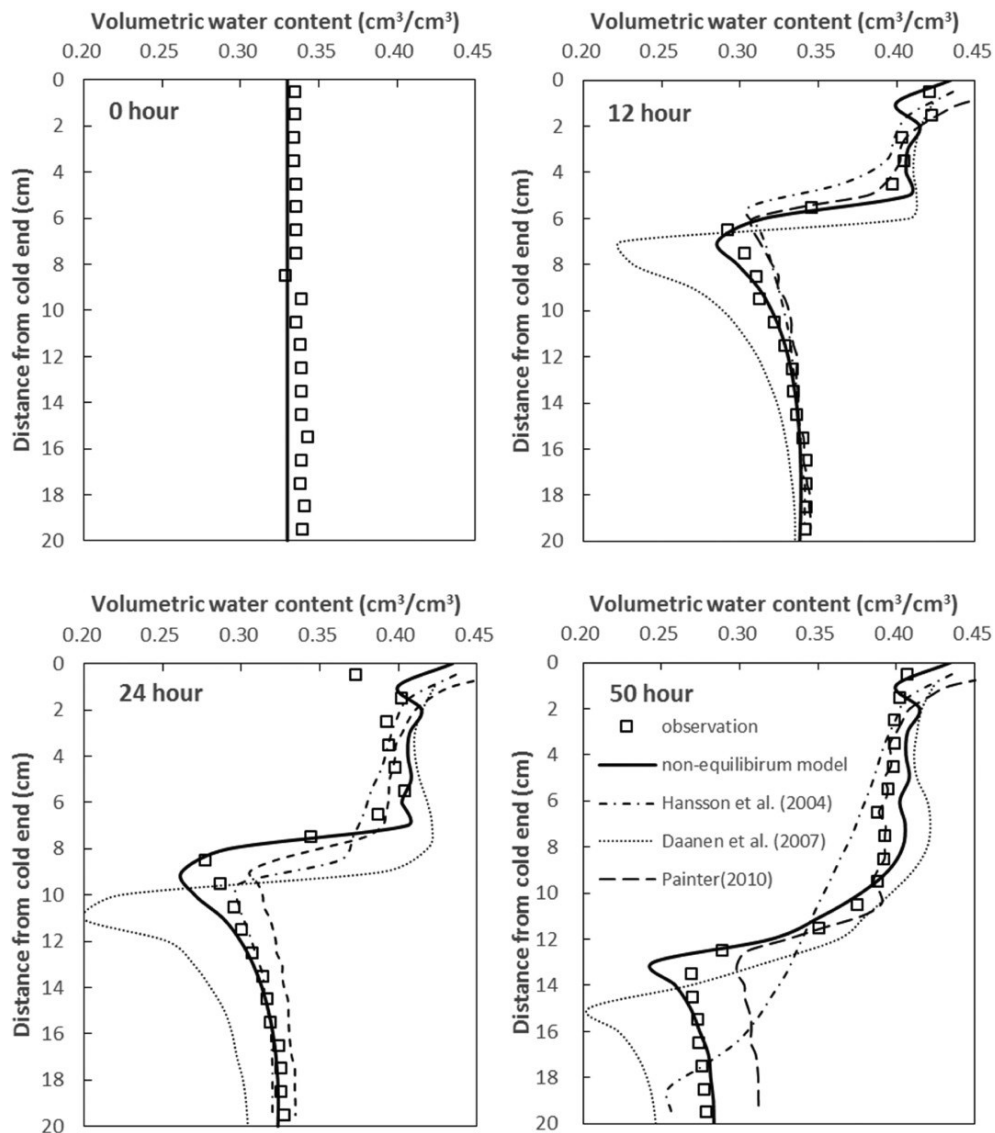


Figure 2-2 Comparison between numerical simulations and experimental data ([Peng et al. 2016](#)).

[Chen et al., \(2022\)](#) introduced an enhanced TH-coupled model based on the Finite Element Method (FEM), which they validated using experimental data from Jame and Norum. These studies primarily investigate variations in temperature and volumetric water content.

Moreover, in modeling unsaturated frozen soil, studying vapor movement during freezing requires additional governing equations ([Gawin et al., 2019](#)). However, the impact of vapor movement on water content has been largely overlooked in the literature, with only a few studies acknowledging that vapor movement cannot be disregarded when the initial water content is low ([He et al., 2020](#)). Previous studies on modeling frost actions in unsaturated soils primarily concentrated on thermo-hydraulic responses, often neglecting geomechanical behavior to simplify the models. However, by incorporating the momentum balance equation into the system of coupling equations, it becomes possible to identify the deformation and stress changes of the medium.

Current THM models for frozen soils are predominantly developed for fully saturated frozen geomaterials ([Arzanfudi and Al-Khoury, 2018](#); [Koniorczyk et al., 2015](#); [Thomas et al., 2009](#)). Among these THM models, [Nishimura et al., \(2009\)](#) derived a formulation and conducted a fully coupled THM analysis of elastoplastic water-saturated frozen soils, considering freezing and thawing processes by incorporating the concept of cryo-suction. [Bekele et al., \(2017\)](#) developed a numerical model to estimate frost heave in saturated porous media using the Isogeometric Analysis (IGA) technique.

Recently, there has been an increased focus on coupled THM models for unsaturated soils ([Liu and Yu, 2011](#); [Teng et al., 2020](#)). [Bai et al., \(2020\)](#) introduced a frost heave model for saturated-unsaturated soils, incorporating an effective strain ratio to relate frost heave strain in unsaturated soils to moisture and temperature fields. The back-calculated effective strain ratio was integrated

into displacement equations, and the model's results were validated against experimental data (Figure 2-3), although it did not account for pore pressure.

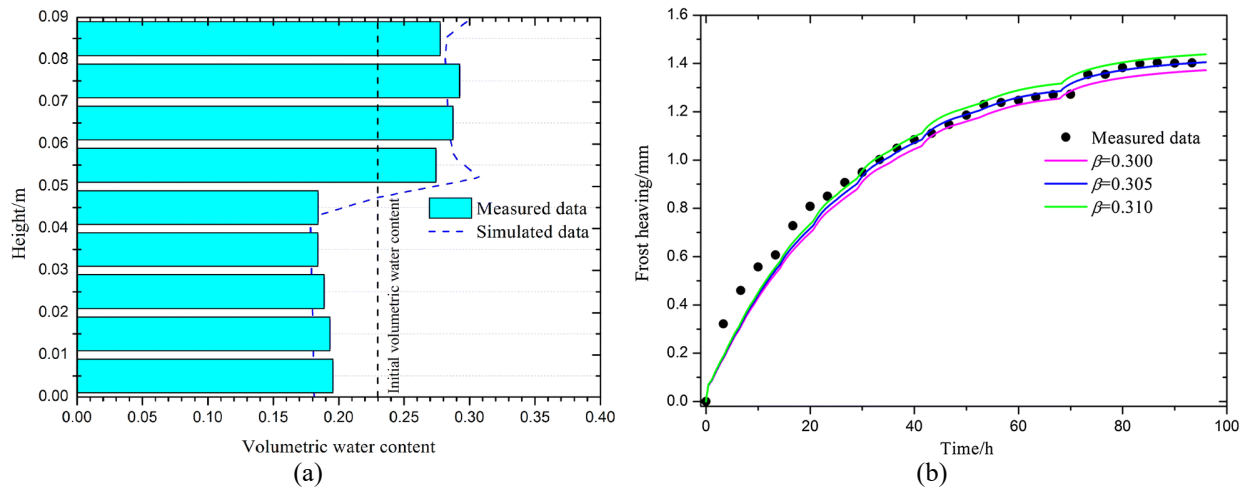


Figure 2-3 Results of simulation of Bai et al., (2020): (a) total volumetric water content at the end of the experiment and (b) frost heave with different values of effective strain ratio

Huang and Rudolph, (2021) presented a THM model to analyze frost heave in variably saturated freezing soils. The gas phase included vapor, with dry air transport neglected for simplicity. The model's validity was confirmed using laboratory test data from literature. They utilized void ratio as a dependent variable to illustrate the correlation between ice lens segregation, stress-deformation, and void ratio evolution.

Li et al. validated their numerical model using experimental data from Mizoguchi and their comprehensive uniaxial experiments (Li et al., 2021). Their numerical results encompassed variations in water content, vapor, and temperature, alongside frost heave. Similarly, Wu and Ishikawa, (2022) devised a thermo-hydro-mechanical model to simulate the freezing process of partially saturated frost-susceptible soils in Hokkaido. Their multiphysics simulations aligned well with frost heave tests on Touryo soil and Fujinomori soil, indicating that the frost heave ratio is directly proportional to the initial degree of saturation and inversely proportional to the cooling rate and overburden pressure.

However, previous models have not adequately characterized pore water, pore ice pressure, and pore air pressure, leading to an unclear definition of the effective stress law. Model formulations have varied significantly due to different researchers' backgrounds (Gawin et al., 2020). There is a lack of a comprehensive and inclusive finite element formulation for describing thermal-hydro-mechanical coupled processes in unsaturated freezing soils, considering pore pressure components from liquid water, air, and ice (Li et al., 2024).

## 2.6 Climate change and permafrost degradation in north of Quebec

Permafrost degradation poses a significant environmental and geological challenge in Arctic and subarctic regions, exemplified in places like Umiujaq in Quebec, Canada. The warming climate induces permafrost thaw, resulting in substantial alterations in slope stability, hydrology, and local ecosystems. Thawing permafrost can instigate slope instability in steep bedrock areas, leading to unexpected and unprecedented slope destabilization (Gruber and Haeblerli, 2007). This is particularly concerning as permafrost serves a crucial role in preserving ground stability. The degradation of permafrost due to rising temperatures is evidenced by the increasing thickness of the active layer and the northward retreat of permafrost extent, with climatic factors playing a significant role (Vasiliev et al., 2020). Further impacts of permafrost degradation include significant implications for hydrology and groundwater dynamics in these regions (Dagenais et al., 2020). Permafrost loss is projected to persist throughout the 21st century, posing a threat to the stability of Arctic infrastructure and the sustainable development of Arctic communities (Hjort et al., 2018; Minsley et al., 2022). The release of carbon from Arctic permafrost due to warming is a significant concern as it can impact the climate (Miner et al., 2022). Additionally, thawing permafrost affects vegetation growth, with changes in surface thaw onset affecting various stages of the growing season in the Arctic permafrost region (Chen and Jeong, 2024; Young et al., 2020).

Moreover, the release of plant-available nitrogen from thawing permafrost in subarctic peatlands leads to changes in vegetation composition and biomass production (Keuper et al., 2017, 2012). Consequently, implementing stabilizing measures in these regions is imperative to mitigate foreseeable geohazards.

## 2.7 Application of Ground Source Heat Pump in permafrost region

In recent years, there has been a rise in the adoption of renewable energy sources for stabilizing permafrost regions. Among these, the Ground Source Heat Pump (GSHP) system has emerged as a notable option, offering a sustainable solution for space heating in subarctic areas. With 44,561 inhabitants of Nord-du-Québec residing in villages within subarctic regions, there exists significant potential to leverage GSHP systems for heating purposes, thereby reducing reliance on fuel typically transported by boat (Gunawan et al., 2020). GSHP technology harnesses the stable temperature of the ground to provide heating, cooling, and hot water for both residential and commercial buildings. In Arctic and subarctic regions, Ground Source Heat Pump (GSHP) systems offer significant applications owing to the relatively stable ground temperatures. Recently, numerous experimental and numerical studies have been conducted to assess various aspects of geothermal energy systems such as Borehole Thermal Energy Storage (BTES), Ground-coupled heat pump (GCHP), and GSHP systems under diverse conditions. These studies have focused on the practical application and benefits of GSHP systems in areas affected by permafrost (Baser and McCartney, 2015; Bidarmaghz et al., 2016; Catolico et al., 2016; Maranghi et al., 2023; Moradi et al., 2015). For a comprehensive overview, Giordano and Raymond, (2019) offer a detailed literature review. GSHP technology proves particularly effective in regions characterized by extreme temperature fluctuations, highlighting its adaptability and potential environmental advantages in Arctic and subarctic climates. Hence, comprehending the intricate behavior of

frozen soil during freezing and thawing is crucial for simulating permafrost and forecasting its behavior with and without the implementation of Ground Source Heat Pump (GSHP) systems. Numerical models play a pivotal role in simulating the effects of freezing and thawing on permafrost, offering valuable insights into future changes and potential impacts on ground stability. These models must integrate climate-warming-induced alterations to precisely simulate permafrost dynamics amid shifting climatic conditions (Perreault et al., 2021; Thomas et al., 2009).

Although using phase change strain, Li et al. validated their numerical model with field data of highly unsaturated loess in northwest China (Li et al., 2024), employing the poro-elastic THM model. Norouzi and Li introduced a coefficient to adjust the phase change strain in an unsaturated frozen medium, developing a poro-plastic numerical model and validating it with experimental data (Norouzi and Li, 2024). However, none of these models were utilized to simulate ground responses under GSHP operations.

## 2.8 Summary

The study of frozen soil behavior, particularly in Arctic and subarctic regions, is paramount given its significant implications for geotechnical engineering, environmental sustainability, and climate change adaptation. Through a synthesis of literature and research findings, it becomes evident that permafrost degradation, accelerated by climate warming, poses multifaceted challenges ranging from slope instability to alterations in hydrology and ecosystem dynamics.

To address these challenges, researchers have increasingly turned to numerical modeling approaches, incorporating advanced methodologies such as numerical homogenization, poro-elastic, and poro-plastic models, to simulate the complex behavior of frozen soil under freezing and thawing conditions. These models, validated through field data and experimental studies,

provide valuable insights into permafrost dynamics and ground stability under changing climatic conditions.

Furthermore, the application of GSHP systems emerges as a promising solution for permafrost stabilization and renewable energy generation in Arctic and subarctic regions. While numerous studies have investigated the practical applications and benefits of GSHP systems in permafrost-affected areas, there remains a gap in understanding the ground responses under GSHP operations.

Moving forward, future research efforts should focus on bridging this gap by integrating numerical models, including numerical homogenization, with GSHP operations to simulate the impacts of freezing and thawing on permafrost. Additionally, there is a need for comprehensive models that incorporate climate-warming-induced changes to accurately predict permafrost dynamics and ground responses under evolving environmental conditions.

## Preface to Chapter 3

The Arctic and subarctic regions are experiencing unprecedented changes due to climate change, leading to significant alterations in the mechanical properties of frozen soils. Understanding these changes is critical for infrastructure development and environmental preservation in cold regions. This chapter explores a novel approach to estimate the elastic properties of heterogeneous frozen clay soils by integrating analytical and numerical models. By employing the eXtended Finite Element Method (XFEM) for numerical homogenization, we delve into the complex interactions between clay-water composites and nonclay mineral inclusions, emphasizing the importance of considering imperfect bonds in predictive models. The insights gained from this study aim to enhance the reliability of engineering applications and contribute to the broader knowledge of soil mechanics in freezing environments.

## Chapter 3

### 3 Estimating equivalent elastic properties of frozen clay soils using an XFEM-based computational homogenization<sup>1</sup>

#### 3.1 Abstract

This study addresses the challenge of estimating the elastic properties of heterogeneous frozen clay soils by introducing a comprehensive approach that combines analytical and numerical models. The frozen clay soil is treated as a mixture composed of frozen clay-water composites and nonclay mineral inclusions. An inversion algorithm is employed to deduce the elastic properties of the matrix (clay-water composites) of two artificially frozen sandy clay samples with known temperature-dependent elastic properties. Subsequently, a two-dimensional numerical simulation using the eXtended Finite Element Method (XFEM) is conducted to carry out numerical homogenization by considering the imperfect bond among frozen clay-water composites and nonclay minerals. The numerical homogenization model offers insights into the temperature-dependent behavior of the interface stiffness parameter. The numerical homogenization results are compared with conventional numerical homogenization approaches like the FEM, which rigidly defines the bonding between inclusions and the matrix. The comparison indicates that the neglect

---

<sup>1</sup> A version of this manuscript has been published in *Journal of Cold Regions Science and Technology* (2024).

of imperfect bonds among clay-water composites and nonclay minerals will lead to unrealistic outcomes in cases with a high fraction of inclusions. This integrated approach advances the understanding and prediction of elastic properties of frozen clay soils by considering their heterogeneous nature.

**Keywords:** frozen clay soils, elasticity, computational homogenization, XFEM, interface stiffness parameter

## 3.2 Introduction

Frozen clay soils, distinguished by their heterogeneous composition of clay-water composites and non-clay minerals display significant sensitivity to temperature and the applied load conditions. (An et al., 2022; Girgis, 2019; Li et al., 2024). A comprehensive understanding of the mechanical behaviors of frozen clay soils is essential in the investigation of geological disasters such as slumps of permafrost (B. Wang et al., 2016), infrastructure damage due to seasonal freeze-thaw actions (Andersland and Ladanyi, 2013), or engineering projects related to the artificial ground freezing (AGF) techniques (Ma et al., 2023). Substantial characterization results on elastic properties of frozen clay soils are essential for studying stress and strain distributions in the frozen ground. Previously, a series of experimental studies have been conducted by researchers to investigate the mechanical responses of frozen clay soils under different temperature and loading rate conditions (Girgis et al., 2020; Li and Akhtar, 2022). Lab data has been summarized to establish empirical temperature-dependent mechanical property relations for frozen soils (Li et al., 2004; Ma et al., 2017; Shi et al., 2023; Zhu et al., 2020). To examine the influence of temperature and strain rate on the mechanical properties of frozen loess, (Xu et al., 2017) carried out a set of uniaxial compressive tests on saturated frozen Helin loess covering five distinct strain rates ( $1 \times 10^{-2}/s$ ,  $1 \times 10^{-3}/s$ ,  $1 \times 10^{-4}/s$ ,  $5 \times 10^{-5}/s$ , and  $1 \times 10^{-5}/s$ ) and four different temperatures ( $-2$  °C,  $-4$  °C,  $-5$  °C, and  $-7$  °C). Considering that the rate-dependent uniaxial compressive behavior of frozen clay soil is markedly influenced by its minerals, void ratio, stress history, and pore fluid salinity, (Girgis et al., 2020) conducted a series of laboratory tests on two artificial frozen clay soils to gauge the rate dependency of uniaxial axial compressive behavior at temperatures ranging from  $-15$  °C to  $0$  °C. The temperature-dependent uniaxial compressive mechanical properties were

measured and modeled using empirical relations, exhibiting a high dependency on the applied deformation rate.

A thorough understanding of the rate dependency behavior and its relationship with temperature requires a large number of specimens with similar compositions and microstructures. Thus, the required sophisticated procedures and the challenges to obtain in-situ frozen clay soils have delayed the theoretical study of their behavior. Laboratory tests can only provide a limited amount of characterization results on some samples, and the intrinsic anisotropic properties of samples with different clay fractions are still with large uncertainties. It is of practical importance to determine how those intrinsic anisotropic properties change with varying amounts of clay fractions. Recently, homogenization methods have been employed to ascertain the equivalent properties of a heterogeneous medium, such as frozen soils, by partitioning the composite material into two or more scales (Chang et al., 2019). Various attempts have been made based on homogenization theory to model the behavior of frozen soils (Zhang et al., 2019; Zhou and Meschke, 2018). Moreover, numerical homogenization elucidates the mechanical behavior of a material under the assumption of periodicity, wherein a Representative Elementary Volume (REV) containing properties at the micro-level is reiterated throughout the heterogeneous material at the macro level. Numerical homogenization involves the computational modeling of a REV with appropriate boundary conditions and loading to compute localized fields, which are then homogenized to obtain effective properties of heterogeneous composites. A comprehensive review of the extensive applications of numerical homogenization is available in the works of Geers et al., (2010) and Otero et al., (2018). Different studies have been conducted to model the effective properties of artificial frozen soil using various numerical methods, such as the works by Meng et

al., (2020, 2018). However, challenges persist, including difficulties in accounting for complex microstructures and reliance on simplifying assumptions about constituent interactions.

To address the interaction between compounds in a heterogeneous medium, a micromechanics-based constitutive model is presented by Zhang et al., (2020) within the framework of continuum micromechanics and homogenization theory, considering the interactions between the matrix (bonded element) and inclusions (frictional element). Additionally, Norouzi et al., (2022) employed a two-dimensional numerical homogenization model and applied cohesiveness between compounds, introducing stiffness interface parameters using the eXtended Finite Element Method (XFEM). By incorporating extra degrees of freedom, XFEM is capable of modeling various types of discontinuities, including cohesiveness between matrix and inclusions, and has been successfully applied to numerical homogenization (Erkmen and Dias-da-Costa, 2022; Erkmen and Dias - da - Costa, 2021; Nguyen et al., 2020). Both analytical and numerical homogenization approaches have been applied to characterize elastic properties but they have advantages and limitations. It has been proven that the effective elastic properties calculated from the analytical solutions are not acceptable for cases with a high volume fraction of inclusions (Li and Wong, 2016). For frozen geomaterials, the interfacial effect among frozen and unfrozen media should be properly considered in a numerical homogenization approach. Apart from that, the elastic properties of each compound as the major inputs for numerical homogenization are not usually available from experimental data. It is a lack of comprehensive analytical or numerical approaches that can accommodate these challenges.

The objective of this paper is to establish a combination of analytical and numerical homogenization methods to estimate the elastic properties of frozen clay soils. The experimental

results of the elastic properties of two different artificial frozen sandy clays are chosen as an application of our numerical approach. After the introduction, the physical properties of frozen sandy clays are provided in [Section 3.3](#). The analytical and numerical homogenization methods applied in this paper are introduced in [Sections 3.4](#) and [3.5](#), respectively. The model verification and mechanical properties of artificial frozen sandy clay soils are given in [Section 3.6](#). Discussion about the higher volumetric content of the non-clay minerals, comparison of the simulated results with the analytical solution, and the effect of randomly generated minerals are provided in [Section 3.7](#). Finally, [Section 3.8](#) is allocated for the conclusions of this study.

### 3.3 Basic physical properties

In this section, the physical properties of frozen soils including volumetric-mass and densities relations that are used in the following sections are described. A saturated frozen clay soil medium is composed of clay mineral ( $c$ ), water ( $w$ ) and non-clay minerals ( $nc$ ). Therefore, the total volume of the frozen soil ( $V$ ) medium can be explained as:

$$V = V_c + V_w + V_{nc} \quad (3.1)$$

where,  $V_c$ ,  $V_w$ , and  $V_{nc}$  are the volume of clay minerals, water and non-clay minerals. Denoting  $cw$  as the clay-water composite, the volume fraction of the clay-water composite is defined as follows:

$$f_{cw} = \frac{V_{cw}}{V} = 1 - f_{nc} \quad (3.2)$$

Here  $V_{cw}$  is the total volume of clay-water composite and  $f_{nc}$  is the volume fraction of non-clay minerals. Accordingly, the clay fraction by mass of the sample is expressed as:

$$C_f = \frac{m_c}{m_c + m_{nc}} = \frac{\rho_c V_c}{\rho_c V_c + \rho_{nc} V_{nc}} \quad (3.3)$$

where  $m_c$  and  $m_{nc}$  are the mass of clay and non-clay minerals, respectively and  $\rho_c$  and  $\rho_{nc}$  are the densities of clay and non-clay minerals, respectively. If we assume that the densities of clay and non-clay minerals are equal (i.e.,  $\rho_c = \rho_{nc}$ ), a relation between the volume fraction of clay water composite and clay fraction by mass is concisely given as:

$$f_{cw} = C_f(1 - \phi) + \phi \quad (3.4)$$

in which,  $\phi$  is the porosity of the medium and is defined as the ratio of the volume of void to the total volume:

$$\phi = \frac{V_w}{V} = \frac{e}{1 + e} \quad (3.5)$$

where  $e$  is the void ratio of the medium. To calculate the void ratio, the following equation can be used:

$$e = \frac{G_s \rho_w}{\rho_d} - 1 \quad (3.6)$$

In [Equation \(3.6\)](#),  $G_s$  is the specific gravity of the medium,  $\rho_w$  is the water density, and  $\rho_d$  is the dry density. The dry density is expressed as a function of bulk density ( $\rho_b$ ) and water content ( $w$ ) as follows:

$$\rho_d = \frac{\rho_b}{1 + w} \quad (3.7)$$

### 3.4 Analytical homogenization methods

This section presents two typical analytical approaches for estimating the effective elastic properties of heterogeneous materials. The Reuss model employs simplified formulations to compute the lower bound of elastic properties, while the differential effective medium (DEM) theory determines the homogenized elastic parameters of a medium by solving a pair of fully coupled ordinary differential equations ([Markov et al., 2009](#)).

The Reuss model enables the estimation of the lower bound for the elastic properties of geomaterials. The Reuss model assumes that all components of the heterogeneous material experience identical stress conditions and estimates the equivalent bulk ( $K_e$ ) and shear ( $G_e$ ) moduli of a fine-grained geomaterial as follows:

$$\begin{aligned}\frac{1}{K_e} &= \frac{f_{cw}}{K_{cw}} + \frac{(1 - f_{cw})}{K_{nc}} \\ \frac{1}{G_e} &= \frac{f_{cw}}{G_{cw}} + \frac{(1 - f_{cw})}{G_{nc}}\end{aligned}\tag{3.8}$$

where,  $K_{cw}$  and  $K_{nc}$  denote the bulk modulus of clay-water composites and nonclay minerals, respectively, while  $G_{cw}$  and  $G_{nc}$  represent the shear modulus of clay-water composites and nonclay minerals, respectively.

The differential effective medium (DEM) theory approaches the modeling of two-phase composites by progressively introducing inclusions from one phase into the matrix phase until the desired composition of the constituents is achieved (Cleary et al., 1980; Norris et al., 1985; Zimmerman, 1984). In the case of frozen clay soil samples, by considering  $A^K$  and  $A^G$  as the geometric factors, the coupled system of ordinary differential equations governing the effective bulk modulus and shear modulus is expressed as follows:

The rate of change of bulk modulus concerning the volume fraction of nonclay minerals ( $f_{nc}$ ) is given by:

$$\frac{dK_e}{df_{nc}} = \frac{1}{(1 - f_{nc})} (K_{nc} - K_e) A^K\tag{3.9}$$

The rate of change of shear modulus concerning the volume fraction of nonclay minerals ( $f_{nc}$ ) is given by:

$$\frac{dG_e}{df_{nc}} = \frac{1}{(1 - f_{nc})} (G_{nc} - G_e) A^G \quad (3.10)$$

Also, [Markov et al., \(2009\)](#) introduced geometric factors for nonclay minerals with a spherical shape as:

$$\begin{aligned} A^K &= \frac{3K_{cw} + 4G_{cw}}{3K_{nc} + 4G_{cw}} \\ A^G &= \frac{5G_{cw}(3K_{cw} + 4G_{cw})}{G_{cw}(9K_{cw} + 8G_{cw}) + 6G_{nc}(K_{cw} + 2G_{cw})} \end{aligned} \quad (3.11)$$

### 3.5 Numerical homogenization

#### 3.5.1 Equilibrium of a deformable body

Considering  $\Omega$  as the domain of analysis and  $\Gamma_D$ , and  $\Gamma_N$  as the Dirichlet and Neumann boundaries, respectively, by principles of continuum mechanics, the governing equation for the equilibrium of a deformable two-dimensional body and its corresponding boundary conditions can be formulated as follows:

$$\begin{aligned} \nabla_{\mathbf{x}} \cdot \boldsymbol{\sigma} + \mathbf{p} &= \mathbf{0} && \text{in } \Omega \\ \mathbf{u} &= \mathbf{r} && \text{in } \Gamma_D \\ \mathbf{n} \cdot \boldsymbol{\sigma} &= -\mathbf{s} && \text{in } \Gamma_N \end{aligned} \quad (3.12)$$

In these equations,  $\nabla_{\mathbf{x}}^T = \langle \partial/\partial x_1 \quad \partial/\partial x_2 \rangle$  represents the gradient operator, and ‘.’ signifies the dot product operator. Additionally,  $\boldsymbol{\sigma}$  and  $\mathbf{p}$  denote the stress tensor and body force, while  $\mathbf{r}$  and  $\mathbf{s}$  represent the prescribed displacement and traction, respectively. To establish the relationship between stress and the gradient of displacement, a constitutive relation is essential:

$$\boldsymbol{\sigma} = \mathbf{D} : \nabla_{\mathbf{x}} \otimes \mathbf{u} \quad \text{in } \Omega \quad (3.13)$$

Here, ‘.’ denotes the double dot product, ‘ $\otimes$ ’ represents the tensorial product, and  $\mathbf{D}$  is the stiffness matrix. Due to variations in the mechanical properties of heterogeneous materials throughout the

medium, the numerical homogenization method allows for the estimation of the effective stiffness matrix ( $\hat{\mathbf{D}}$ ) based on the equivalent elastic modulus and Poisson's ratio of the substance. This matrix can then be substituted into [Equation 3.13](#) to assess the homogenized displacement.

### 3.5.2 The first order of homogenization

In numerical homogenization, it is assumed that the properties of non-homogenous material vary periodically at the mesoscale. As drawn in [Figure 3-1](#), the domain can be segmented into uniform cells that are considerably smaller than the entirety of the soil structure. Based on the asymptotic expansion theory,  $\mathbf{x}$  refers to the position in the macro-scale and  $\mathbf{y} = \mathbf{x}/\eta$  is a fast-periodic coordinate within a cell i.e.,  $0 \leq \mathbf{y} \leq \mathbf{Y}$  that  $\mathbf{Y}$  is the geometric period of the cell ([Figure 3-1](#)). As a result, the transformed derivation operation will be presented as:

$$\frac{\partial}{\partial \mathbf{x}} \rightarrow \frac{\partial}{\partial \mathbf{x}} + \frac{1}{\eta} \frac{\partial}{\partial \mathbf{y}} \quad (3.14)$$

where  $\eta$  is the scaling parameter representing the ratio between the size of the meso-scale and macro-scale. Accordingly, the exact displacement field and the expanded form of the stress gradient are determined based on the asymptotic expansion theory as follows ([Hassani and Hinton, 1998](#)):

$$\mathbf{u}(\mathbf{x}, \mathbf{y}) = \bar{\mathbf{u}}(\mathbf{x}, \mathbf{y}) + \eta \bar{\bar{\mathbf{u}}}(\mathbf{x}, \mathbf{y}) + \dots \quad (3.15)$$

$$\boldsymbol{\sigma}(\mathbf{x}, \mathbf{y}) = \tilde{\boldsymbol{\sigma}}(\mathbf{x}, \mathbf{y}) + \eta \tilde{\tilde{\boldsymbol{\sigma}}}(\mathbf{x}, \mathbf{y}) + \dots \quad (3.16)$$

wherein,  $\bar{\mathbf{u}}(\mathbf{x}, \mathbf{y})$  and  $\tilde{\boldsymbol{\sigma}}(\mathbf{x}, \mathbf{y})$  are the first approximation solutions. The oscillatory behavior parameters of displacement and stress fields are represented by  $\bar{\bar{\mathbf{u}}}(\mathbf{x}, \mathbf{y})$  and  $\tilde{\tilde{\boldsymbol{\sigma}}}(\mathbf{x}, \mathbf{y})$ , each varying with distinct orders of  $\eta$ .

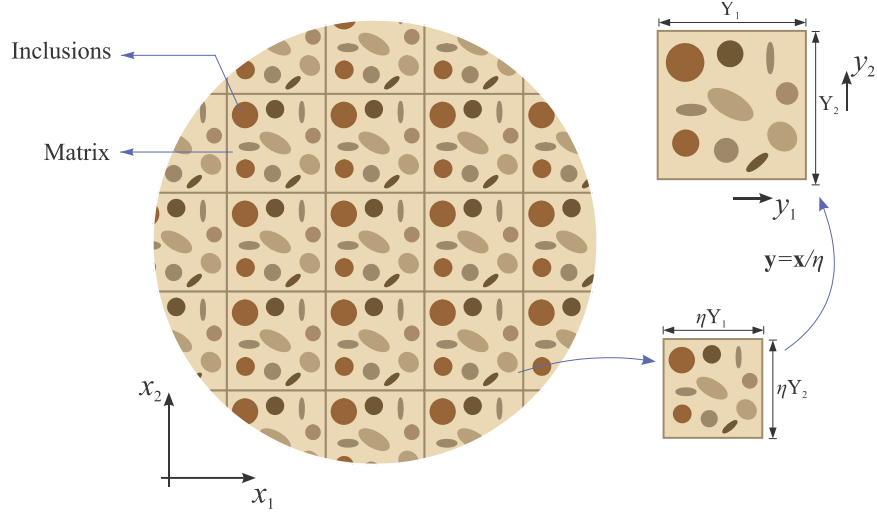


Figure 3-1 Representation of slow and fast coordinates in a heterogeneous framework: (a) a sample, (b) a REV at the micro-scale model, and (c) a REV converted to the fast coordinate, after [Norouzi et al. \(2022\)](#).

By inserting [Equation 3.14](#) into [Equation 3.12](#), the resulting equation is:

$$\nabla_{\mathbf{x}} \cdot \boldsymbol{\sigma}(\mathbf{x}, \mathbf{y}) + \frac{1}{\eta} \nabla_{\mathbf{y}} \cdot \boldsymbol{\sigma}(\mathbf{x}, \mathbf{y}) = -\mathbf{p}(\mathbf{x}) \quad (3.17)$$

Incorporating [Equations 3.15](#) and [3.16](#) into [Equation 3.13](#) and arranging them by their respective orders (i.e., 1 and  $\eta$ ), results in:

$$0 = \mathbf{D}(\mathbf{x}, \mathbf{y}) : \nabla_{\mathbf{y}} \otimes \bar{\mathbf{u}}(\mathbf{x}) \quad (3.18)$$

$$\tilde{\boldsymbol{\sigma}}(\mathbf{x}, \mathbf{y}) = \mathbf{D}(\mathbf{x}, \mathbf{y}) : (\nabla_{\mathbf{x}} \otimes \bar{\mathbf{u}}(\mathbf{x}) + \nabla_{\mathbf{y}} \otimes \bar{\bar{\mathbf{u}}}(\mathbf{x}, \mathbf{y})) \quad (3.19)$$

[Equation 3.18](#) highlights the independence of  $\bar{\mathbf{u}}$  from the rapid coordinate. Given that only the first order of homogenization is the focus of this research, other stress parameter terms are disregarded. Consequently, integrating [Equation 3.19](#) into [Equation 3.20](#) yields two distinct equations with different orders:

$$\nabla_{\mathbf{x}} \cdot \tilde{\boldsymbol{\sigma}}(\mathbf{x}, \mathbf{y}) + \mathbf{p}(\mathbf{x}) = 0 \quad \text{in } \Omega \quad O(1) \quad (3.20)$$

$$\nabla_{\mathbf{y}} \cdot \tilde{\boldsymbol{\sigma}}(\mathbf{x}, \mathbf{y}) = 0 \quad \text{in } \gamma \quad O(1/\eta) \quad (3.21)$$

### 3.5.3 The variational setting for homogenization

In order to solve the governing equations (i.e., [Equations 3.20](#) and [3.21](#)), the weak form of partial differential equations (PDEs) should be derived. Transforming these equations from their strong forms to their weak forms will facilitate a more robust numerical treatment. It enables us to impose different boundary conditions and offers flexibility in our choice of approximation functions. Assuming that  $\mathbf{p}$  and  $\mathbf{s}$  are not a function of the fast coordinate, to establish the weak form of the balance equation, [Equation 3.20](#) is multiplied by the variation of the first approximate displacement ( $\delta\bar{\mathbf{u}}$ ) and integrated by parts throughout a single domain of the cell. This gives:

$$\int_{\Omega} \nabla_{\mathbf{x}} \otimes \delta\bar{\mathbf{u}} : \hat{\boldsymbol{\sigma}} d\Omega + \int_{\Omega} \delta\bar{\mathbf{u}} \cdot \mathbf{p} d\Omega + \int_{\Gamma_N} \delta\bar{\mathbf{u}} \cdot \mathbf{s} d\Gamma = 0 \quad (3.22)$$

where,  $\hat{\boldsymbol{\sigma}}$  stands as the effective stress tensor. With  $|Y|$  as the area of the cell, the effective stress tensor is given as:

$$\hat{\boldsymbol{\sigma}} = |Y|^{-1} \int_Y \tilde{\boldsymbol{\sigma}}(\mathbf{x}, \mathbf{y}) dY \quad (3.23)$$

The weak form of [Equation 3.21](#) can be derived similarly by multiplying with the virtual displacement fluctuations ( $\delta\bar{\bar{\mathbf{u}}}$ ), and integrating over a domain of one cell ( $Y$ ) ([Geers et al., 2010](#)):

$$\int_Y \nabla_{\mathbf{y}} \otimes \delta\bar{\bar{\mathbf{u}}} : \boldsymbol{\sigma} dY - \int_{\Psi} \delta\bar{\bar{\mathbf{u}}} \cdot \boldsymbol{\sigma} \cdot \mathbf{n} d\Psi = 0 \quad (3.24)$$

Here,  $\Psi = \partial Y$  denotes as the boundary of the cell representing the fast coordinate on the cell boundary. In the context of numerical engineering analysis, the Hill-Mandel condition is described by [Equation 3.24](#) that offers a framework for evaluating non-homogeneous materials at both micro and macro scales. It enables the decoupling of analyses for heterogeneous materials into local and

global scales. Assuming that the scaling parameter approaches zero (i.e.,  $\eta \rightarrow 0$ ), and given the relationship between the gradients of average displacement and stress within a single cell, as derived from the solution of Equation 3.24, the weak form of the equilibrium equation over the heterogeneous domain can be replaced by Equation 3.22. This substitution allows the heterogeneous model to transition to a homogenized model, characterized by effective properties derived from the REV.

### 3.5.4 REV boundary value problem

To represent the properties of the finest segment of the heterogeneous medium's micro-structural volume, it's essential to define a REV alongside the appropriate boundary conditions for solving Equation 3.24. Given that the precise boundary condition of the heterogeneous medium isn't predetermined, various general boundary conditions like uniform gradient, uniform traction, or periodicity can be chosen to analyze the REV. In this research, considering our assumption of the heterogeneous medium's periodicity (as illustrated in Figure3-1b), we've opted for the periodic boundary condition. This condition is applied to the REV, facilitating the computation of the average displacement field and the local level stress tensor. From this, the components of the effective stiffness matrix are discerned based on three specific displacement gradient cases:

$$\begin{bmatrix} \hat{\sigma}_{11}^1 & \hat{\sigma}_{11}^2 & \hat{\sigma}_{11}^3 \\ \hat{\sigma}_{22}^1 & \hat{\sigma}_{22}^2 & \hat{\sigma}_{22}^3 \\ \hat{\sigma}_{12}^1 & \hat{\sigma}_{12}^2 & \hat{\sigma}_{12}^3 \end{bmatrix} = \begin{bmatrix} \hat{D}_{1111} & \hat{D}_{1122} & \hat{D}_{1112} \\ \hat{D}_{1122} & \hat{D}_{2222} & \hat{D}_{2212} \\ \hat{D}_{1112} & \hat{D}_{2212} & \hat{D}_{1212} \end{bmatrix} \begin{matrix} \text{Case1} & \text{Case2} & \text{Case3} \\ \begin{bmatrix} 1 & 0 & 0 \\ 0 & 1 & 0 \\ 0 & 0 & 1 \end{bmatrix} \end{matrix} \quad (3.25)$$

Subsequent to establishing the weak form of the computational homogenization equations, they are discretized utilizing the eXtended Finite Element Method (XFEM). By utilizing the XFEM, the displacement field and the traction vector at the discontinuity interfaces can be defined. To adjust cohesion between inclusions and the matrix at the discontinuity interfaces, the cohesive

stiffness matrix (expressed as  $\mathbf{c} = c\mathbf{I}$ ) is incorporated within the traction vector formulation, where  $c$  is scalar stiffness coefficient, and  $\mathbf{I}$  is the unit matrix. Detailed steps, such as the method for enforcing boundary conditions and the final matrix assembly, are further discussed in (Nguyen et al., 2020; Emad Norouzi et al., 2022). To deduce the elastic characteristics of the heterogeneous material, a specialized code developed in-house was leveraged.

After introducing both analytical and numerical homogenization methods, the flowchart of the current research is described herein. Figure 3-2 shows the step-by-step computational methodology employed to extract the elastic properties of a clay-water composite within a heterogeneous material, considering the concurrent presence of non-clay minerals. In a study area, samples with the highest clay fraction (preferred to have an  $f_{cw}$  higher than 0.7) will be selected to carry out laboratory tests. Since the elastic properties of nonclay minerals (rigid particles or aggregates) of a geomaterial can be easily retrieved from the literature or handbook (Markov et al., 2009), the elastic properties of the clay-water composite can be back-calculated using the DEM approach through an inversion calculation when the elastic properties of the bulk soil sample are available from laboratory tests. With the calculated elastic properties of clay-water composites and non-clay minerals as inputs, we will be able to estimate equivalent elastic properties of a frozen clay sample with any  $f_{cw}$  using our XFEM tool.

Within the XFEM framework, the interface stiffness parameter, is calibrated by using the newly determined elastic properties of the clay-water composite and the known properties of the non-clay mineral. The calibrated model is subsequently run to validate convergence. Post-validation, adjustments to the volume content are made, if necessary, to represent scenarios with higher non-clay mineral volume content. The final output yields the effective homogenized elastic properties

of the heterogeneous material, paving the way for more accurate geotechnical modeling and simulations.

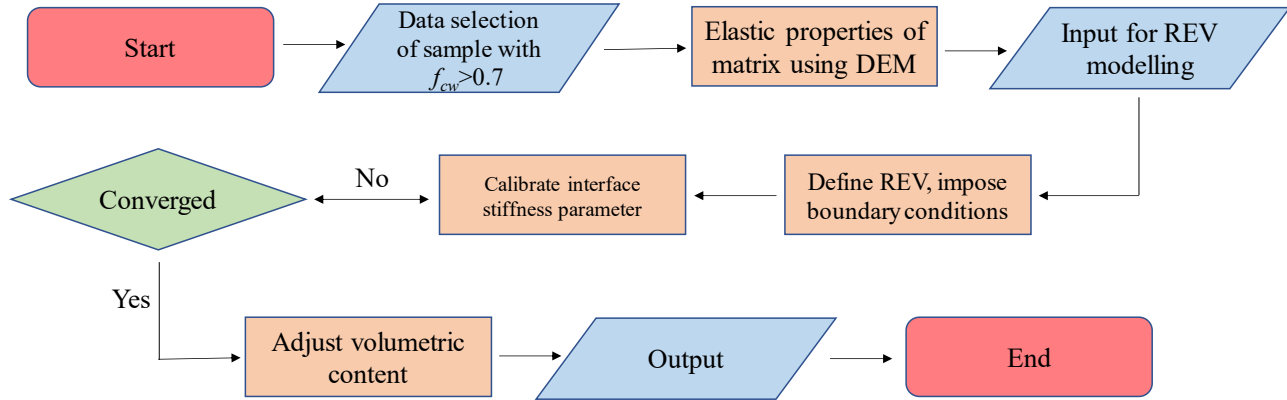


Figure 3-2 The flowchart of the proposed comprehensive numerical approach for estimating elastic properties of frozen clay soils.

## 3.6 Verification and numerical simulations

### 3.6.1 Model verification

To evaluate the robustness of the analytical and numerical models, the experimental data of a soil-rock mixture has been selected. For a soil-rock mixture, the soil is treated as the matrix and rock is included as the inclusion. Thus, the volume fraction of soil in a soil-rock mixture will be equivalent to the  $f_{cw}$  in a frozen clay soil. The experimental data presented in this study was originally obtained by [Yang et al., \(2015\)](#). These experiments were conducted at both normal (+20°C) and frozen (-20°C) temperatures, encompassing a range of volume fraction of rock content, varying from 0.30 to 0.70. [Yang et al., \(2015\)](#) also developed an analytical model for the normal temperature case using a two-layer embedded model of a single inclusion and a three-layer model of a double inclusion composite for the frozen temperature case. Their models were rigorously validated against the experimental results. Additionally, [Meng et al., \(2020\)](#) and [\(2018\)](#) employed the experimental data of 30% and 40% of rock content to verify the accuracy of their numerical homogenization model. The current numerical method has been validated by employing

the experimental data of elastic modulus of soil-rock mixture with different rock content in the REV under both normal and frozen conditions (Emad Norouzi et al., 2022). The results based on the XFEM model were achieved by calibrating interface stiffness parameters using samples containing 30% rock content by volume at both normal and frozen temperatures. Subsequently, these calibrated parameters were applied to verify other samples.

The material properties of the soil and rock, acquired from existing literature, as well as the interface stiffness parameters calibrated for normal and frozen temperatures as reported in references, are presented in Table 3-1.

Table 3-1 Elastic properties of soil, rock and interface stiffness parameter applied to current numerical model

Material properties	Temperature	
	T = 20 °C	T = -20 °C
Elastic modulus of the matrix (MPa)	2.62	10.15
Poisson's ratio of the matrix (-)	0.4	0.38
Elastic modulus of the rock (MPa)	40000	40000
Poisson's ratio of the rock (-)	0.2	0.2
Interface stiffness parameter (MPa)	336	1600

To compare the results of analytical models as well as numerical XFEM simulation results, Figure 3-3 presents the graph of homogenized elastic modulus of soil-rock mixtures at normal and freezing conditions.

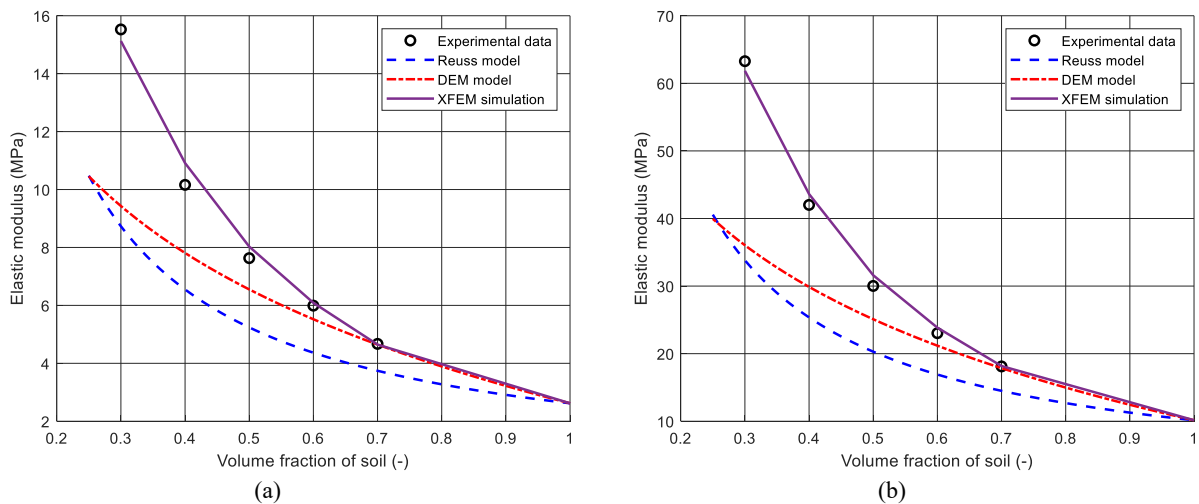


Figure 3-3 Elastic modulus of soil-rock mixtures: comparison between analytical and numerical methods for (a) normal and (b) freezing temperatures.

As shown in [Figure 3-3](#), the results show that the DEM is notably effective for scenarios with a predominant soil component. Conversely, when dealing with samples that have a diminished soil proportion, analytical approaches fail to accurately represent outcomes, largely due to the neglecting of interactions between the matrix and inclusions. By introducing an interface stiffness parameter, it becomes possible to quantify the cohesive relationship between soil and rock. Additionally, [Figure 3-3](#) highlights that while this parameter is temperature-dependent, its value remains consistent irrespective of the rock fraction at a specific temperature, emphasizing its relevance in geotechnical analyses. The case of this soil-rock mixture is used to demonstrate that the DEM approach is very reliable when the soil volume fraction (volume fraction of matrix) is more than 0.7. Thereby, we have chosen 0.7 as a threshold  $f_{cw}$  value for a frozen clay soil sample selected to estimate clay water composite elastic properties using DEM ([Figure 3-2](#)).

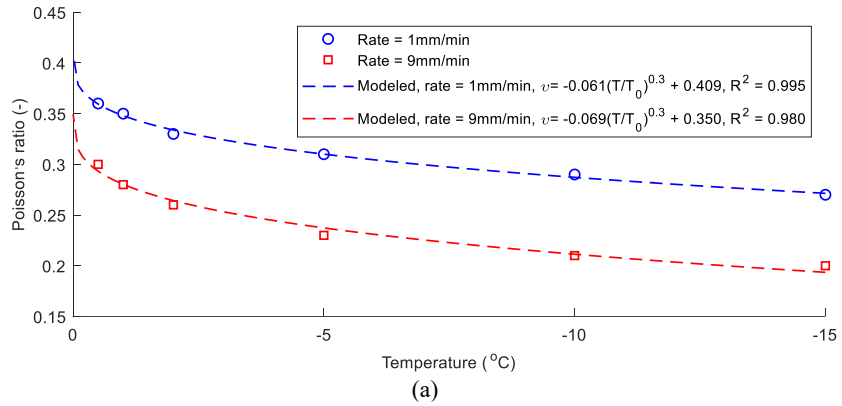
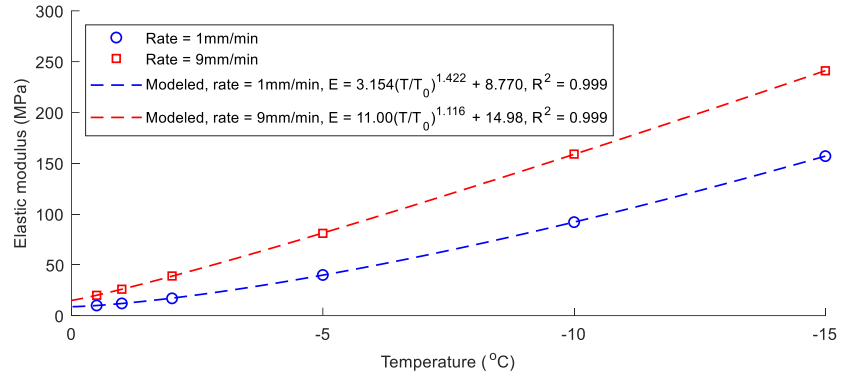
### 3.6.2 Mechanical properties of artificial frozen sandy clay soils

In this section, the algorithm previously introduced is used to estimate the elastic properties of two artificially frozen sandy clay samples. The experimental data and related experimental procedures can be found in ([Girgis et al., 2020](#)). In their studies, Kaolinite-sand and Bentonite-sand samples were prepared and tested at diverse temperatures: 0 °C, -0.5 °C, -1 °C, -2 °C, -5 °C, -10 °C, and -15 °C. The elastic modulus and Poisson's ratio for every sample were determined at loading rates of 1mm/min, 3mm/min, and 9mm/min. The physical properties of the samples including dimensions, bulk density, and water content are provided in [Table 3-2](#).

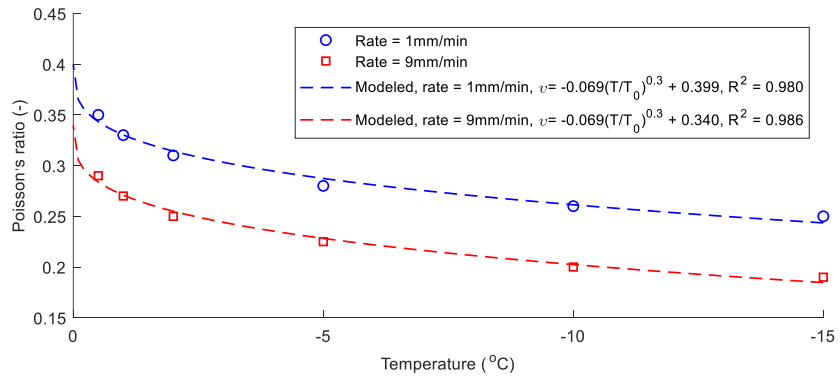
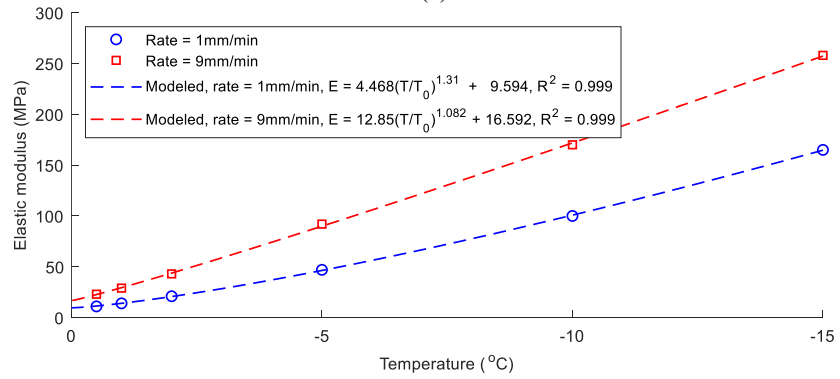
Table 3-2 Kaolinite-sand and Bentonite-sand: Experimental setup and properties.

Sample	Dimension		Bulk density (g/cm <sup>3</sup> )	Water content
	Height (mm)	Diameter (mm)		
Kaolinite-sand	101.6	50.8	1.76	23%
Bentonite-sand	101.6	50.8	1.53	59%

Girgis et al. (2020) determined the Young's modulus using the tangent method at the half-peak strength point, and similarly, the Poisson ratio was computed under the same stress conditions. Some results of Young's modulus and Poisson's ratio of artificially frozen Kaolinite-sand and Bentonite-sand versus temperature are displayed in Figure 3-4 for each loading rate. They also found that values of the deformation parameters are sensitive to temperature and loading rate. Fitted temperature-dependent power law functions were proposed to estimate elastic modulus and Poisson's ratio for each loading rate. A strong correlation between both Young's modulus and Poisson's ratio was captured. Young's modulus displayed a significant linear-like increasing trend with the decrease in temperature, while Poisson's ratio displays a nonlinear decreasing trend with a decrease in temperature. Figure 3-4a and Figure 3-4b indicate that the bentonite-sand samples have higher values of Young's modulus compared to kaolinite-sand samples, whereas the values of Poisson's ratio values for Bentonite-sand samples are lower than Kaolinite-sand samples.



(a)



(b)

Figure 3-4 Elastic modulus and Poisson's ratio of (a) Kaolinite-sand, and (b) Bentonite-sand, data is from Girgis et al. (2020).

### 3.6.2.1 Back calculation of elastic properties of matrix

As mentioned, the elastic properties of the clay-water composite should be calculated and then applied to the numerical homogenization model. In order to find the elastic properties of the clay-water composite at different temperatures and different rates, the inversion method, drawn in Figure 3-5 should be employed. The inversion approach commences with the obtained elastic properties of the matrix (represented in clay-water composites) from artificially frozen Kaolinite-sand and Bentonite-sand.

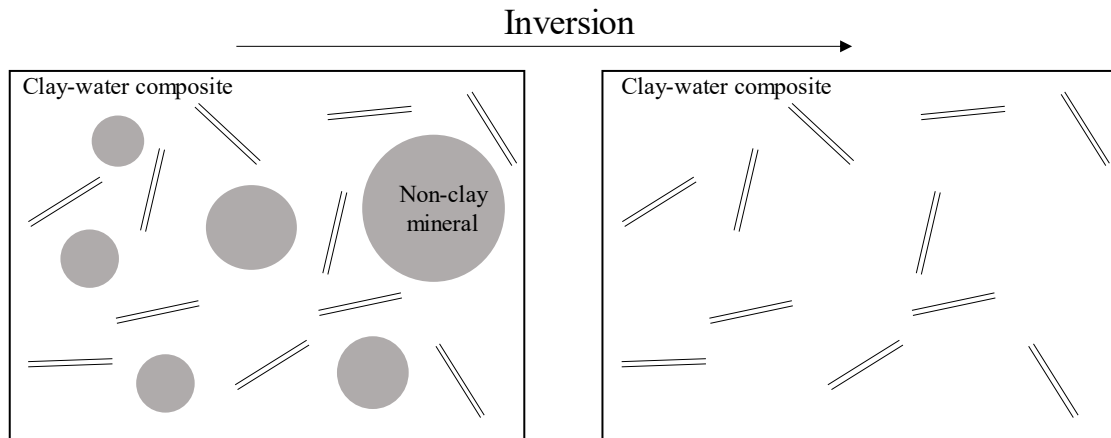


Figure 3-5 The inversion algorithm to find elastic properties of clay-water composites using DEM, modified after (Li and Wong, 2017).

As verified in the previous section, DEM can be employed if the volume fraction of the clay water composite ( $f_{cw}$ ) is larger than 0.7. As the elastic properties of the samples and non-clay minerals are available, DEM can estimate the elastic properties of the matrix can be back-calculated. The volume fraction of non-clay minerals and the elastic properties of non-clay minerals are written in Table 3-3. In this paper, it is assumed that the elastic properties of the non-clay minerals are constant as temperature differs.

Table 3-3 Volumetric and elastic properties of non-clay minerals, applied to DEM

Sample	Volume fraction of non-clay minerals, $f_{nc}$	Elastic modulus of non-clay minerals (MPa)	Poisson's ratio of non-clay minerals (-)
Kaolinite-sand	0.27	40000	0.2
Bentonite-sand	0.18	40000	0.2

The experimental data of 1mm/min and 9mm/min are selected and their corresponding elastic properties of both Kaolinite-sand and Bentonite-sand are calculated and presented in Figure 3-6 at different temperatures.

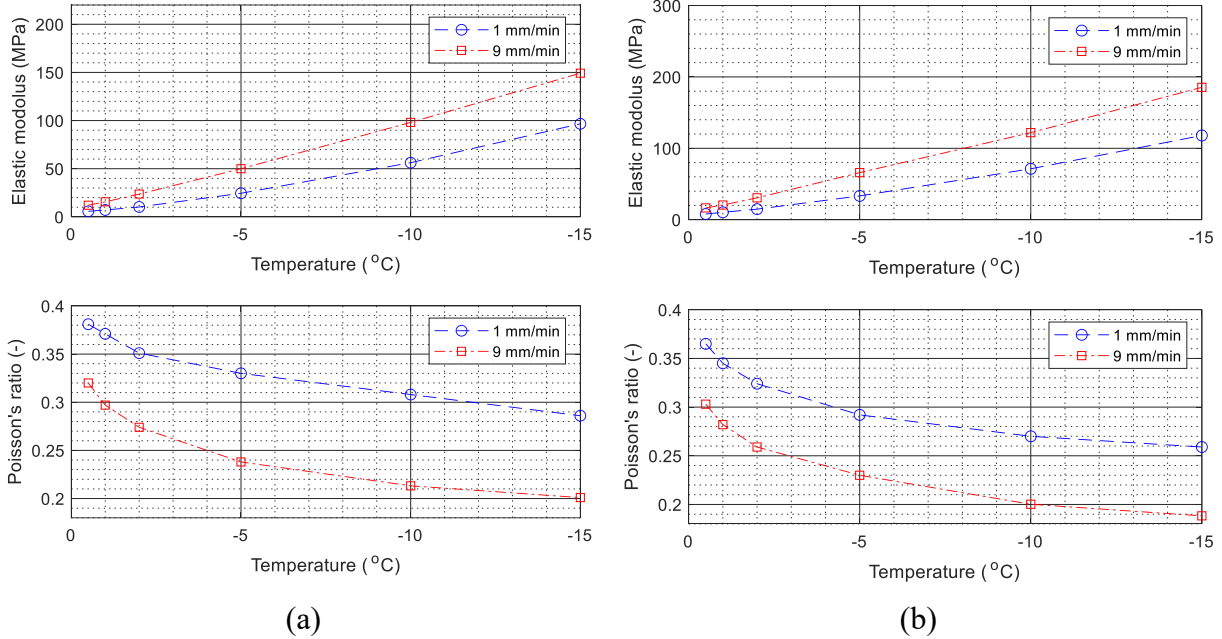


Figure 3-6 Inversion algorithm: Using DEM method to find the elastic properties of (a) Kaolinite-sand and (b) Bentonite-sand versus temperature

### 3.6.2.2 Interface stiffness parameters at different temperatures

Following the estimation of the clay-water composite properties, the proposed numerical homogenization can be utilized by creating the REV. Inclusions should be defined based on the volumetric content of the non-clay minerals, as outlined in Table 3-3. For the sake of generality, the inclusions are placed in an aligned and symmetric fashion, with their positioning being determined by the size of the non-clay minerals as shown in Figure 3-7. In the discussion section, the impact of the size and configuration of inclusions is explored.

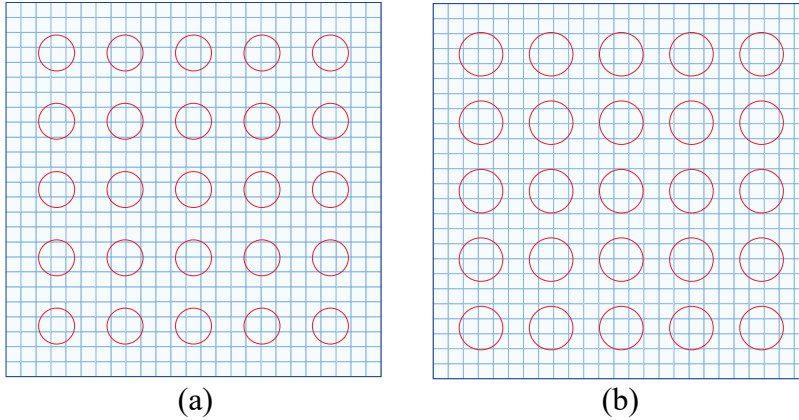
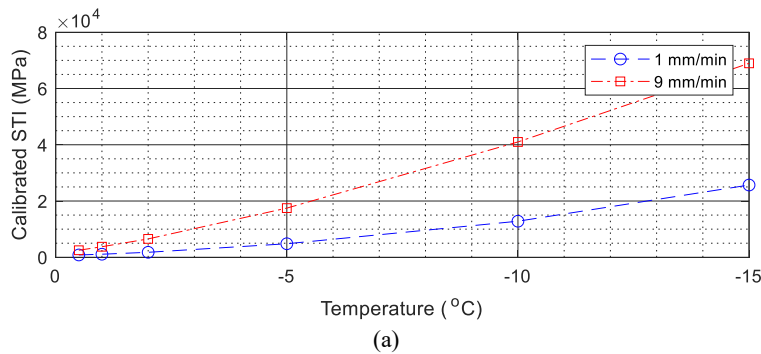


Figure 3-7 Numerical meshing of REV elements employed in current numerical homogenization method: (a) Kaolinite-sand and (b) Bentonite-sand

Both REV elements are simulated with calculated elastic properties of clay-water composites from the previous section, the elastic properties of non-clay minerals written in Table 3-3. Also, to match the modeled results with the experimental data, the interface stiffness parameter should be calibrated. After simulation of all cases, the results of the interface stiffness parameter for both artificially frozen soils are provided in Figure 3-8. The results show that the behavior of the interface stiffness parameter is similar to elastic modulus so as temperature decreases, the interface stiffness parameter increases. The comparison between the values of the calibrated interface stiffness parameter of Kaolinite-sand and Bentonite-sand also reveals a significant difference. The results for Bentonite-sand are around 10 times greater than Kaolinite-sand, while the elastic modulus of the Bentonite-sand is in the same order as the Kaolinite-sand which may be because of the difference in the volumetric content of the samples.



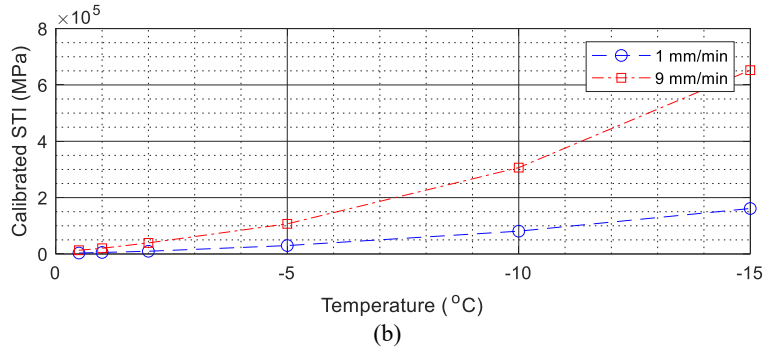


Figure 3-8 Calibrated interface stiffness parameter versus temperature (a) Kaolinite-sand and (b) Bentonite-sand

## 3.7 Discussion

### 3.7.1 Higher volumetric fraction of non-clay materials

After calibrating the interface stiffness parameters, the numerical homogenization is employed to simulate the cases with higher volumetric fractions of non-clay minerals. The RVEs are generated containing clay-water composites as matrix and non-clay minerals as inclusions. The inclusions are similar and are placed with aligned configuration like the cases depicted in Figure 3-7 and their area are calculated based on the volumetric content of the non-clay minerals. Like Section 3.6.2, the experimental data of elastic modulus and Poisson's ratio conducted by loading 1 mm/min and 9 mm/min are selected. The modeled outcomes for all cases are shown in Figure 3-9 and Figure 3-10 for Kaolinite-sand and Bentonite-sand respectively at selected temperatures (i.e.,  $-0.5^{\circ}\text{C}$ ,  $-5.0^{\circ}\text{C}$ ,  $-10^{\circ}\text{C}$ , and  $-15^{\circ}\text{C}$ ). The presented simulation data shows the rate of increase of elastic modulus of Kaolinite-sand with respect to the volume fraction of non-clay mineral is less than Bentonite-sand. Moreover, unless the simulated elastic modulus results, Poisson's ratio data displays an increasing trend as the volume fraction of clay-water composites augments. Finally, it can be found that as the temperature decreases, the Poisson's ratios converge.

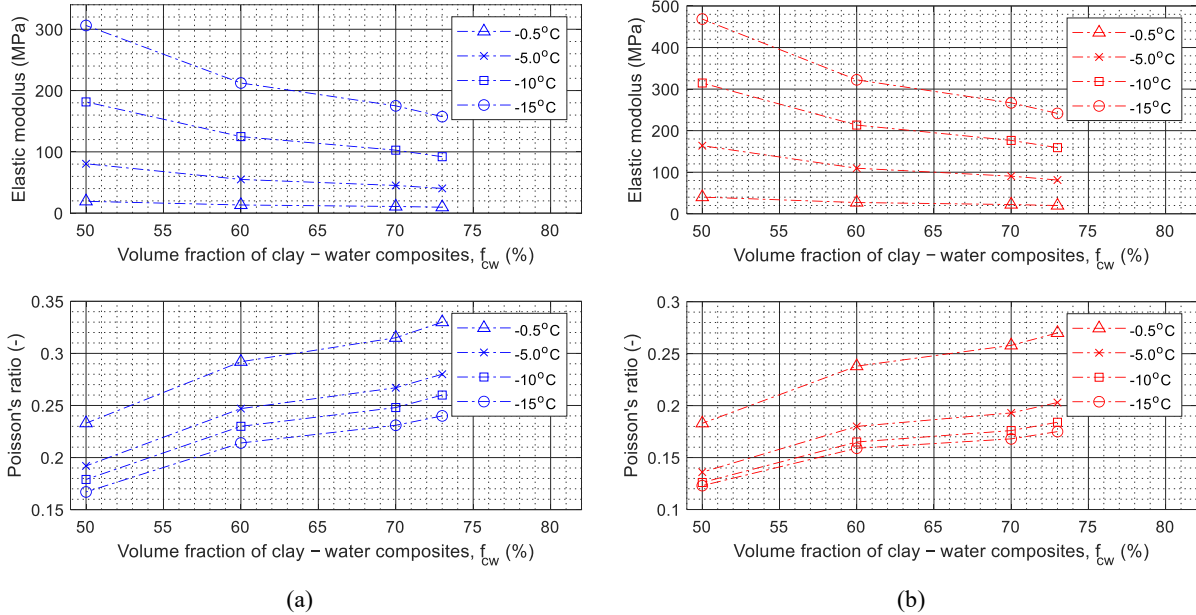


Figure 3-9 Elastic properties of Kaolinite-sand at selected temperatures with different volume fractions of clay-water composites for the cases with (a) 1 mm/min and (b) 9mm/min loading

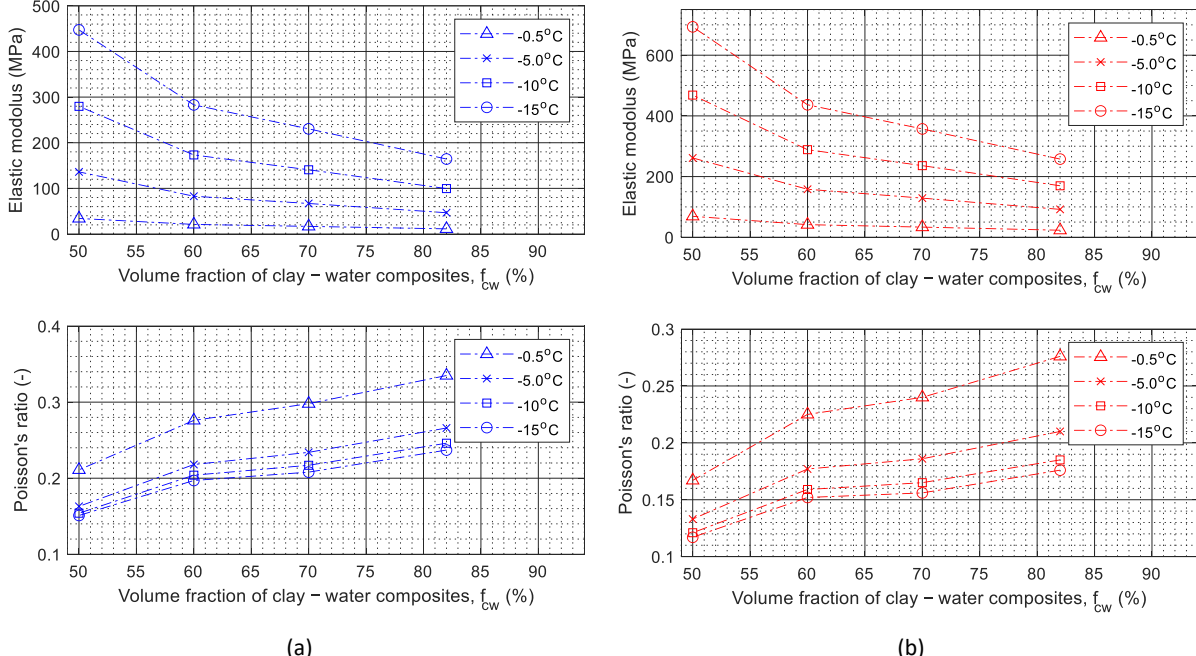


Figure 3-10 Elastic properties of Bentonite-sand at selected temperatures with different volume fractions of clay-water composites for the cases with (a) 1 mm/min and (b) 9mm/min loading

### 3.7.2 Comparison with other analytical and numerical solutions

In this section, the results of the elastic modulus for both artificially frozen sands across different volumetric fractions of clay-water composites at two temperatures (i.e.,  $T = -0.5\text{ }^{\circ}\text{C}$  and  $T = -15\text{ }^{\circ}\text{C}$ ) for the cases with 1mm/min and 9 mm/min loadings simulated are compared with the

analytical methods introduced in [Section 3.4](#). The graphs of the elastic modulus versus volume fraction of clay-water composites are drawn in [Figures 3-11](#) and [3-12](#) for Kaolinite-sand and Bentonite-sand, respectively. The comparison shows that the difference between analytical solutions and the current method is increasing as the volume fraction of clay-water composites decreases. Furthermore, the error ratio between the numerical method and analytical solution of the cases with  $T = -0.5$  °C is more than the error ratio of the cases with  $T = -15$  °C which can be inferred that the error ratio between the analytical and numerical methods decreases as the temperature drops and the elastic modulus increases.

Subsequently, the model was rerun with an exceedingly high interface stiffness parameter. This was done to simulate the elastic properties of RVEs, aiming to assess the impact of these properties in scenarios where a rigid bond exists between the non-clay minerals and the clay-water composites. The numerical meshing, the inclusion configurations within the REV, and the material properties were retained as in the XFEM models. The comparisons, as illustrated in [Figures 3-11](#) and [3-12](#), reveal that the error ratio between the XFEM and rigid bond model augments with the increasing volume fraction of non-clay minerals. Notably, for cases at  $T = -0.5$  °C, the rigid bond model appears unreliable for cases with  $f_{cw}$  of clay-water composites less than 0.7. It's also observed that the error ratio between the outcomes of the XFEM and the rigid bond model for cases with a 9 mm/min loading is lesser than for those with a 1 mm/min loading under identical conditions.

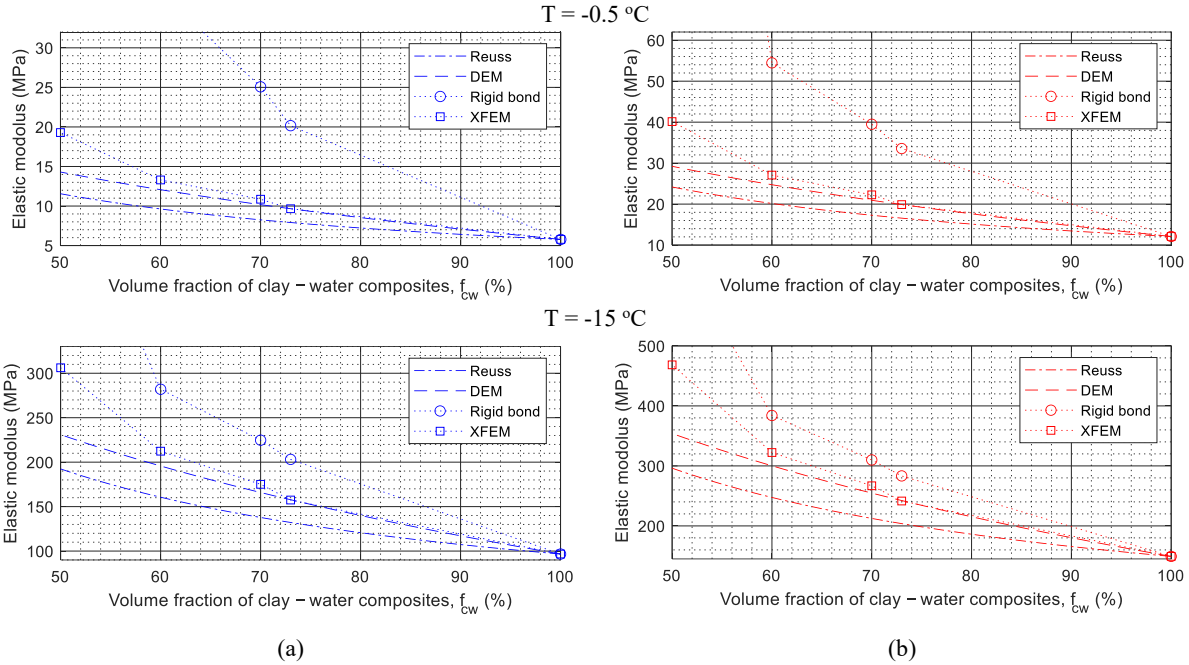


Figure 3-11 Modeling of elastic modulus of Kaolinite-sand at  $T = -0.5\text{ }^{\circ}\text{C}$  (first row) and  $T = -15\text{ }^{\circ}\text{C}$  (second row) with different volume fraction of clay-water composites: Comparison of modeled elastic modulus between Reuss, DEM, Rigid bond, and XFEM for the cases with (a) 1 mm/min and (b) 9mm/min loading

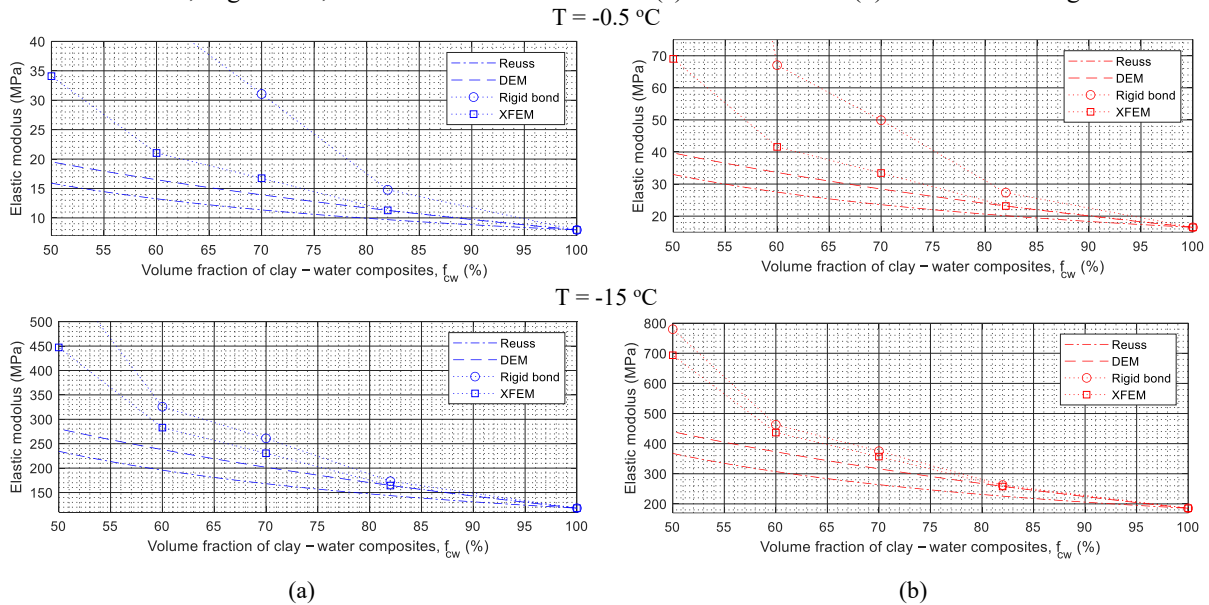


Figure 3-12 Modeling of elastic modulus of Bentonite-sand at  $T = -0.5\text{ }^{\circ}\text{C}$  (first row) and  $T = -15\text{ }^{\circ}\text{C}$  (second row) with different volume fraction of clay-water composites: Comparison of modeled elastic modulus between Reuss, DEM, Rigid bond, and XFEM for the cases with (a) 1 mm/min and (b) 9mm/min loading

### 3.7.3 Randomly generated models

As previously mentioned, to maintain generality, the inclusions were symmetrically distributed and aligned uniformly. In this section, new REV with randomly generated inclusions are

simulated, drawing from the graph depicting particle diameter of the non-clay minerals of experimental samples versus percentage passing as provided by [Girgis \(2019\)](#). These simulations use the same inputs from the modeling of the previous sections' to investigate variations in the results. Accordingly, both Kaolinite-sand and Bentonite-sand REVs were designed with inclusions generated at random. To ensure the consistency and reliability of the results, three distinct REVs, each with a different number of inclusions, were established for both types of artificially frozen sands. The methodology behind the random generation of inclusions is elaborated upon in [Nguyen et al., \(2020\)](#) and [Norouzi et al., \(2022\)](#). The configurations of these REVs are displayed in [Figure 3-13](#) for both Kaolinite-sand and Bentonite-sand.

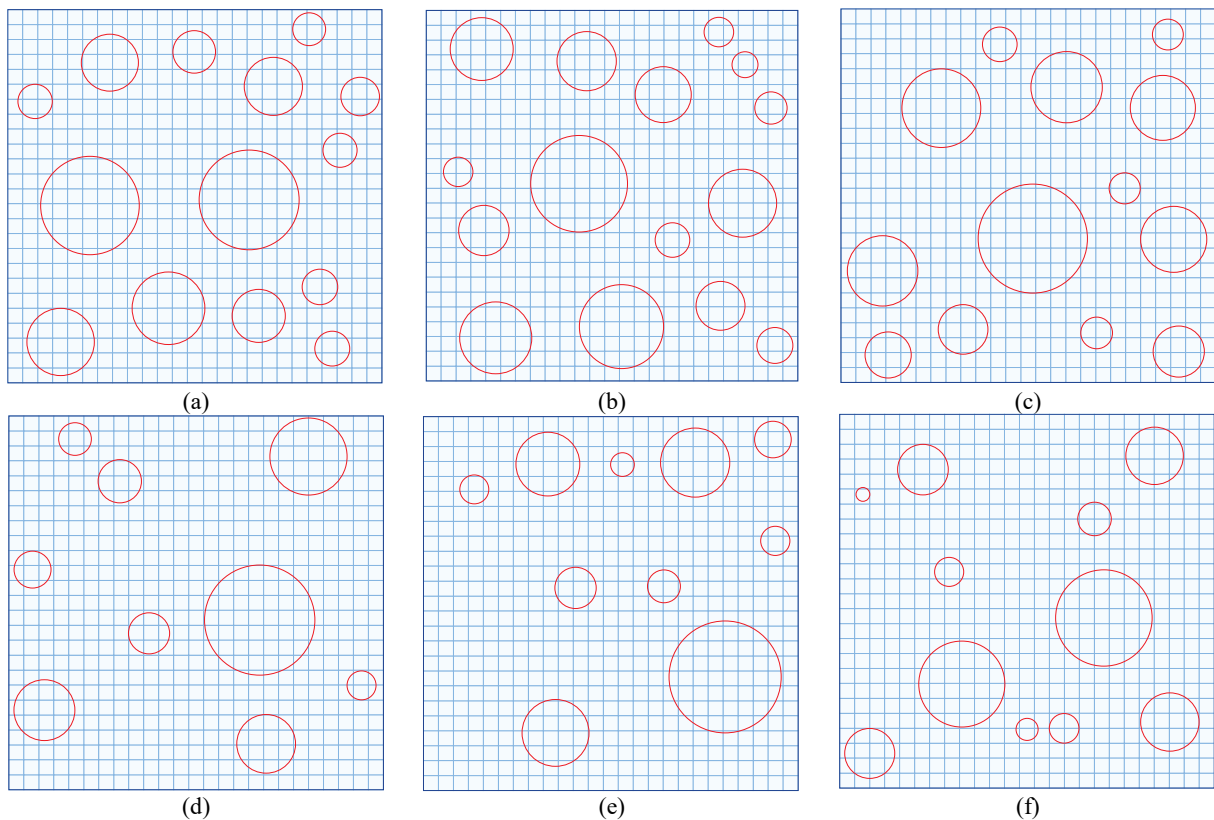


Figure 3-13 Numerical meshing of REV with randomly generated of Kaolinite-sand with  $f_{nc}=0.27$  with (a) 14, (b) 15, (c) 13 inclusions and Bentonite-sand with  $f_{nc}=0.18$  with (d) 9, (e) 10, (f) 11 inclusions.

The derived values for the elastic modulus and Poisson's ratio, corresponding to selected temperatures, are presented in [Table 3-4](#) (for Kaolinite-sand) and [Table 3-5](#) (for Bentonite-sand),

specifically for the cases with a 9mm/min loading. Given that the REV's aren't symmetrical, the homogenized elastic properties differ between horizontal and vertical orientations. Differences between the mean elastic properties and the experimental data are quantified in the last two columns of both tables.

Table 3-4 The results of simulated elastic properties of Kaolinite-sand with randomly generated inclusions in xx and yy directions and absolute error ratio with respect to experimental data at different temperatures

Temperature	Sample number	$E_{xx}$ (MPa)	$\nu_{xx}$ (-)	$E_{yy}$ (MPa)	$\nu_{yy}$ (-)	$E_{mean}$ (MPa)	$\nu_{mean}$ (-)	Error of $E_{mean}$	Error of $\nu_{mean}$
T= -0.5 °C	a	19.140	0.290	19.040	0.290	19.090	0.290	3.974%	3.333%
	b	19.170	0.289	19.050	0.289	19.110	0.289	3.873%	3.667%
	c	19.270	0.291	18.700	0.296	18.985	0.294	4.502%	2.167%
T= -5 °C	a	78.630	0.223	78.390	0.222	78.510	0.223	3.372%	3.261%
	b	78.630	0.214	78.090	0.221	78.360	0.218	3.557%	5.435%
	c	79.300	0.224	76.930	0.229	78.115	0.227	3.858%	1.522%
T= -10 °C	a	154.030	0.204	153.450	0.203	153.740	0.204	3.369%	3.095%
	b	153.670	0.205	154.030	0.204	153.850	0.205	3.300%	2.619%
	c	155.470	0.205	150.890	0.210	153.180	0.208	3.721%	1.190%
T= -15 °C	a	233.740	0.195	232.650	0.195	233.195	0.195	3.439%	2.500%
	b	233.090	0.196	233.890	0.195	233.490	0.196	3.317%	2.250%
	c	236.030	0.196	229.200	0.201	232.615	0.199	3.679%	0.750%

Table 3-5 The results of simulated elastic properties of Bentonite-sand with randomly generated inclusions in xx and yy directions and absolute error ratio with respect to experimental data at different temperatures

Temperature	Sample number	$E_{xx}$ (MPa)	$\nu_{xx}$ (-)	$E_{yy}$ (MPa)	$\nu_{yy}$ (-)	$E_{mean}$ (MPa)	$\nu_{mean}$ (-)	Error of $E_{mean}$	Error of $\nu_{mean}$
T= -0.5 °C	d	22.430	0.289	23.070	0.286	22.750	0.288	1.770%	0.862%
	e	22.860	0.286	23.330	0.284	23.095	0.285	0.281%	1.724%
	f	22.180	0.293	22.180	0.291	22.180	0.292	4.231%	0.690%
T= -5 °C	d	88.750	0.225	91.240	0.222	89.995	0.224	2.084%	0.667%
	e	90.170	0.221	92.070	0.220	91.120	0.221	0.860%	2.000%
	f	88.860	0.229	88.780	0.228	88.820	0.229	3.362%	1.556%
T= -10 °C	d	163.700	0.200	168.440	0.197	166.070	0.199	2.128%	0.750%
	e	166.270	0.196	169.830	0.195	168.050	0.196	0.961%	2.250%
	f	164.740	0.204	164.180	0.203	164.460	0.204	3.076%	1.750%
T= -15 °C	d	248.570	0.190	255.960	0.187	252.265	0.189	2.086%	0.789%
	e	252.550	0.186	257.930	0.185	255.240	0.186	0.932%	2.368%
	f	250.780	0.194	249.570	0.193	250.175	0.194	2.897%	1.842%

The errors calculated fall within an acceptable range, underlining the stability of the results. This suggests that the use of numerical homogenization, combined with the calibrated interface stiffness

parameters derived from aligned inclusions, can be effectively extended to REVs with randomly generated inclusions, while maintaining an acceptable error margin. Additionally, to highlight the influence of the temperature on the clay-water composite's stress, the von Misses stress contours for sample (c) of Kaolinite-sand are showcased in Figure 3-14. This is done across various temperatures (i.e.,  $T = -0.5\text{ }^{\circ}\text{C}$ ,  $T = -5\text{ }^{\circ}\text{C}$ ,  $T = -10\text{ }^{\circ}\text{C}$ , and  $T = -15\text{ }^{\circ}\text{C}$ ), in both horizontal and vertical orientations.

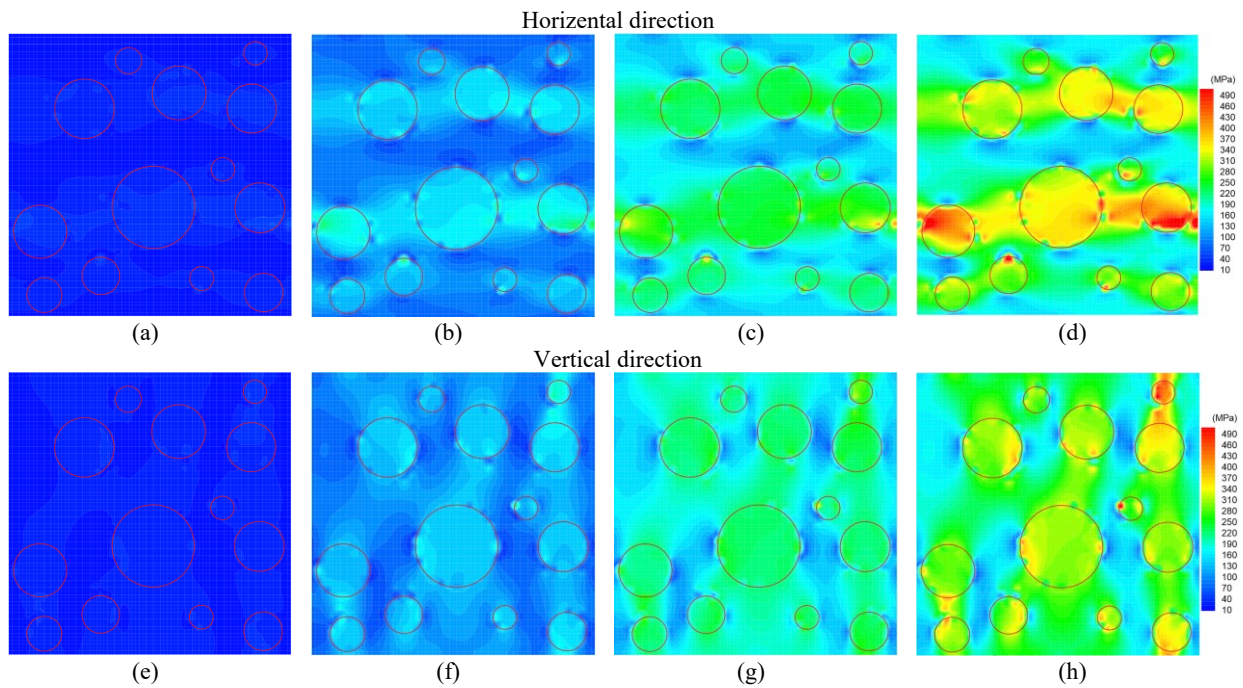


Figure 3-14 The von Misses stress contours of sample (c) of Kaolinite-sand at (a)  $T = -0.5\text{ }^{\circ}\text{C}$ , (b)  $T = -5\text{ }^{\circ}\text{C}$ , (c)  $T = -10\text{ }^{\circ}\text{C}$ , and (d)  $T = -15\text{ }^{\circ}\text{C}$  in horizontal direction and (e)  $T = -0.5\text{ }^{\circ}\text{C}$ , (f)  $T = -5\text{ }^{\circ}\text{C}$ , (g)  $T = -10\text{ }^{\circ}\text{C}$ , and (h)  $T = -15\text{ }^{\circ}\text{C}$  in vertical direction with imperfect bonding between matrix and inclusions

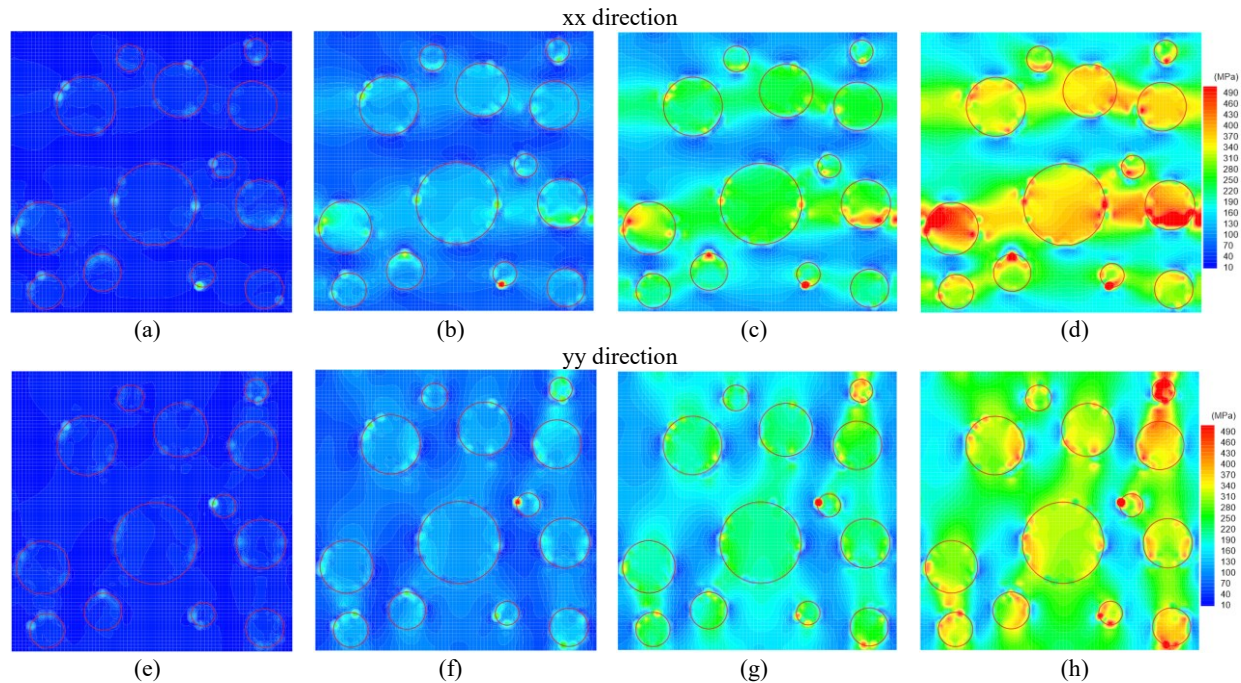


Figure 3-15 The von Mises stress contours of sample (c) of Kaolinite-sand at (a)  $T = -0.5\text{ }^{\circ}\text{C}$ , (b)  $T = -5\text{ }^{\circ}\text{C}$ , (c)  $T = -10\text{ }^{\circ}\text{C}$ , and (d)  $T = -15\text{ }^{\circ}\text{C}$  in horizontal direction and (e)  $T = -0.5\text{ }^{\circ}\text{C}$ , (f)  $T = -5\text{ }^{\circ}\text{C}$ , (g)  $T = -10\text{ }^{\circ}\text{C}$ , and (h)  $T = -15\text{ }^{\circ}\text{C}$  in vertical direction with rigid bonding between matrix and inclusions.

Figure 3-14 indicates that as the temperature reduces, the rate of increase of stress around the bonding of matrix and inclusions will be higher than the rate of stress increase within matrix and inclusion. This is because in this simulation, the elastic properties of inclusions remain constant at different temperatures. Furthermore, utilizing the XFEM, the stress concentration around the inclusions is distributed more smoothly compared to analogous cases modeled with rigid bonding, as depicted in Figure 3-15.

### 3.7.4 Limitations

While this study provides valuable insights into estimating the homogenized elastic properties of frozen soils, it is important to acknowledge its limitations. The homogenization method discussed here overlooks factors such as plasticity, the impact of ice lenses, and anisotropy, potentially compromising the accuracy of the results. Additionally, the focus solely on saturated frozen soil

samples neglects the potential differences in behavior exhibited by unsaturated frozen soils. The presence or absence of water within the soil matrix can significantly influence its mechanical properties and responses to freezing, introducing complexities that may not be fully addressed by the proposed method. Unsaturated soils may manifest distinct deformation mechanisms and hydraulic behaviors compared to their saturated counterparts under freezing conditions. As a result, the findings and conclusions of this study may not be entirely applicable to unsaturated frozen soils. Future research endeavors should aim to explore and rectify these limitations to foster a more comprehensive understanding of frozen soil mechanics.

### 3.8 Conclusions

In this paper, we present a novel method to estimate the homogenized elastic properties of frozen soils, drawing on both analytical and numerical models. The numerical approach is applied to estimate the elastic properties of two artificially frozen sandy clay samples with known temperature-dependent elastic properties. The following conclusions can be drawn from our investigations:

- The results from DEM modeling are reliable when the volume fraction of matrix or clay-water composites is higher than 0.7. For cases with a matrix volume fraction under 0.7, the results prove to be less reliable. Through an inversion approach using DEM, the elastic parameters of clay-water composites can be obtained using laboratory results on samples with  $f_{cw}$  higher than 0.7, which serves as the critical input for the subsequent numerical homogenization using XFEM.
- A 2D numerical homogenization is conducted using the XFEM by considering the imperfect bond among frozen clay-water composites and nonclay minerals. Conventional numerical homogenization approach like the FEM rigidly defines the bonding between

inclusions and the matrix. The neglect of imperfect bonds among clay-water composites and nonclay minerals will lead to unrealistic outcomes, particularly in cases with a high fraction of inclusions.

- The interface stiffness parameter, which signifies the cohesiveness between the matrix and the inclusions, has been calibrated across a range of temperatures. This calibrated interface parameter has been crucial in the application of the REVs with a significant fraction of non-clay minerals, facilitating accurate predictions of their elastic properties. The numerical homogenization model revealed insights into the behavior of the interface stiffness parameter concerning temperature variations. Unlike Poisson's ratio, the calibrated interface parameter increases as temperature decreases like elastic modulus. Moreover, the values of the interface stiffness parameter of the Bentonite-sand are considerably higher than those of Kaolinite-sand. This difference can be attributed to the differences in mineralogical composition and water content.

For simplicity, the inclusion distribution can be kept aligned and symmetric. However, when models with randomly generated inclusions were introduced, variations in the elastic properties could be noticed. Our results highlight the need to account for non-homogeneous distributions in practical applications.

## Preface to Chapter 4.

The behavior of unsaturated freezing soils poses a unique challenge in the field of geotechnical engineering, particularly in cold regions where frost actions significantly impact soil stability and infrastructure integrity. This chapter presents a comprehensive computational model to analyze the coupled thermal, hydraulic, and mechanical processes in unsaturated soils under frost conditions. Utilizing the finite element method, this study introduces a new soil freezing characteristic curve model that incorporates air-water capillary pressure and water-ice cryosuction. By verifying the model against experimental data, we demonstrate its robustness and provide a detailed discussion on the influence of different pore pressure components. This work aims to bridge the gap in our understanding of unsaturated soil behavior during freezing and thawing cycles, offering valuable insights for future research and practical applications.

## Chapter 4

# 4 Finite element modeling of thermal-hydro-mechanical coupled processes in unsaturated freezing soils considering air-water capillary pressure and cryosuction.<sup>2</sup>

### 4.1 Abstract

This paper presents a comprehensive computational model for analyzing thermo-hydro-mechanical coupled processes in unsaturated porous media under frost actions. The model employs the finite element method to simulate multiphase fluid flows, heat transfer, phase change, and deformation behaviors. A new soil freezing characteristic curve model is proposed to consider the suctions from air-water capillary pressure and water-ice cryosuction. A total pore pressure with components from liquid water pressure, air pressure, and ice pressure is used in the effective stress law. Vapor and dry air are considered miscible gases, utilizing the ideal gas law and Dalton's law. The governing equations encompass the linear momentum balance equation, the energy balance equation, and mass conservation equations for water species (ice, liquid, and vapor) and dry air. Weak forms are formulated based on primary variables of displacement, water pressure, air pressure, and temperature. The spatial discretization is achieved through the finite element method, while temporal discretization employs the fully implicit finite difference method, resulting in a

---

<sup>2</sup> A version of this manuscript has been published in the journal of *International Journal for Numerical and Analytical Methods in Geomechanics* (2024).

system of fully coupled nonlinear equations. To verify the proposed computational model, a numerical implementation is developed and validated against a set of experimental data from the literature. The successful verification demonstrates the robustness of the model. A detailed discussion of the contributions from phase change strain and different sources of pore pressure is also addressed.

**Keywords:** Unsaturated soils, frost actions, finite element method, pore pressure, thermo-hydro-mechanical coupling

## 4.2 Introduction

Frozen soils, comprising soil particles, water, ice, and air are naturally abundant in various geographical regions such as seasonal frozen and permafrost layers, arctic and subarctic zones, and loess sediments, where prolonged periods of freezing temperatures are prevalent (Kadivar and Manahiloh, 2019). Moreover, there has been a recent surge in the utilization of the Artificial Ground Freezing (AGF) technique to temporarily enhance soil bearing capacity and regulate ground and groundwater movement in civil engineering applications such as tunneling, pipelining, mining, and slope constructions (Vitel et al., 2015; Xu et al., 2019). However, the cyclic freezing and thawing poses a threat and may cause a set of Geo-Risks (e.g., infrastructure damages, subsidence, borehole failures). The concern is amplified by the impact of climate change, which brings about more frequent and severe weather events (Na and Sun, 2017). Frozen soils can be categorized as either saturated, lacking air, or unsaturated, where air is present within the medium. Freezing processes in saturated and unsaturated frozen soil can give rise to frost heave, resulting in an expansion of the soil volume. Frost heave occurs when the freezing process increases the volume of water migration and water crystallization, causing the separation of soil particles. Frost heave poses a significant risk in cold regions, often leading to engineering disasters such as pipe ruptures and foundation damage. In fully saturated soils, where all pores are already filled with pore water, the increased volume of water migration and crystallization leads to frost heave. However, in unsaturated cases, a portion of the volume expansion is initially allocated to fill the pores, with the remaining increased volume causing frost heave (Bai et al., 2020). The prediction of frost heave becomes a more intricate task, as it cannot be solely determined by variations in total water and air content. In addition, unlike saturated soil, the prediction of frost heave in unsaturated soil should consider additional physical variables such as air flux (Li et al., 2021).

The attempts to simulate frozen soil can be generally categorized to thermo-hydro (TH), thermos-mechanical (TM), and thermo-hydro-mechanical (THM) modeling (Arzanfudi and Al-Khoury, 2018). TH modeling considers mass balance and energy balance equations to study the temperature variations and water, vapor, and ice movement in the medium. To relate the governing equations, many studies have been conducted to include the complex behavior of freeze-thaw phenomena through analytical, experimental, and numerical approaches. The aspects cover phase transition, cryo-suction, and premelting dynamics (Mikkola and Hartikainen, 2001; Zhou and Meschke, 2013). To estimate the total water content in an unsaturated frozen soil, Kurylyk and Watanabe, (2013) conducted a comprehensive mathematical study to elucidate various forms of the Clapeyron equation and the connection between the soil moisture curve and soil freezing curve under both saturated and unsaturated freezing conditions. They also developed a model to estimate the hydraulic conductivity of partially frozen soil. Generally, Bi et al., (2023) examined a collection of 29 models and categorized them into four groups: theoretical models, soil water characteristic curve (SWCC)-based models, empirical models, and estimation models. Using the above constitutive relations, many TH models are developed and verified by experimental data. Mizoguchi, (1990) conducted a set of experiments to measure the variation of total water content during freezing using a vertical biaxial sample. This experiment has been employed to validate some numerical simulations (Liu and Yu, 2011; Painter, 2011; Peng et al., 2016; Stuurop et al., 2021). A list of inputs is available in a thermo-hydro numerical simulation conducted by Hansson et al., (2004). They have developed numerical simulations using a mixed formulation for both water flow and heat transport without considering vapor movement and frost heave. The combination of the Van Genuchten, (1980) soil water characteristic (SWC) curve and a modified Clapeyron equation was employed to estimate liquid and ice saturations during freezing in

unsaturated soils. A lower freezing temperature was determined for unsaturated soil due to pre-freezing pressures (suction). Additionally, [Dall'Amico et al., \(2011\)](#) suggested that the total water content could be determined independently of temperature using the van Genuchten equation. To enhance the understanding of freezing processes, it is crucial to establish comprehensive constitutive equations that describe the relationship between cryogenic suction and capillary pressure. [Painter and Karra, \(2014\)](#) proposed a constitutive relation to calculate ice, water, and air saturations for unsaturated frozen soils by considering temperature, water pressure, and air pressure. Another benchmark experimental data of soil freezing was reported by [Jame and Norum, \(1980\)](#). Similar to the previous case, they conducted a set of 1D freezing experiments but in a horizontal direction. The numerical inputs are available in [Painter, \(2011\)](#) and [Peng et al., \(2016\)](#) for different cases and boundary conditions. Using the central Finite Difference Method (FDM) to discretize the equations in both spatial and temporal, Peng's model that is based on non-equilibrium ice-water interfaces and is verified by the above-mentioned two sets of experimental data ([Peng et al., 2016](#)). Additionally, [Chen et al., \(2022\)](#) developed an improved TH-coupled model based on the Finite Element Method (FEM) model and applied it to verify their model with the experimental data by Jame and Norum. These studies primarily focus on variations in temperature and volumetric water content. Furthermore, in modeling unsaturated frozen soil, the study of vapor movement during freezing requires additional governing equations ([Gawin et al., 2019](#)). However, the effect of vapor movement on water content has been mostly neglected in the literature, with only a few studies addressing that the vapor movement cannot be neglected when initial water content is low ([He et al., 2020](#)).

Previous research on modeling frost actions in unsaturated soils mainly focused on thermo-hydraulic responses while neglecting geomechanical behavior for simplicity. By adding the

momentum balance equation to the system of coupling equations, the deformation and stress changes of the medium can be identified. The current THM models for frozen soils are mainly developed for fully saturated frozen geomaterials ([Arzanfudi and Al-Khoury, 2018](#); [Koniorczyk et al., 2015](#); [Thomas et al., 2009](#); [Yang et al., 2015](#)). Among these THM models for frozen soils, [Nishimura et al., \(2009\)](#) derived a formulation and numerically applied a fully coupled THM analysis of elastoplastic water-saturated frozen soils, considering the freezing and thawing processes by incorporating the concept of cryo-suction. [Bekele et al., \(2017\)](#) developed a numerical model to estimate frost heave in saturated porous media using the Isogeometric Analysis (IGA) technique. Recently, there has been increased attention given to coupled THM models for unsaturated soils ([Liu and Yu, 2011](#); [Teng et al., 2020](#)). [Bai et al., \(2020\)](#) proposed a frost heave model for saturated-unsaturated soils by introducing an effective strain ratio to establish the relationship between frost heave strain in unsaturated soils and the fields of moisture and temperature. The back-calculated effective strain ratio was incorporated into the displacement equations, and the results were verified against their experimental data, although their model did not consider pore pressure. [Huang and Rudolph, \(2021\)](#) presented a THM model to analyze frost heave in variably saturated freezing soils. The gas phase contains vapor, and the transport of dry air was neglected for simplicity. The model was verified using laboratory test data from the literature. The void ratio was used as a dependent variable to demonstrate the link between ice lens segregation, stress-deformation, and the evolution of the void ratio. Li et al. validated their numerical model with Mizoguchi's experimental data and their comprehensive uniaxial experiments ([Li et al., 2021](#)). Water content, vapor, and temperature variations as well as the frost heave were included in their numerical results. Similarly, [Wu and Ishikawa, \(2022\)](#) developed a thermo-hydro-mechanical model to simulate the freezing process of partially saturated frost

susceptible soils in Hokkaido. Their multiphysics simulations aligned well with frost heave tests on Touryo soil and Fujinomori soil, indicating that the frost heave ratio is proportional to the initial degree of saturation and inversely proportional to the cooling rate and overburden pressure. Nevertheless, previous models have not adequately characterized pore water, pore ice pressure, and pore air pressure, resulting in an unclear definition of the effective stress law. Model formulations have varied significantly due to different researchers' backgrounds (Gawin et al., 2020). There is a lack of a comprehensive and inclusive finite element formulation for describing the thermal-hydro-mechanical coupled processes in unsaturated freezing soils considering pore pressure components from liquid water, air, and ice (Li et al., 2024).

In this study, we propose a novel fully coupled THM numerical model, implemented within a finite element framework, to simulate the frost actions in unsaturated porous media. A new soil freezing characteristic curve (SFCC) model is applied to consider the suctions from air-water capillary pressure and water-ice cryosuction. Thus, liquid water pressure, air pressure, and ice pressure are treated as parts of the total pore pressure. The general governing equations of THM coupling are derived based on the fundamentals of continuum mechanics. The spatial discretization of the governing equations is performed using the FEM and the time-dependent equations are solved using the FDM. To demonstrate the efficacy of the developed equations and numerical code, data from a recently published experimental test is used for validation.

### **4.3 Mathematical models of unsaturated frozen medium**

This section covers the basic physical properties or models that serve as the fundamentals of THM-coupled processes in an unsaturated frozen soil. A notation list of parameters is presented in Appendix A. Similar formulations can be found in other theoretical developments for porous media (Khoei and Mortazavi, 2020; Mortazavi et al., 2023).

### 4.3.1 Volumetric relation

The volumetric content of each phase, denoted by  $\theta_\alpha$ , is determined by dividing the volume of that specific phase ( $\alpha$ ) by the total volume ( $V$ ). The phases considered include soil ( $s$ ), water ( $w$ ), ice ( $i$ ), and moist air ( $g$ ).

$$\theta_\alpha = \frac{V_\alpha}{V} \quad (4.26)$$

Moreover, porosity is defined as the ratio of void volume (i.e.,  $V_{void} = V - V_s$ ) to the total volume:

$$n = \frac{V_{void}}{V} \quad (4.27)$$

The saturation of water, ice, and air, denoted as  $S_\alpha$ , can be expressed as the respective volume ratio divided by the porosity as follows:

$$S_\alpha = \frac{\theta_\alpha}{n} = \frac{V_\alpha}{V_{void}}, \quad \alpha = w, g, i \quad (4.28)$$

The summation of saturations is unity. Figure 4-1 shows the components of an unsaturated frozen soil and their corresponding volumetric ratios.

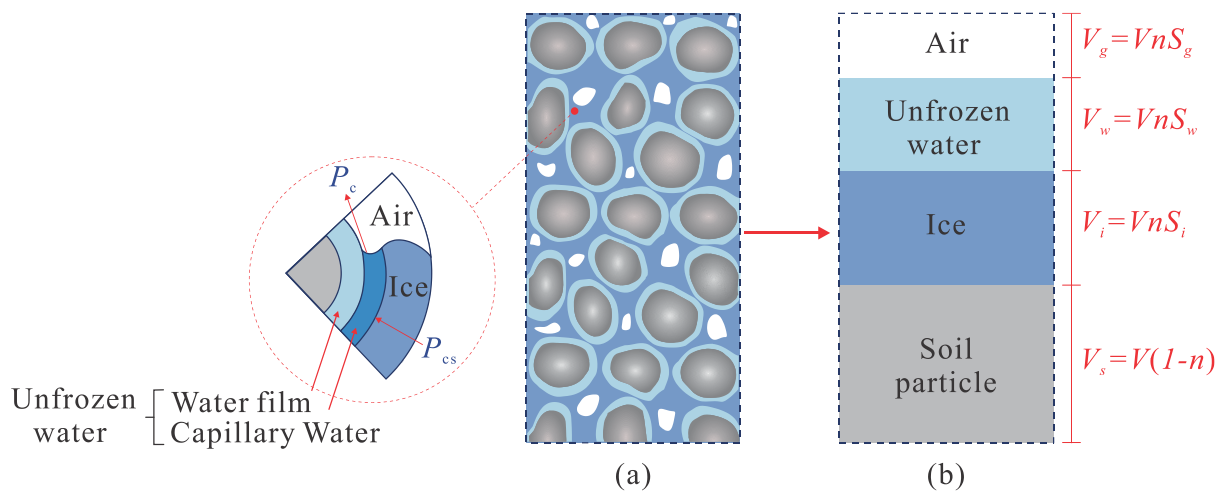


Figure 4-1 Sketch showing the configuration of different phases of an unsaturated frozen soil.

### 4.3.2 Capillary pressure

According to the capillary theory, the discontinuity pressure between air pressure and pore water pressure in an unsaturated soil can be written as:

$$P_c = P_g - P_w \quad (4.29)$$

in which  $P_c$ ,  $P_g$ , and  $P_w$  are air-water capillary pressure, moist air pressure, and water pressure, respectively. A similar relation between ice pressure ( $P_i$ ) and pore water pressure in a partially frozen soil ( $P_{wf}$ ) can be written for the cryosuction pressure  $P_{cs}$ :

$$P_{cs} = P_i - P_{wf} \quad (4.30)$$

Defining  $\beta$  as the ratio of ice-liquid to liquid-air surface tensions which can be either 1.0 for solid–liquid–solid (SLS) soils or 2.2 for solid-to-solid (SS) soils (Kurylyk and Watanabe, 2013), we have (Painter and Karra, 2014):

$$P_{cs} = \frac{P_c}{\beta} \quad (4.31)$$

The SS soil is characterized by the absence of colloidal materials and consists of soil types like sand, silt, or coarse clay fractions where particles have direct solid-to-solid (SS) contacts. On the other hand, SLS soil represents a scenario where soil particles are consistently separated by liquid water. SLS soil typically involves clay-water composites. According to Kurylyk and Watanabe, (2013), the  $\beta$  coefficient is dependent on the interface energies from different interface components in an unsaturated frozen soil.

The modified Clausius-Clapeyron equation describes the relationship between temperature, ice pressure, and pore water pressure in partially frozen soil. The equation is as follows (Kay and Groenevelt, 1974):

$$\frac{L_f}{T_0} dT = \frac{dP_{wf}}{\rho_w} - \frac{dP_i}{\rho_i} \quad (4.32)$$

In Equation (4.32),  $\rho_w$  and  $\rho_i$  are the densities of water and ice respectively.  $L_f$  is the latent heat,  $T$  is the temperature, and  $T_0 = 273.15$  K represents the reference temperature. Through the integration of the above differential equation of equilibrium and assuming that ice pressure at freezing point equals air pressure, the following equations can be obtained to quantify the freezing point temperature:

$$\frac{L_f}{T_0} (T_f - T_0) = \frac{P_{wf}}{\rho_w} - \frac{P_i}{\rho_i} \quad (4.33)$$

where  $T_f$  is the freezing point temperature which can be calculated by assuming  $\rho_w \cong \rho_i$ :

$$T_f = T_0 - \frac{T_0}{L_f \rho_w} \frac{P_c}{\beta} \quad (4.34)$$

### 4.3.3 SWCC and SFCC

As mentioned in the introduction, to find water, ice, and air saturations in an unsaturated frozen medium, many soil freezing characteristic curve (SFCC) models have been proposed in the literature and most of them are soil water characteristic curve (SWCC)-based models. However, previous SFCC models mainly consider temperature as a dependent variable for calculating ice saturation results (Huang and Rudolph, 2021). The neglect of the dependency of ice saturation on air-water capillary pressure will bring numerical issues because the partial derivative term of ice saturation over capillary pressure is needed in the numerical implementation. In this study, we intend to solve this numerical issue by introducing an SFCC model with the consideration of air-water capillary pressure and temperature.

Introducing the volumetric total water content as  $\theta_{tw} = \theta_w + \frac{\rho_i}{\rho_w}\theta_i$ , the model of [Van Genuchten, \(1980\)](#) is employed in this study, to estimate the water, ice, and air saturations as a function of capillary pressure and temperature. The model is presented as:

- Above freezing point temperature ( $T > T_f$ ), ice content is zero. Therefore, total water content equals volumetric water content:

$$\theta_w = \theta_r + (\theta_s - \theta_r)(1 + [\alpha_v P_c]^{n_v})^{-m_v} \quad (4.35)$$

$$S_w = \frac{\theta_w}{n}, \quad S_g = 1 - S_w$$

- Under freezing point temperature ( $T < T_f$ ), we have:

$$\theta_{tw} = \theta_r + (\theta_s - \theta_r) \left( 1 + \left[ \alpha_v \frac{P_c}{\beta} \right]^{n_v} \right)^{-m_v}$$

$$\theta_w = \theta_r + (\theta_s - \theta_r) \left( 1 + \left[ \alpha_v \left( \frac{P_c}{\beta} + \rho_w \frac{L_f}{T_0} (T_f - T) \right) \right]^{n_v} \right)^{-m_v} \quad (4.36)$$

$$\theta_i = \frac{\rho_w}{\rho_i} (\theta_{tw} - \theta_w)$$

$$S_w = \frac{\theta_w}{n}, \quad S_i = \frac{\theta_i}{n}, \quad S_g = 1 - S_w - S_i$$

in which,  $\alpha_v$ ,  $m_v$ , and  $n_v$  are the curve fitting parameters. It should be noted that the total suction pressure in [Equation 4.11](#) contains the component from air-water capillary pressure and the component from cryosuction (quantifying using the Clausius-Clapeyron equation). The component from cryosuction is approximated using  $\rho_w \frac{L_f}{T_0} (T_f - T)$ . The introduction of  $\frac{P_c}{\beta}$  in [Equation 4.11](#) can be treated as converting the capillary pressure to an equivalent amount of

cryosuction pressure, thus, to consistently apply the SFCC. When we only include  $\frac{P_c}{\beta}$  as suction, ice will be treated as a part of water, thus allowing the determination of the total water content  $\theta_{tw}$ . In contrast, if both air-water capillary pressure and cryosuction are included in the van Genuchten model, the liquid water content  $\theta_w$  can be derived. The inclusion of  $P_c$  term in Equation 4.11 will generate reasonable values for the term of  $\frac{\partial S_i}{\partial P_c}$  in the subsequent FEM formulation.

According to the Dalton's law, (Moran et al., 2010) moist air pressure is a combination of dry air ( $ga$ ) pressure and vapor ( $gw$ ) pressure, the pressure of moist air can be expressed as (Lewis and Schrefler, 1998):

$$P_g = P_{gw} + P_{ga} \quad (4.37)$$

where  $P_{gw}$  and  $P_{ga}$  are the vapor pressure and dry air pressure, respectively. Vapor pressure can be calculated using the Kelvin-Laplace law by defining relative humidity as follows (Khoei et al., 2021):

$$h_r = \frac{P_{gw}}{P_{gws}} = \exp\left(-\frac{P_c M_w}{\rho_w T R}\right) \quad (4.38)$$

In Equation 4.13,  $P_{gws}$  is saturated vapor pressure as a function of temperature. In this study, we assume that the moist air behaves as a perfect gas following the ideal gas law to find dry and vapor densities (Lewis and Schrefler, 1998):

$$\rho_{ga} = \frac{P_{ga} M_a}{T R}, \quad \rho_{gw} = \frac{P_{gw} M_w}{T R}, \quad \rho_g = \rho_{ga} + \rho_{gw} \quad (4.39)$$

where  $M_a$  and  $M_w$  are the molar masses of the constituents of dry air and water; R is the universal gas constant, and  $\rho_g$  is the density of moist air.

#### 4.3.4 Darcy's law

The hydraulic conductivity of the porous medium changes continuously during the freezing/thawing process depending on the degree of water saturation i.e., as a function of temperature and capillary pressure. To calculate the hydraulic conductivity at a given temperature, a relative hydraulic conductivity parameter is introduced into the Darcy's law: During freezing, a part of wider pores is closed by frozen water. Nevertheless, at the macro-scale level, the volume-averaged advective flux of liquid water (i.e. caused by pressure gradients) still can be described by the Darcy's law (Gawin et al., 2019):

$$nS_{\kappa}\mathbf{v}_{\kappa,S} = \frac{\mathbf{k}k_{r\kappa}}{\mu_{\kappa}}(-\nabla P_{\kappa} + \rho_{\kappa}\mathbf{g}), \quad \kappa = w, g \quad (4.40)$$

in which  $\mathbf{k} = k\mathbf{I}$  represents intrinsic permeability while  $\mathbf{I}$  is the identity matrix. Additionally,  $\mu_{\kappa}$  is viscosity,  $\mathbf{g}$  is the acceleration due to gravity, and  $k_{r\kappa}$  is the relative permeability of  $\kappa$ . Considering the effect of freezing, the relative permeability for water and air is given as:

$$k_{rw} = \Omega_v \sqrt{S_e} \left[ 1 - \left( 1 - S_e^{\frac{1}{m_v}} \right)^{m_v} \right]^2 \quad (4.41)$$

$$k_{rg} = \sqrt{1 - S_e} \left( 1 - S_e^{\frac{1}{m_v}} \right)^{2m_v} \quad (4.42)$$

In Equation 4.16,  $\Omega_v = 10^{-E_v Q}$  is the phenomenological impedance factor of ice that reduces the hydraulic conductivity of soil, where  $E_v$  is an empirical constant and  $Q = \frac{\rho_i \theta_i}{\rho_w \theta_{tw}}$  is the mass ratio of ice over the total water (Hansson et al., 2004; Kurylyk and Watanabe, 2013).

### 4.3.5 Fick's law

To explain the diffusive-dispersive mass flux, the Fick's law is employed for dry air and water vapor phases (Lewis and Schrefler, 1998):

$$\mathbf{J}_g^\kappa = -\rho_g \mathbf{D}_\kappa \nabla \left( \frac{\rho_\kappa}{\rho_g} \right), \quad \kappa = gw, ga \quad (4.43)$$

where  $\mathbf{D}_\kappa$  is the effective dispersion tensor of the diffusing phase and can be proven that  $\mathbf{D}_{gw} = \mathbf{D}_{ga}$  since (Lewis and Schrefler, 1998):

$$\nabla \left( \frac{\rho_{ga}}{\rho_g} \right) = -\nabla \left( \frac{\rho_{gw}}{\rho_g} \right) \quad (4.44)$$

Equation 4.18 can be rewritten as follows:

$$\mathbf{J}_g^{gw} = \rho_g \frac{M_a M_w}{M_g^2} \mathbf{D}_{gw} \nabla \left( \frac{P_{gw}}{P_g} \right) = -\mathbf{J}_g^{ga} \quad (4.45)$$

in which,  $M_g$  is the molar mass of the gas phase and can be found as:

$$M_g = \left( \frac{\rho_{gw}}{\rho_g} \frac{1}{M_w} + \frac{\rho_{ga}}{\rho_g} \frac{1}{M_a} \right)^{-1} \quad (4.46)$$

### 4.3.6 Fourier's law

Conductive heat flux in materials below the freezing point of water is assumed to follow Fourier's law (Gawin et al., 2019):

$$\tilde{\mathbf{q}} = -\lambda_{\text{eff}} \nabla T \quad (4.47)$$

Here,  $\lambda_{\text{eff}}$  is the overall thermal conductivity of porous media which is a function of the thermal conductivity of each phase and their corresponding volumetric fractions (Li et al., 2021):

$$\lambda_{\text{eff}} = \lambda_s^{1-n} \lambda_w^{nS_w} \lambda_g^{nS_g} \lambda_i^{nS_i} \quad (4.48)$$

#### 4.3.7 Material nonlinearity

In this paper, to incorporate the nonlinear behavior of unsaturated frozen soil, an associative Drucker-Prager model has been chosen (Drucker and Prager, 1952). The yield function ( $\Pi$ ) is defined as (de Souza Neto et al., 2011):

$$\Pi(\boldsymbol{\sigma}', c) = \sqrt{\frac{1}{2} \mathbf{s}(\boldsymbol{\sigma}') : \mathbf{s}(\boldsymbol{\sigma}') + \eta p'(\boldsymbol{\sigma}') - \xi c} \quad (4.49)$$

where  $\boldsymbol{\sigma}'$ ,  $\mathbf{s}$ , and  $p'$  are effective stress, deviatoric stress, and hydrostatic pressure, and  $c$  is cohesion. The selection of parameters  $\eta$  and  $\xi$  is based on the approximation of the Mohr-Coulomb plasticity model (Sanei et al., 2022). For a 2D plane strain model, these parameters are expressed as:

$$\eta = \frac{3 \tan \phi}{\sqrt{9 + 12 \tan \phi}} \quad (4.50)$$

$$\xi = \frac{3}{\sqrt{9 + 12 \tan \phi}}$$

where  $\phi$  is the friction angle. To correct the stress-strain relation, two return-mapping algorithms are utilized for smooth portions of the cone and its apex. The details of stress-strain correction and the derivation of the tangential stiffness matrix are described in de Souza Neto et al., (2011). Previous experimental results have demonstrated that the plasticity parameters of the constitutive model are highly dependent on the applied temperature Girgis et al., (2020). The hardening parameters can be explicitly considered in the numerical modeling by including temperature (Yu et al., 2022; Zhang and Michalowski, 2015).

### 4.3.8 Elasticity in a partially saturated frozen soil

According to [Bekele et al., \(2017\)](#), the following relation can be used to relate effective stress and effective strain:

$$d\boldsymbol{\sigma}' = \mathbf{D}_T(d\boldsymbol{\varepsilon} - d\boldsymbol{\varepsilon}^{\text{ph}} - d\boldsymbol{\varepsilon}^T) \quad (4.51)$$

where  $\boldsymbol{\sigma}'$  represents the effective stress vector,  $\mathbf{D}_T$  is the tangential constitutive matrix, and  $d\boldsymbol{\varepsilon}$  represents the total strain increment vector. Moreover, the increment strain due to phase change ( $d\boldsymbol{\varepsilon}^{\text{ph}}$ ) for unsaturated freezing condition is modified as:

$$d\boldsymbol{\varepsilon}^{\text{ph}} \cong \frac{\beta_{\text{ph}}}{3} \left( \frac{n(\rho_w - \rho_i)}{\rho_w S_w + \rho_i S_i} dS_i \right) \mathbf{I} \quad (4.52)$$

The relation is developed based on the mass balance of water and ice during the phase, where,  $\beta_{\text{ph}}$  ( $0 < \beta_{\text{ph}} < 1$ ) is the adjustment coefficient for unsaturated porous media that can be assigned an approximate value equivalent to the initial water saturation. The application of the strain increment herein mirrors the concept of integrating a porosity evolution term due to water-ice phase change ([Michalowski and Zhu, 2006](#); [Vosoughian and Balieu, 2023](#)).

Considering  $\beta_s$  as the thermal expansion coefficient of the solid skeleton, a linear relation can be used to calculate the thermal elastic strain increment ( $d\boldsymbol{\varepsilon}^T$ ) ([Bekele et al., 2017](#); [Lewis and Schrefler, 1998](#)):

$$d\boldsymbol{\varepsilon}^T = \frac{\beta_s}{3} dT \mathbf{I} \quad (4.53)$$

## 4.4 Balance equations

This section presents the fundamental form of the governing equations for porous media, specifically focusing on the phase change induced by freezing and thawing processes. These

processes can be effectively modeled using THM analysis, which considers the interactions between the different phases involved.

#### 4.4.1 Linear momentum balance equation

Equation 4.29 represents the conservation of linear momentum in the porous media, which states the balance between the divergence of the total stress tensor ( $\boldsymbol{\sigma}$ ) and body force ( $\mathbf{b}$ ):

$$\nabla \cdot \boldsymbol{\sigma} + \mathbf{b} = \mathbf{0} \quad (4.54)$$

where  $\nabla = \langle \partial/\partial x \quad \partial/\partial y \quad \partial/\partial z \rangle$  represents the gradient operator and "." denotes the dot product.

According to Yin et al., (2023), the total stress can be approximated using the effective stress and pore pressure components:

$$\boldsymbol{\sigma} = \boldsymbol{\sigma}' - S_w P_w \mathbf{I} - S_g P_g \mathbf{I} - S_i P_i \mathbf{I} \quad (4.55)$$

where  $\boldsymbol{\sigma}'$  is the effective stress. Thus, in Equation 4.30, saturations of individual components (fluid water, air, and ice) are used as weight coefficients for their pore pressure components.

#### 4.4.2 Mass balance equations

The general equation for the conservation of mass for each phase is given by:

$$\frac{D}{Dt} (\theta_\alpha \rho_\alpha) + \theta_\alpha \rho_\alpha \nabla \cdot \mathbf{v}_\alpha - \dot{m}_\alpha = 0, \quad \alpha = s, w, i, g \quad (4.56)$$

In Equation 4.31,  $D(*)/Dt = \nabla(*) \cdot \mathbf{u} + \partial(*)/\partial t$  is the material time derivation (Khoei et al., 2021),  $\mathbf{v}_\alpha$  and  $\rho_\alpha$  represents the velocity and density of the  $\alpha$  phase, and  $\dot{m}_\alpha$  is the rate of increase or decrease of mass per volume for the  $\alpha$  phase.

By combining the conservation of mass equations for water, ice, and vapor, and assuming that the rates of mass change for water and ice are equal but with opposite signs during freezing and thawing (i.e.,  $\dot{m}_i = -\dot{m}_w$ ), the following equation can be obtained (Gawin et al., 2020):

$$\begin{aligned}
nS_g \frac{\partial \rho_{gw}}{\partial t} + n\rho_{gw} \frac{\partial S_g}{\partial t} + n\rho_w \frac{\partial S_w}{\partial t} + n\rho_i \frac{\partial S_i}{\partial t} - \nabla \cdot \left( \rho_g \frac{M_a M_w}{M_g^2} \mathbf{D}_{gw} \nabla \left( \frac{P_{gw}}{P_g} \right) \right) \\
- \nabla \cdot \left( \rho_w \frac{\mathbf{k}k_{rw}}{\mu_w} (\nabla P_w - \rho_w \mathbf{g}) \right) - \nabla \cdot \left( \rho_{gw} \frac{\mathbf{k}k_{rg}}{\mu_g} (\nabla P_g - \rho_g \mathbf{g}) \right) \\
- \beta_{swgi} \frac{\partial T}{\partial t} + (S_w \rho_w + S_g \rho_{gw} + S_i \rho_i) \nabla \cdot \mathbf{v}_s = 0
\end{aligned} \tag{4.57}$$

It should be noted that water evaporation/condensation rate is neglected in the mass balance of Equation 4.32.

The mass balance equation for dry air can be written as (Gawin et al., 2020):

$$\begin{aligned}
nS_g \frac{\partial \rho_{ga}}{\partial t} + n\rho_{ga} \frac{\partial S_g}{\partial t} + S_g \rho_{ga} \nabla \cdot \mathbf{v}_s + \nabla \cdot \left( \rho_g \frac{M_a M_w}{M_g^2} \mathbf{D}_{gw} \nabla \left( \frac{P_{gw}}{P_g} \right) \right) - \nabla \\
\cdot \left( \rho_{ga} \frac{\mathbf{k}k_{rg}}{\mu_g} (\nabla P_g - \rho_g \mathbf{g}) \right) - \beta_{sg} \frac{\partial T}{\partial t} = 0
\end{aligned} \tag{4.58}$$

In the above equations, the velocity of solid particle is given by  $\mathbf{v}_s = \frac{d\mathbf{u}}{dt}$  with  $\mathbf{u}$  as the displacement of the medium. In addition, the terms  $\beta_{swgi}$  and  $\beta_{sg}$  represent the equivalent thermal expansion coefficients for the mass changes of the unsaturated frozen soil and solid air mixture:

$$\beta_{swgi} = (1 - n)(\rho_{gw} S_g + \rho_w S_w) \beta_s + n\rho_w S_w \beta_w + n\rho_i S_i \beta_i \tag{4.59}$$

$$\beta_{sg} = (1 - n) S_g \rho_{ga} \beta_s \tag{4.60}$$

### 4.4.3 Energy balance equation

It is assumed that all the phases are locally in a state of thermodynamic equilibrium and the change in thermal state caused by the liquid water evaporation–desorption is neglected. Thus, the energy balance equation of the medium can be derived as (Li et al., 2021):

$$(\rho C_p)_{\text{eff}} \frac{\partial T}{\partial t} + \mathbf{a} \cdot \nabla T - \nabla \cdot (\lambda_{\text{eff}} \nabla T) + L_w \rho_w \frac{\partial \theta_v}{\partial t} - L_f \rho_i \frac{\partial \theta_i}{\partial t} = 0 \quad (4.61)$$

Here,  $L_w$  and  $L_f$  are latent heat coefficients for the water-vapor phase change and the water-ice phase change, respectively. In Equation 4.36, the heat transfer between the phases is neglected and it is assumed that the time rate of vapor content is almost zero (i.e.,  $\frac{\partial \theta_v}{\partial t} \cong 0$ ). The equivalent heat capacity  $(\rho C_p)_{\text{eff}}$  is defined as (Li et al., 2021):

$$(\rho C_p)_{\text{eff}} = (1 - n) \rho_s C_p^s + n S_w \rho_w C_p^w + n S_g \rho_g C_p^g + n S_i \rho_i C_p^i \quad (4.62)$$

Additionally,  $\mathbf{a}$  is the vector of advection of heat transfer in Equation 4.36, which is a function of relative velocities of water-solid  $\mathbf{v}_{w,s}$  and air-solid  $\mathbf{v}_{g,s}$ :

$$\mathbf{a} = n S_w \rho_w C_p^w \mathbf{v}_{w,s} + n S_g \rho_g C_p^g \mathbf{v}_{g,s} \quad (4.63)$$

## 4.5 Variational formulations

In this study, displacement, pore water pressure, pore air pressure, and temperature are taken as primary variables. Accordingly, the initial conditions are defined as:

$$\mathbf{u} = \mathbf{u}^0, P_w = P_w^0, P_g = P_g^0, T = T^0 \text{ on } \Omega \quad (4.64)$$

where,  $\Omega$  is the problem domain bounded by the boundary  $\Gamma$ . As shown in Figure 4-2, the boundary conditions could be either Dirichlet boundary conditions ( $\Gamma_D$ ) for predefined values or Neumann boundary conditions ( $\Gamma_N$ ) for traction and fluxes. Note that  $\Gamma_D \cup \Gamma_N = \Gamma$  and  $\Gamma_D \cap \Gamma_N = \emptyset$ .

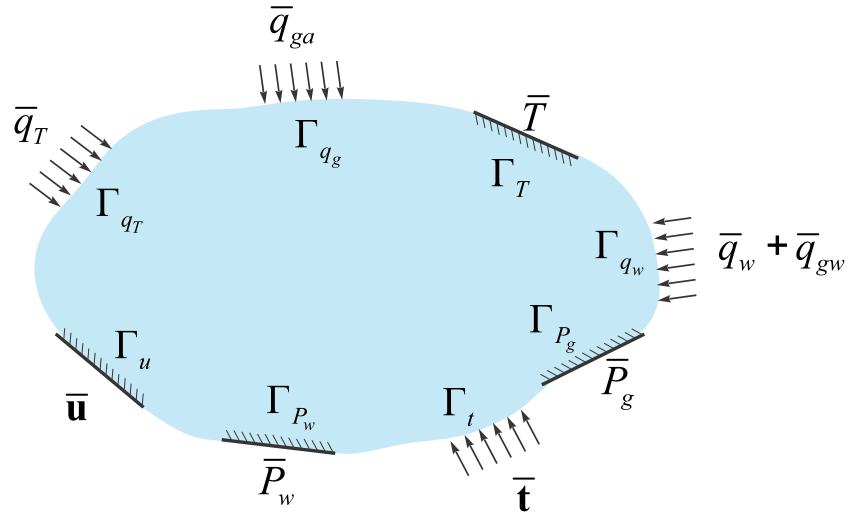


Figure 4-2 Sketch showing the problem domain and boundary conditions with primary variables (modified after (Khoei and Mortazavi, (2020))).

- Dirichlet boundary conditions are expressed as follows:

$$\begin{aligned}
 \mathbf{u} &= \bar{\mathbf{u}} && \text{on } \Gamma_u \\
 P_w &= \bar{P}_w && \text{on } \Gamma_{P_w} \\
 P_g &= \bar{P}_g && \text{on } \Gamma_{P_g} \\
 T &= \bar{T} && \text{on } \Gamma_T
 \end{aligned} \tag{4.65}$$

in which the prescribed values of primary variables (i.e.,  $\bar{\mathbf{u}}$ ,  $\bar{P}_w$ ,  $\bar{P}_g$ ,  $\bar{T}$ ) are imposed on the essential boundary conditions  $\Gamma_u$ ,  $\Gamma_{P_w}$ ,  $\Gamma_{P_g}$ , and  $\Gamma_T$ , respectively.

- Neumann boundary conditions are defined as:

$$\boldsymbol{\sigma} \cdot \mathbf{n}_\Gamma = \bar{\mathbf{t}} \quad \text{on } \Gamma_t \tag{4.66}$$

$$\begin{aligned}
& \left[ -\rho_w \frac{\mathbf{k}k_{rw}}{\mu_w} (\nabla P_w - \rho_w \mathbf{g}) - \rho_{gw} \frac{\mathbf{k}k_{rg}}{\mu_g} (\nabla P_g - \rho_g \mathbf{g}) \right. \\
& \quad \left. + \rho_g \frac{M_a M_w}{M_g^2} \mathbf{D}_{gw} \nabla \left( \frac{P_{gw}}{P_g} \right) \right] \cdot \mathbf{n}_\Gamma = \bar{q}_w + \bar{q}_{gw} && \text{on } \Gamma_{q_w} \\
& \left[ -\rho_{ga} \frac{\mathbf{k}k_{rg}}{\mu_g} (\nabla P_g - \rho_g \mathbf{g}) - \rho_g \frac{M_a M_w}{M_g^2} \mathbf{D}_{gw} \nabla \left( \frac{P_{gw}}{P_g} \right) \right] \cdot \mathbf{n}_\Gamma = \bar{q}_{ga} && \text{on } \Gamma_{q_g} \\
& -(\lambda_{\text{eff}} \nabla T) \cdot \mathbf{n}_\Gamma = \bar{q}_T && \text{on } \Gamma_{q_T}
\end{aligned}$$

Here,  $\mathbf{n}_\Gamma$  represents the unit outward vector normal to the boundary.  $\bar{\mathbf{t}}$  denotes the traction, and  $\bar{q}_w$ ,  $\bar{q}_{gw}$ ,  $\bar{q}_{ga}$ , and  $\bar{q}_T$  are water pressure, vapor pressure, dry air pressure, and thermal fluxes respectively on their corresponding natural boundary conditions (i.e.,  $\Gamma_t$ ,  $\Gamma_{q_w}$ ,  $\Gamma_{q_g}$ ,  $\Gamma_{q_T}$ ).

To solve the governing equations, the weak form of the equations is obtained by integrating the strong forms (i.e., [Equations 4.29](#), [4.32](#), [4.33](#), and [4.36](#)) over the domain and multiplying them by their corresponding admissible test functions ( $\mathbf{W}_u$ ,  $\mathbf{W}_w$ ,  $\mathbf{W}_g$ , and  $\mathbf{W}_T$ ), followed by the application of the divergence theorem. The weak forms are given as:

- Weak form of momentum balance equation:

$$\int_{\Omega} \nabla \mathbf{W}_u \left[ \frac{\partial \boldsymbol{\sigma}}{\partial t} \right] d\Omega = \int_{\Gamma_u^q} \mathbf{W}_u \left[ \frac{\partial \bar{\mathbf{t}}}{\partial t} \right] d\Gamma \quad (4.67)$$

- Weak form of mass balance equation for water species:

$$\begin{aligned}
& \int_{\Omega} \mathbf{W}_w \left[ nS_g \frac{\partial \rho_{gw}}{\partial t} + n\rho_{gw} \frac{\partial S_g}{\partial t} \right] d\Omega \\
& + \int_{\Omega} \mathbf{W}_w \left[ n\rho_w \frac{\partial S_w}{\partial t} + n\rho_i \frac{\partial S_i}{\partial t} - \beta_{swgi} \frac{\partial T}{\partial t} \right] d\Omega \\
& + \int_{\Omega} \mathbf{W}_w \left[ (S_w\rho_w + S_g\rho_{gw} + S_i\rho_i) \mathbf{m}^T \mathbf{L} \frac{\partial \mathbf{u}}{\partial t} \right] d\Omega \\
& + \int_{\Omega} \nabla \mathbf{W}_w \left[ \rho_g \frac{M_a M_w}{M_g^2} \mathbf{D}_{gw} \nabla \left( \frac{P_{gw}}{P_g} \right) \right] d\Omega \\
& + \int_{\Omega} \nabla \mathbf{W}_w \left[ \rho_w \frac{\mathbf{k}k_{rw}}{\mu_w} (\nabla P_w - \rho_w \mathbf{g}) \right] d\Omega \\
& + \int_{\Omega} \nabla \mathbf{W}_w \left[ \rho_{gw} \frac{\mathbf{k}k_{rg}}{\mu_g} (\nabla P_g - \rho_g \mathbf{g}) \right] d\Omega + \int_{\Gamma_w^q} \mathbf{W}_w [\bar{q}_w + \bar{q}_{gw}] d\Gamma \\
& = 0
\end{aligned} \tag{4.68}$$

- Weak form of mass balance equation for dry air:

$$\begin{aligned}
& \int_{\Omega} \mathbf{W}_g \left[ nS_g \frac{\partial \rho_{ga}}{\partial t} + n\rho_{ga} \frac{\partial S_g}{\partial t} \right] d\Omega + \int_{\Omega} \mathbf{W}_g \left[ S_g \rho_{ga} \mathbf{m}^T \mathbf{L} \frac{\partial \mathbf{u}}{\partial t} \right] d\Omega \\
& - \int_{\Omega} \mathbf{W}_g \left[ \beta_{sg} \frac{\partial T}{\partial t} \right] d\Omega - \int_{\Omega} \nabla \mathbf{W}_g \left[ \rho_g \frac{M_a M_w}{M_g^2} \mathbf{D}_{gw} \nabla \left( \frac{P_{gw}}{P_g} \right) \right] d\Omega \\
& + \int_{\Omega} \nabla \mathbf{W}_g \left[ \rho_{ga} \frac{\mathbf{k}k_{rg}}{\mu_g} (\nabla P_g - \rho_g \mathbf{g}) \right] d\Omega + \int_{\Gamma_g^q} \mathbf{W}_g [\bar{q}_{ga}] d\Gamma = 0
\end{aligned} \tag{4.69}$$

- Weak form of energy balance equation:

To address the advection-dominated problems in the energy balance equation (i.e., [Equation 4.36](#)), the Stream Upwind/Petrov Galerkin (SUPG) method is implemented to improve the accuracy and stability of simulations. It involves augmenting the weighting function, which determines the contribution of each term in the equation, with an appropriate term. This modification enables the accounting of advection effects. According to a previous model, we also utilize an arbitrary

weighting function, denoted as  $\mathbf{W}_T^*$ , which combines a continuous weighting function  $\mathbf{W}_T$  and a discontinuous streamline upwind correction term as stated in Equation 4.45 (Brooks and Hughes, 1982; Kelly et al., 1980):

$$\mathbf{W}_T^* = \mathbf{W}_T + \tau_e \mathbf{a} \cdot \nabla \mathbf{W}_T$$

with: (4.70)

$$\tau_e = \frac{h_e}{2\|\mathbf{a}\|} \left( \cot(p_e) - \frac{1}{p_e} \right)$$

here,  $\tau_e$  is an upwind parameter. It is derived based on the local Peclet number ( $p_e$ ) which is defined as:

$$p_e = \frac{\|\mathbf{a}\| h_e}{2\lambda_{\text{eff}}} \quad (4.71)$$

where  $h_e$  denotes the maximum length of the element of the mesh and  $\|\cdot\|$  is the Euclidean norm. By incorporating the computed arbitrary weighting function, the resulting weak form of the energy balance equation is expressed as:

$$\begin{aligned} & \int_{\Omega} \mathbf{W}_T^* \left[ (\rho C_p)_{\text{eff}} \frac{\partial T}{\partial t} \right] d\Omega + \int_{\Omega} \mathbf{W}_T^* \left[ (n S_w \rho_w C_p^w \mathbf{v}_{w,s} + n S_g \rho_g C_p^g \mathbf{v}_{g,s}) \cdot \nabla T \right] d\Omega \\ & + \int_{\Omega} \nabla \mathbf{W}_T^* [\lambda_{\text{eff}} \nabla T] d\Omega - \int_{\Omega} \mathbf{W}_T^* \left[ L_f \rho_i (1-n) S_i \mathbf{m}^T \mathbf{L} \frac{\partial \mathbf{u}}{\partial t} \right] d\Omega \\ & - \int_{\Omega} \mathbf{W}_T^* \left[ L_f \rho_i n \frac{\partial S_i}{\partial P_c} \frac{\partial P_g}{\partial t} \right] d\Omega + \int_{\Omega} \mathbf{W}_T^* \left[ L_f \rho_i n \frac{\partial S_i}{\partial P_c} \frac{\partial P_w}{\partial t} \right] d\Omega \\ & - \int_{\Omega} \mathbf{W}_T^* \left[ L_f \rho_i n \frac{\partial S_i}{\partial T} \frac{\partial T}{\partial t} \right] d\Omega + \int_{\Gamma_t^q} \mathbf{W}_T^* [\bar{q}_T] d\Gamma = 0 \end{aligned} \quad (4.72)$$

## 4.6 FEM implementation

### 4.6.1 Spatial discretization

In this paper, the Finite Element Method (FEM) is utilized for spatial discretization of the governing THM equations. This technique involves dividing the domain into smaller elements, and within each element, the solution is approximated using shape functions. By reformulating the THM governing equations into a weak form, the FEM transforms the original partial differential equations into a system of algebraic equations that can be solved numerically. Consequently, the FEM approximation of the displacement, strain, pressure, and temperature fields can be expressed as follows:

$$\begin{aligned}\mathbf{u}(\mathbf{x}, t) &= \mathbf{N}_u(\mathbf{x})\mathbf{U}(t) \\ \boldsymbol{\varepsilon}(\mathbf{x}, t) &= \mathbf{B}_u(\mathbf{x})\mathbf{U}(t) \\ P_\pi(\mathbf{x}, t) &= \mathbf{N}_p(\mathbf{x})\mathbf{P}_\pi(t) \quad (\pi = w, g) \\ T(\mathbf{x}, t) &= \mathbf{N}_t(\mathbf{x})\mathbf{T}(t)\end{aligned}\tag{4.73}$$

where,  $\mathbf{N}_u(\mathbf{x})$ ,  $\mathbf{N}_p(\mathbf{x})$ , and  $\mathbf{N}_t(\mathbf{x})$  are shape functions of fields of displacement, fluid pressure, and temperature, respectively.  $\mathbf{B}_u(\mathbf{x})$  is the spatial derivative of shape function, and  $\mathbf{U}(t)$ ,  $\mathbf{P}_\pi(t)$ , and  $\mathbf{T}(t)$  are the nodal values of displacement, fluid pressure and temperature fields, respectively. To enhance the numerical stability and accuracy of the results, linear test functions were utilized to discretize the water pressure and temperature, while second-order shape functions were employed to discretize the displacement in this THM-coupled analysis. This improves the accuracy in representing the displacement field compared to linear shape functions (Lewis and Schrefler, 1998; Zienkiewicz and Shiomi, 1984). Finally, the set of discretized coupled governing equations end up to an ordinary time-dependent differential equation system stated as:

$$\begin{bmatrix} 0 & 0 & 0 & 0 \\ 0 & \mathbf{K}_{ww} & \mathbf{K}_{wg} & \mathbf{K}_{wt} \\ 0 & \mathbf{K}_{gw} & \mathbf{K}_{gg} & \mathbf{K}_{gt} \\ 0 & 0 & 0 & \mathbf{K}_{tt} \end{bmatrix} \begin{Bmatrix} \mathbf{u} \\ \mathbf{P}_w \\ \mathbf{P}_g \\ \mathbf{T} \end{Bmatrix} + \begin{bmatrix} \mathbf{C}_{uu} & \mathbf{C}_{uw} & \mathbf{C}_{ug} & \mathbf{C}_{ut} \\ \mathbf{C}_{wu} & \mathbf{C}_{ww} & \mathbf{C}_{wg} & \mathbf{C}_{wt} \\ \mathbf{C}_{gu} & \mathbf{C}_{gw} & \mathbf{C}_{gg} & \mathbf{C}_{gt} \\ \mathbf{C}_{tu} & \mathbf{C}_{tw} & \mathbf{C}_{tg} & \mathbf{C}_{tt} \end{bmatrix} \frac{d}{dt} \begin{Bmatrix} \mathbf{u} \\ \mathbf{P}_w \\ \mathbf{P}_g \\ \mathbf{T} \end{Bmatrix} = \begin{Bmatrix} \mathbf{f}_u \\ \mathbf{f}_w \\ \mathbf{f}_g \\ \mathbf{f}_t \end{Bmatrix} \quad (4.74)$$

All the matrix elements are presented in Appendix B.

#### 4.6.2 Temporal discretization

Assuming  $\mathbf{X}^T = [\mathbf{u} \ \mathbf{P}_w \ \mathbf{P}_g \ \mathbf{T}]$  as the vector of unknown variables, Equation 4.49 can be rewritten as the following compact form:

$$\mathbf{K}\mathbf{X} + \mathbf{C} \frac{d\mathbf{X}}{dt} = \mathbf{F} \quad (4.75)$$

To solve the above equation, the fully implicit Finite Difference Method is utilized herein. After time integration of the nonlinear set of ordinary differential equations over the time domain, the form of the discretized residual vector at time  $t_{n+1}$  is derived based on backward Euler algorithm as follows:

$$\mathbf{R}_{n+1} = \mathbf{C}_{n+1} \frac{\mathbf{X}_{n+1} - \mathbf{X}_n}{\Delta t} + \mathbf{K}_{n+1} \mathbf{X}_{n+1} - \mathbf{F}_{n+1} \quad (4.76)$$

where  $\Delta t$  is the time interval. To solve fully coupled nonlinear system of Equation 4.51, the unknown increments should be computed using a Newton-Raphson iteration scheme:

$$\mathbf{R}_{n+1}^{i+1} = \mathbf{R}_{n+1}^i + \mathbf{J} d\mathbf{X}_{n+1}^{i+1} = 0 \quad (4.77)$$

$$d\mathbf{X}_{n+1}^{i+1} = -\frac{\mathbf{R}_{n+1}^i}{\mathbf{J}} \quad (4.78)$$

where  $\mathbf{R}_{n+1}^i$  is the result of subtracting the total force ( $\mathbf{F}_{n+1}$ ) and the vector of converged solution from the previous time step of analysis ( $\mathbf{P}_n$ ) from the internal force:

$$\mathbf{R}_{n+1}^i = \mathbf{J}\mathbf{X}_{n+1}^i - \mathbf{F}_{n+1}^i - \mathbf{P}_n \quad (4.79)$$

$$\mathbf{P}_n = \frac{\mathbf{C}_{n+1}^i \mathbf{X}_n}{\Delta t} \quad (4.80)$$

Subsequently, the Jacobian matrix ( $\mathbf{J}$ ) in Equation 4.52 can be derived by differentiating the residual with respect to the unknown variables vector ( $\mathbf{X}$ ):

$$\mathbf{J} = \begin{bmatrix} \frac{\mathbf{C}_{uu}}{\Delta t} & \frac{\mathbf{C}_{uw}}{\Delta t} & \frac{\mathbf{C}_{ug}}{\Delta t} & \frac{\mathbf{C}_{ut}}{\Delta t} \\ \frac{\mathbf{C}_{wu}}{\Delta t} & \frac{\mathbf{C}_{ww}}{\Delta t} + \mathbf{K}_{ww} & \frac{\mathbf{C}_{wg}}{\Delta t} + \mathbf{K}_{wg} & \frac{\mathbf{C}_{wt}}{\Delta t} + \mathbf{K}_{wt} \\ \frac{\mathbf{C}_{gu}}{\Delta t} & \frac{\mathbf{C}_{gw}}{\Delta t} + \mathbf{K}_{gw} & \frac{\mathbf{C}_{gg}}{\Delta t} + \mathbf{K}_{gg} & \frac{\mathbf{C}_{gt}}{\Delta t} + \mathbf{K}_{gt} \\ \frac{\mathbf{C}_{tu}}{\Delta t} & \frac{\mathbf{C}_{tw}}{\Delta t} & \frac{\mathbf{C}_{tg}}{\Delta t} & \frac{\mathbf{C}_{tt}}{\Delta t} + \mathbf{K}_{tt} \end{bmatrix} \quad (4.81)$$

Finally, the unknown vector is updated at each iteration until the required convergence criterion is satisfied:

$$\mathbf{X}_{n+1}^{i+1} = \mathbf{X}_{n+1}^i + d\mathbf{X}_{n+1}^{i+1} \quad (4.82)$$

By defining  $\varepsilon = 10^{-5}$  as the prescribed tolerance, the convergence criterion of iteration is set as:

$$|\mathbf{R}_{n+1}^i| < \varepsilon \quad (4.83)$$

The algorithm for solving nonlinear FEM numerical models for the present THM coupled processes is summarized in **Box 4-1**. In our formulation, the material plastic nonlinear behavior is treated using the implicit return mapping algorithm. However, the thermally induced plastic yielding (hardening or softening) is considered explicitly, which is similar to the approach presented by [Semnani et al., \(2016\)](#).

- 1) Start
- 2) Start time step  $n+1$
- 3) Assemble  $\mathbf{C}_n$ ,  $\mathbf{K}_n$ , and Jacobian matrix, using variables in step  $n$
- 4) Calculate external forces and residual
- 5) Impose boundary conditions
- 6) Start while loop
  - a) Start a new iteration
  - b) Compute  $d\mathbf{X}_{n+1}^{i+1}$
  - c) Calculate effective strain, trial volumetric and deviatoric stresses
  - d) Update temperature-dependent mechanical properties (i.e.,  $E$ ,  $\nu$ ,  $c$ , and  $\phi$ ) based on updated temperature
  - e) Check for plasticity
    - i) If plasticity trues:
      - update plastic strain, volumetric and deviatoric stresses using return mapping algorithm and find tangential stiffness matrix
    - ii) Else,
      - keep the elastic and thermal-hydraulic parameters and use elastic stiffness matrix.
  - f) Update thermal, hydraulic variables for THM coupling
  - g) Assemble  $\mathbf{C}_{n+1}^i$ ,  $\mathbf{K}_{n+1}^i$  and Jacobian matrix using updated variables
  - h) Find internal force and update the external force to find new residual
    - i) If the residual meets the convergence criterion,
      - end while loop and go to (7)
    - ii) Else,
      - go to the next iteration
- 7) Save primary and secondary variables for the next step.
- 8) Go to the next step

Box 4-1 Numerical algorithm for solving the nonlinear THM coupled FEM problem.

## 4.7 Numerical verification

Based on the above-mentioned formulations and algorithm, we implement the new THM model through our in-house developed FEM code using MATLAB. The thermal-poroelastic part of the code was validated previously (Norouzi et al., 2019). In order to validate the performance of simulating frost actions in unsaturated soils, we use the 1D freezing test data on an unsaturated soil conducted by Bai et al., (2020). In their experiment, an unsaturated silty soil sample is

subjected to an initial temperature profile of 3°C. A constant temperature of -3°C is applied to the top side for 100 hours, while the bottom temperature is kept constant at 3°C. Before frozen, the initial water saturation of the studied soil is 49%. During the test, data of total water content, temperature, and frost heave is recorded.

We carry out a 2D FEM modeling on the above-mentioned laboratory freezing test. In the simulation, a sample with the dimension of 50 mm × 90 mm is modeled as a plane strain problem. The size of elements is 5 mm × 5 mm and each element contains four Gauss points. Figure 4-3 shows the finite element mesh for the simulation. We have carried out a mesh sensitivity analysis to make sure the applied mesh size generates a stable result.

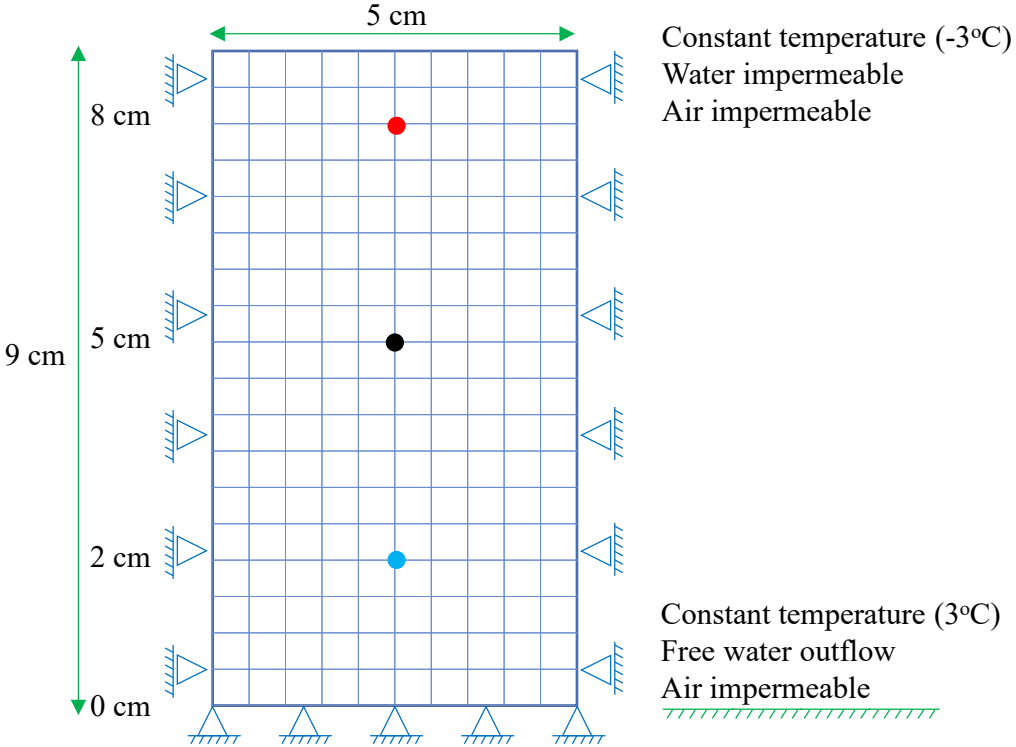


Figure 4-3 FEM mesh and boundary conditions of both ends for the numerical test.

The displacement of the bottom side is restricted in both directions and the lateral side is restricted in the horizontal direction. Additionally, the lateral sides are adiabatic with no hydraulic flux and all sides are impermeable. The problem is solved for a total time of 100 hours.

According to Bai et al., (2020), the temperature-dependent mechanical properties of the soil are given as:

$$E = \begin{cases} 20 + 11.3(T_f - T)^{0.6} & T \leq T_f \\ 20 & T > T_f \end{cases} \quad (4.84)$$

$$\nu = \begin{cases} 0.28 - 0.007(T_f - T) & T \leq T_f \\ 0.28 & T > T_f \end{cases} \quad (4.85)$$

$$c = \begin{cases} 20 + 6(T_f - T)^{1.24} & T \leq T_f \\ 20 & T > T_f \end{cases} \quad (4.86)$$

$$\phi = \begin{cases} 20 + 3.4(T_f - T)^{0.38} & T \leq T_f \\ 20 & T > T_f \end{cases} \quad (4.87)$$

In the above equations, the units of Young's modulus ( $E$ ), cohesive ( $c$ ), and friction angle ( $\phi$ ) are MPa, kPa, and degree, respectively. The rest of the material properties or parameters applied in the numerical model are presented in Table 4-1.

Table 4-1 Material properties for the unsaturated soil in the 1D freezing (Bai et al., 2020)

Initial porosity	$n = 0.47$ (-)
Density of solid	$\rho_s = 2700$ (kg/m <sup>3</sup> )
Density of ice	$\rho_i = 910$ (kg/m <sup>3</sup> )
Density of water	$\rho_w = 1000$ (kg/m <sup>3</sup> )
Universal gas constant	$R = 8.31$ (J/mole)
Molar mass of dry air	$M_a = 28.97$ (g/mole)
Molar mass of liquid water	$M_w = 18.02$ (g/mole)
Intrinsic permeability	$\mathbf{k} = 8 \times 10^{-13}$ (m <sup>2</sup> )
Dynamic viscosity of water	$\mu_w = 1 \times 10^{-3}$ (Pa.s)
Dynamic viscosity of air	$\mu_g = 1 \times 10^{-5}$ (Pa.s)
Van Genuchten's model parameter	$\alpha_v = 1.89 \times 10^{-4}$ (Pa <sup>-1</sup> )
Van Genuchten's model parameter	$n_v = 1.25$ (-)
Van Genuchten's model parameter	$m_v = 0.28$ (-)
Empirical constant of impedance factor of ice	$E_v = 10$
Ratio of ice-liquid to liquid-air surface	$\beta = 2.2$ (-)
Specific heat capacity of soil	$C_s = 880$ (J/kg/K)

Specific heat capacity of ice	$C_i = 1874 \text{ (J/kg/K)}$
Specific heat capacity of water	$C_w = 4180 \text{ (J/kg/K)}$
Specific heat capacity of air	$C_g = 717 \text{ (J/kg/K)}$
Thermal conductivity of soil	$\lambda_s = 1.2 \text{ (W/m/K)}$
Thermal conductivity of ice	$\lambda_i = 2.22 \text{ (W/m/K)}$
Thermal conductivity of water	$\lambda_w = 0.58 \text{ (W/m/K)}$
Thermal conductivity of air	$\lambda_g = 0.03 \text{ (W/m/K)}$
Thermal expansion coefficient of solid	$\beta_s = 9 \times 10^{-7} \text{ (1/K)}$
Thermal expansion coefficient of ice	$\beta_i = 5 \times 10^{-7} \text{ (1/K)}$
Thermal expansion coefficient of water	$\beta_w = 6.3 \times 10^{-6} \text{ (1/K)}$
Latent heat of fusion	$L_f = 3.45 \times 10^5 \text{ (J/kg)}$
Reference temperature	$T_0 = 273.15 \text{ (K)}$

Simulated temperature variations at different heights are obtained and displayed in [Figure 4-4](#) along with the measured data. In general, the simulation results are aligned with the experimental data.

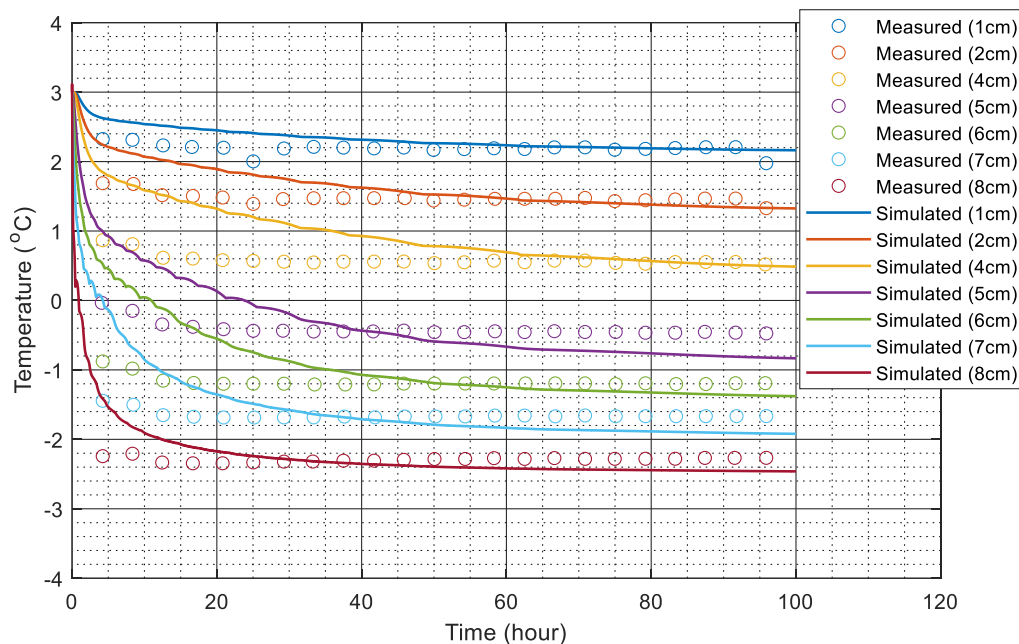


Figure 4-4 Simulated temperature evolutions at different heights (measured data is from [Bai et al., \(2020\)](#))

[Figure 4-5](#) presents a simulated the total volumetric water content (ice and liquid water) profile at  $t = 100$  hours along with experimental data by [Bai et al., \(2020\)](#). The water redistribution due to frost action can be well characterized except at the ice-water interface. A more detailed description

of the water content development during freezing is illustrated in contour plots displayed in Figure 4-6.

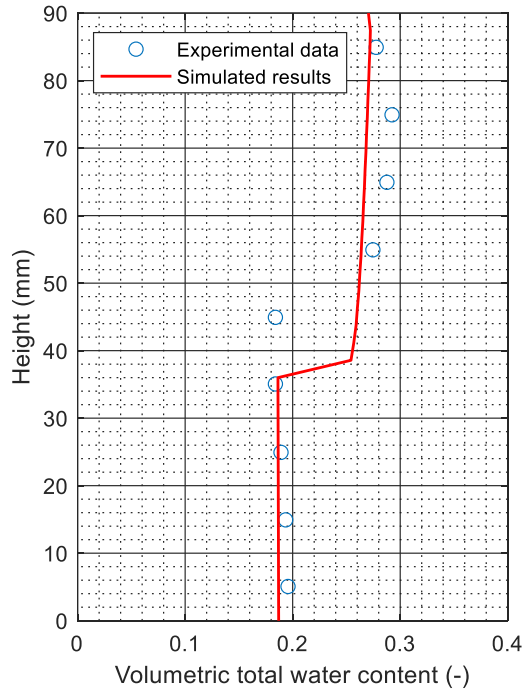


Figure 4-5 Simulated and measured total volumetric water contents at the end of the test ( $t = 100$  hrs) (measured data is from Bai et al., (2020)).

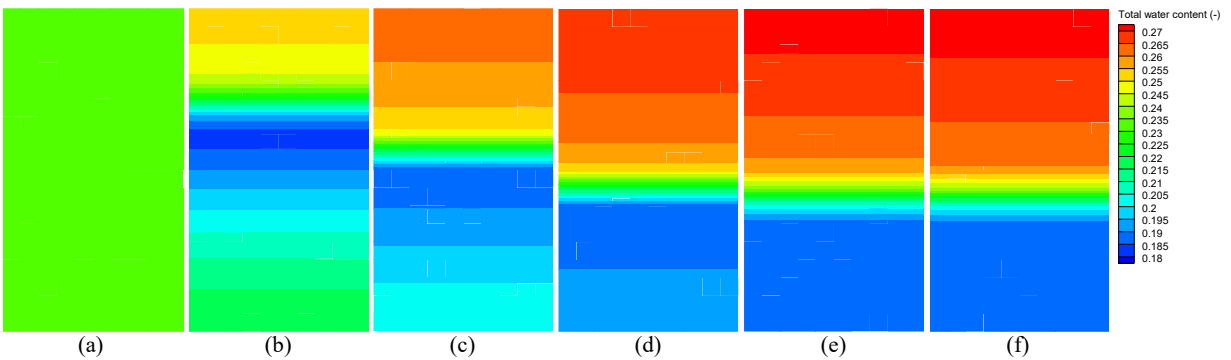


Figure 4-6 Simulated contours of total volumetric water contents at: (a) initial condition, (b)  $t = 10$  hrs, (c)  $t = 25$  hrs, (d)  $t = 50$  hrs, (e)  $t = 75$  hrs, and (f)  $t = 100$  hrs.

As is displayed in Figure 4-7, the variation in total water content during freezing is mainly driven by the increase in the ice content. Water from the lower portion moves to the upper side due to the cryosuction. Even though the soil is unsaturated, such a change in water re-distribution still can lead to a significant heaving in the soil sample. Figure 4-8 presents the simulated frost heave result against the measured result by Bai et al., (2020), which indicates a comparable agreement. The results of considering phase change induced strain will be discussed in the subsequent section.

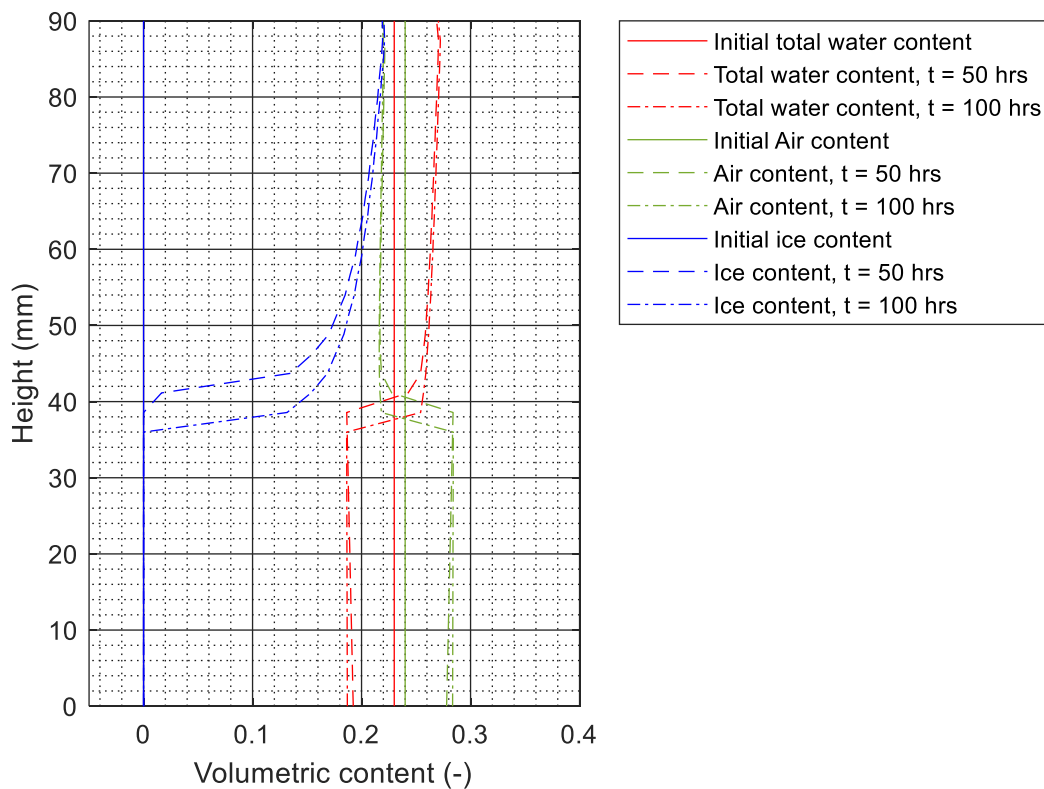


Figure 4-7 Plots showing the profile developments of total water content, air content, and ice content.

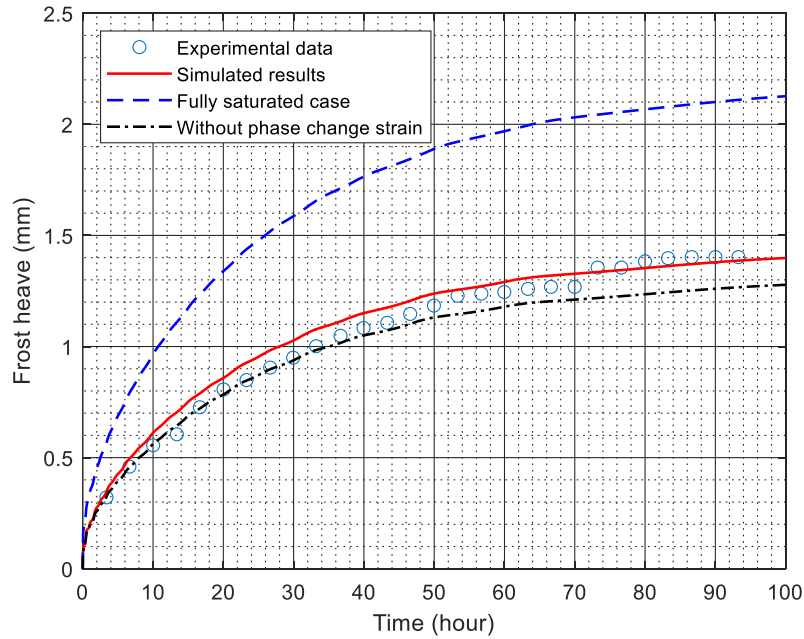


Figure 4-8 Simulated and measured frost heave developments with time (measured data is from Bai et al., (2020)).

## 4.8 Discussions

### 4.8.1 Effect of phase change strain

In this study, the phase change strain for an unsaturated soil is calculated using a coefficient  $\beta_{ph}$  to accommodate the water saturation state as is shown Equation 4.27. For simplicity, we have assigned the initial water saturation value to  $\beta_{ph}$ . In order to examine the sensitivity of using different  $\beta_{ph}$  values, we also carry out some numerical tests using different  $\beta_{ph}$  values while keeping other materials properties and boundary conditions the same as described in Section 6. The results of frost heave curves are also included in Figure 4-8. The case with  $\beta_{ph} = 1$  represents a fully saturated condition, while  $\beta_{ph} = 0$  represents a case without considering phase change induced strain. Significant differences are noticed in the three curves displayed in Figure 4-8. The results indicate that assuming a fully saturated condition will overestimate the frost heave, while the neglect of phase change strain underestimates the frost heave. The adoption of the initial water

saturation value for  $\beta_{ph}$  yields a reasonable frost heave prediction. The difference in the deformation behavior can also be demonstrated by the difference in porosity profiles. Simulated porosity contours (at  $t = 100$  hrs) for cases with and without considering phase change strain are presented in Figure 4-9. The porosity change is updated according to the change in the volumetric strain using the equation of  $\Delta n = (1 - n)\Delta\epsilon_v$ . The major difference is located in the upper part, where the ice tends to be accumulated. The case by considering phase change strain displays a larger amount of increment in porosity when compared with the case without phase change strain. However, it should be noted that the freezing driven water movement from the warm side to the cold side has contributed to a significant amount of porosity increase. Thus, the porosity increase in the upper part of sample is still obvious even if the phase change induced volumetric strain is not accounted (Figure 4-9b). It also confirms with the possibility of having frost heave in an unsaturated soil.

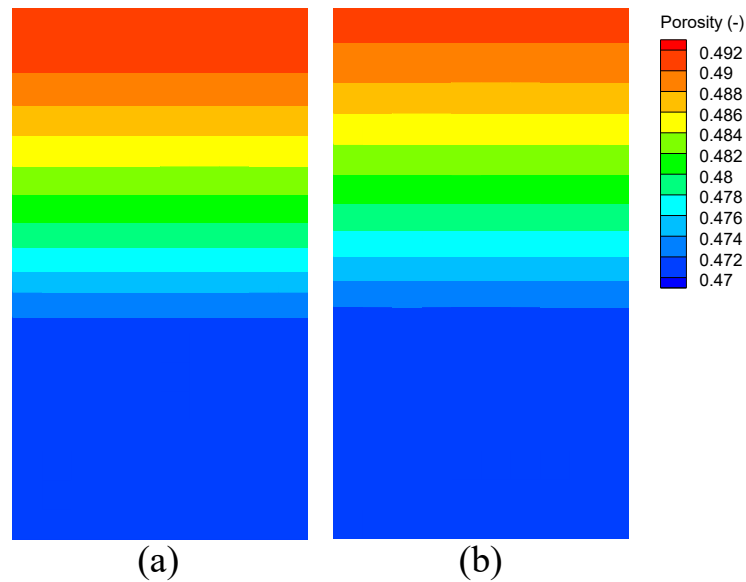


Figure 4-9 Simulated porosity contours at the end of numerical tests: (a) with phase change strain, (b) without phase change strain ( $t = 100$  hrs).

## 4.8.2 Pore pressure variations

As an investigation of the poromechanical response, the characterization of the pore pressure is essential. In this study, we applied the equivalent pore pressure concept as:

$$P_{\text{pore}} = S_w P_w + S_g P_g + S_i P_i \quad (4.88)$$

The liquid water pressure  $P_w$ , air pressure  $P_g$ , and ice pressure  $P_i$  are treated as parts of the total pore pressure  $P_{\text{pore}}$ . The saturations of individual components are used as simplified weight coefficients. Such application is valid when there is a pore water pressure balance between macropores and micropores. More detailed microstructure-based derivation for the equivalent pore pressure for unsaturated porous media is presented by [Yin et al., \(2023\)](#). The simulated total pore pressure changes during the numerical test are obtained and displayed in [Figure 4-10a](#). The curves show the variations along the height profile at different times, but the total pore pressure has always been positive.

In this study, both vapor and dry air are included in the gas phase. Thus, we can quantify the contributions from vapor and dry air according to the simulation results. Simulated vapor pressure and dry air pressure profiles are obtained and displayed in [Figures 4-10b](#) and [4-10c](#). The vapor pressure varies significantly along the height, but the range of vapor pressure changes with time is only around 2 kPa. By contrast, the dry air pressure is uniformly distributed but increases considerably with time. Thus, dry air contributes more effectively to an increase in the air pressure during freezing. As is displayed in [Figure 4-10d](#), the freezing point temperature values are slightly affected by the change in pore pressure. The variation of freezing point temperature profiles is similar to that of pore pressure profiles.

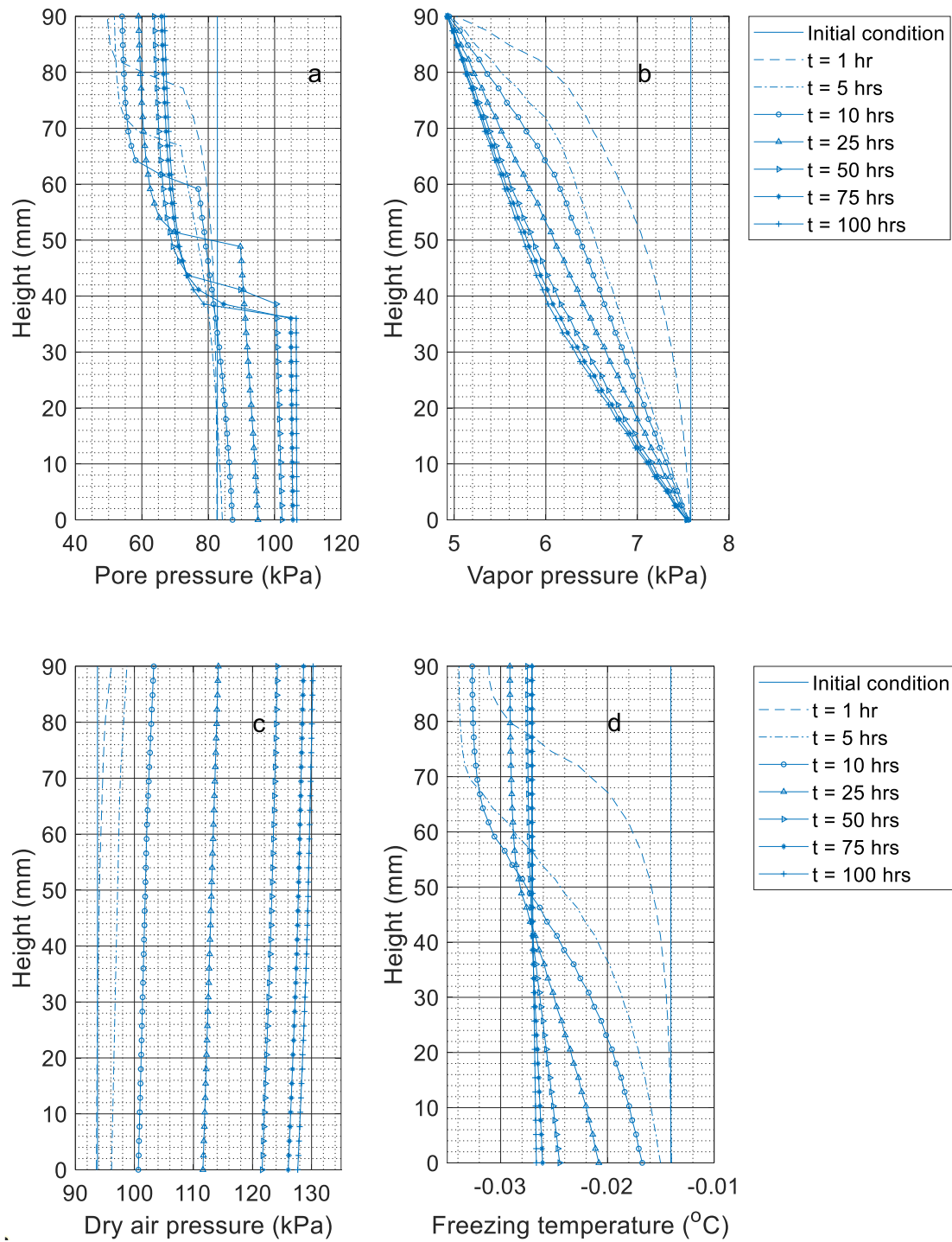


Figure 4-10 Simulated pore pressure and freezing temperature point profiles at different times of the numerical test: (a) total pore pressure, (b) vapor pressure, (c) dry air pressure, (d) freezing temperature point.

In order to better demonstrate the pore pressure fluctuation, we present the simulated pore pressure development at three key monitoring points (height = 2 cm, 5 cm, and 8 cm) in Figure 4-11. The freezing induced pore pressure drop in the top part of the sample can be well reflected by the curve of the point at 8 cm. By contrast, the lower part of the sample (height = 2 cm) is subjected to a gradual increase in pore pressure.

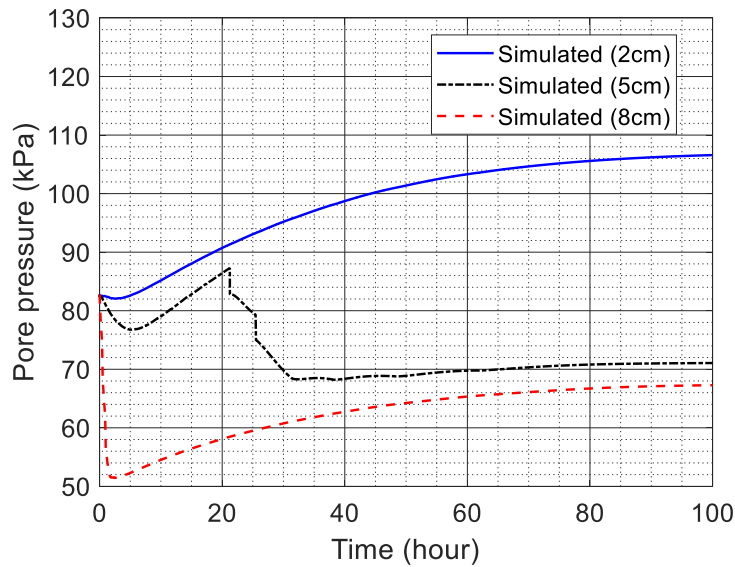


Figure 4-11 Simulated pore pressure development at three key monitoring points (height = 2 cm, 5 cm, and 8 cm).

### 4.8.3 Freezing induced plastic strain

In the study by Bai et al., (2020), temperature-dependent mechanical properties of the related soil sample were provided. However, the potential thermally induced plastic behavior was not characterized experimentally or numerically in the previous study. As is presented in Box 1, the thermally induced plastic yielding process can be quantified using our in-house developed FEM numerical tool. From our numerical results, we can notice the simulated accumulated plastic strain (von Mises equivalent plastic strain) during the freezing process (Figure 4-12). The generated plastic strain is generally located in the upper part of the sample, which is close to the freezing

end. Simulated stress paths in the mean effective stress-Mises equivalent shear stress space ( $p' - q$  space) of three monitoring points (height = 2 cm, 5 cm, and 8 cm) are also collected and displayed in Figure 4-13a. The curves indicate that some shear stress is built up during the freezing process. Some tensile stress tends to be generated in the upper part of the sample during the early stage of freezing. As is shown in Figure 4-13b, the generated plastic strain is mostly developed in the first 50 hours.

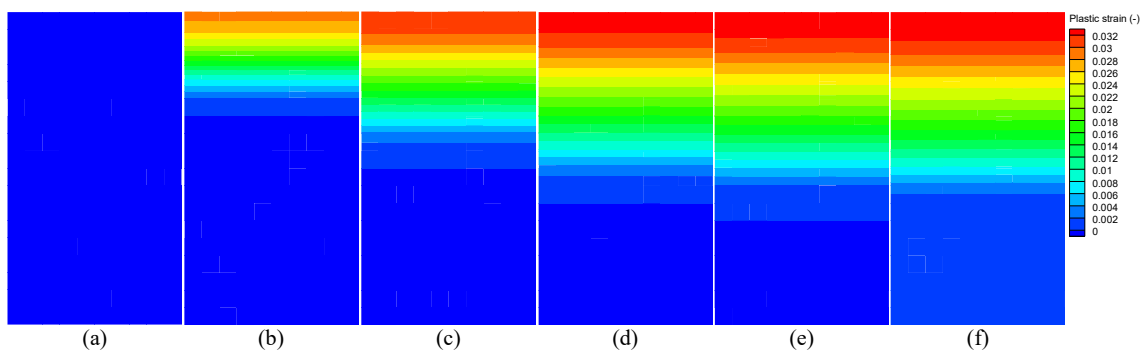


Figure 4-12 Simulated von Mises equivalent plastic strain contours at: (a) initial condition, (b)  $t = 10$  hrs, (c)  $t = 25$  hrs, (d)  $t = 50$  hrs, (e)  $t = 75$  hrs, and (f)  $t = 100$  hrs.

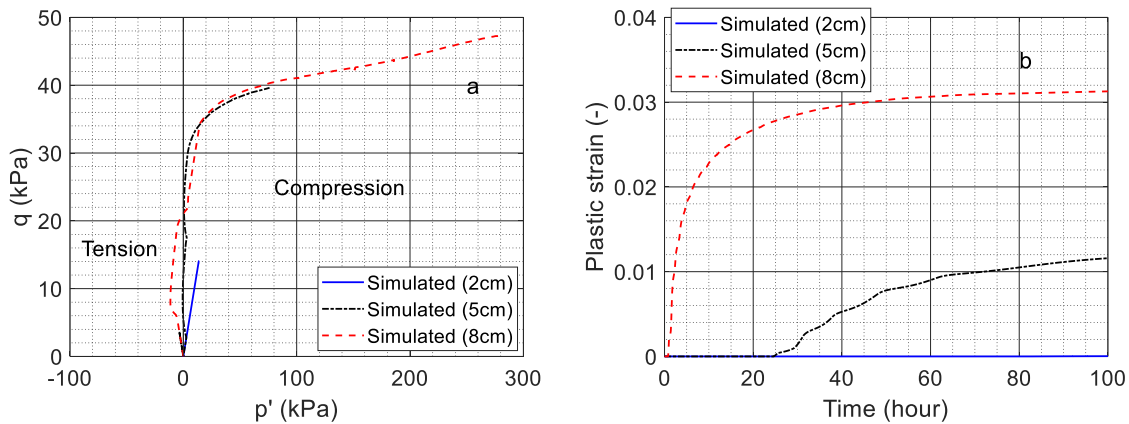


Figure 4-13 Simulated effective stress paths and accumulated plastic strains at the three key points.

#### 4.8.4 Limitations

While the proposed computational model demonstrates a good range of applicability, this research has its limitations that offer opportunities for future investigations. Several aspects can be further explored to enhance the model's accuracy and applicability. Instead of relying on ideal gas relations, future studies may consider employing more realistic gas relations to better capture the behavior of vapor and dry air during the freezing process. This could lead to more accurate predictions of vapor pressure changes and their influence on the overall system. The present THM-coupled FEM formulation is capable of simulating related plastic yielding behavior due to frost actions. However, the present numerical model is not yet validated against any experimental data with an apparent record of plastic response. Our simulation generates some preliminary numerical results on potential freezing induced plastic deformation behavior, and the frozen soil is treated as a continuum porous media using a phenomenon based plastic model. The pore-scale yielding or failure process of frozen soil cannot be simulated using our numerical tool. Further theoretical development of the micromechanical failure process in frozen soil due to ice generation is recommended. The interfacial aspect between frozen and unfrozen parts should be investigated to simulate the ice lens generation process. A possible approach is to apply the eXtended Finite Element Method (XFEM) to characterize the imperfect interfacial bond or cracking behaviors in frozen soil (Khoei and Mortazavi, 2020; Emad Norouzi et al., 2022). In addition, exploring a broader range of soil types and environmental factors would provide insights into the model's performance and limitations in different scenarios. Further numerical and experimental investigations on the hardening/softening of unsaturated frozen soils due to freeze-thaw actions are recommended.

## 4.9 Conclusions

In this study, we present a comprehensive and inclusive finite element formulation for describing the thermal-hydro-mechanical coupled processes in unsaturated freezing soils considering pore pressure components from liquid water, air, and ice. The model is successfully applied to a 1D freezing test on an unsaturated soil to demonstrate its capability to characterize the variations in total water content, temperature, and frost heave. Several conclusions are drawn as follows:

- The new THM-coupled model is developed based on the fundamentals of continuum mechanics. The weak forms of equations of the linear momentum balance equation, mass balance equations of dry air and water species, and energy balance equation are developed and presented in detail. To address the advection-dominated problems in the energy balance equation, the SUPG method can be implemented to improve the accuracy and stability of simulations. The traditional van Genuchten soil water characteristic (SWC) curve model and the Clapeyron equation can be combined to generate a new soil freezing characteristic curve (SFCC) model to consider the suctions from air-water capillary pressure and water-ice cryosuction. The new SFCC model can be well implemented in the FEM formulation with the consideration of capillary pressure-dependent ice saturation.
- The phase change induced strain should be properly considered in the numerical modeling of frost actions in unsaturated soils. Our numerical tests indicate that assuming a fully saturated condition will overestimate the frost heave, while the neglect of phase change strain underestimates the heaving result. An adjustment coefficient with an initial water saturation value can be applied to accommodate the water saturation state.

A total pore pressure as a function of air pressure, water pressure, ice pressure, and their corresponding saturations is used in the effective stress law. When freezing starts, the pore pressure

increases in the freezing zone due to an increase in ice pressure and reduces in the unfrozen zone because of the air movement. During freezing, there is a slight drop in the vapor pressure but a significant increase in dry air pressure. Thus, the increase in the air pressure during freezing is mainly contributed by the dry air. By considering air pressure, water pressure and ice pressure as components of the total pore pressure, our numerical tool can characterize the development of effective stress paths and the potential thermally induced plastic yielding behavior.

## Appendix A: Notation list of symbols

$s$	Solid phase
$w$	Water phase
$i$	Ice phase
$g$	Moist air phase
$ga$	Dry air phase
$gw$	Vapor phase
$V_\alpha$	Volume of each phase
$\theta_\alpha$	Volumetric content of each phase
$n$	Porosity
$S_\alpha$	Saturation
$\rho_\alpha$	Density
$P_w$	Water pressure
$P_{wf}$	Water pressure in frozen soil
$P_i$	Ice pressure
$P_g$	Air pressure
$P_{ga}$	Dry air pressure
$P_{gw}$	Vapor air pressure
$P_{gws}$	Saturated vapor pressure
$P_c$	Capillary pressure of water and air
$P_{cf}$	Capillary pressure of water and ice
$\mathbf{k}$	Intrinsic permeability
$k_{r\alpha}$	Relative permeability
$\mu_\alpha$	Viscosity
$\alpha_v$	Van Genuchten's model parameter
$n_v$	Van Genuchten's model parameter
$m_v$	Van Genuchten's model parameter
$\Omega_v$	Impedance factor of ice
$M_w$	Molar mass of liquid water
$M_a$	Molar mass of dry air
$M_g$	Molar mass of moist air
$h_r$	Relative humidity
$T$	Temperature
$T_0$	Reference temperature
$T_f$	Freezing point temperature
$L_f$	Latent heat of fusion
$L_w$	Latent heat of vapor condensation
$\sigma$	Total stress
$\sigma'$	Effective stress
$\mathbf{b}$	Body force
$\mathbf{u}$	Displacement
$\mathbf{D}_T$	Tangential stiffness matrix
$\boldsymbol{\varepsilon}$	Total strain

$\boldsymbol{\varepsilon}^{\text{ph}}$  Phase change strain  
 $\boldsymbol{\varepsilon}^T$  Thermal strain  
 $C_p^\alpha$  Heat capacity  
 $\lambda_\alpha$  Heat conductivity

## Appendix B: The Matrix form of governing equations

- Momentum balance equation

$$\mathbf{C}_{uu} = \int_{\Omega} \mathbf{B}_u^T \mathbf{D}_T \mathbf{B}_u d\Omega$$

$$\begin{aligned} \mathbf{C}_{uw} = & - \int_{\Omega} \mathbf{B}_u^T S_w \mathbf{mN}_p d\Omega + \int_{\Omega} \mathbf{B}_u^T \left[ \frac{\partial S_w}{\partial P_c} P_w + \frac{\partial S_g}{\partial P_c} P_g + \frac{\partial S_i}{\partial P_c} P_i - S_i \right] \mathbf{mN}_p d\Omega \\ & + \int_{\Omega} \mathbf{B}_u^T \mathbf{D}_T \frac{\beta_{ph}}{3} \left( \frac{n(\rho_w - \rho_i)}{\rho_w S_w + \rho_i S_i} \right) \frac{\partial S_i}{\partial P_c} \mathbf{mN}_p d\Omega \end{aligned}$$

$$\begin{aligned} \mathbf{C}_{ug} = & - \int_{\Omega} \mathbf{B}_u^T S_g \mathbf{mN}_p d\Omega - \int_{\Omega} \mathbf{B}_u^T \left[ \frac{\partial S_w}{\partial P_c} P_w + \frac{\partial S_g}{\partial P_c} P_g + \frac{\partial S_i}{\partial P_c} P_i \right] \mathbf{mN}_p d\Omega \\ & - \int_{\Omega} \mathbf{B}_u^T \mathbf{D}_T \frac{\beta_{ph}}{3} \left( \frac{n(\rho_w - \rho_i)}{\rho_w S_w + \rho_i S_i} \right) \frac{\partial S_i}{\partial P_c} \mathbf{mN}_p d\Omega \end{aligned}$$

$$\begin{aligned} \mathbf{C}_{ut} = & - \int_{\Omega} \mathbf{B}_u^T \left[ \frac{\partial S_w}{\partial T} P_w + \frac{\partial S_g}{\partial T} P_g + \frac{\partial S_i}{\partial T} P_i - \frac{S_i \rho_w L_f}{T_0} \right] \mathbf{mN}_t d\Omega - \int_{\Omega} \mathbf{B}_u^T \mathbf{D}_T \frac{\beta_s}{3} \mathbf{mN}_t d\Omega \\ & - \int_{\Omega} \mathbf{B}_u^T \mathbf{D}_T \frac{\beta_{ph}}{3} \left( \frac{n(\rho_w - \rho_i)}{\rho_w S_w + \rho_i S_i} \right) \frac{\partial S_i}{\partial T} \mathbf{mN}_t d\Omega \end{aligned}$$

$$\mathbf{f}_u = \int_{\Gamma_u^q} \mathbf{N}_u^T \frac{\partial \bar{\mathbf{t}}}{\partial t} d\Gamma$$

- Mass balance equation of water species

$$\mathbf{C}_{wu} = \int_{\Omega} \mathbf{N}_p^T [S_w \rho_w + S_g \rho_{gw} + S_i \rho_i] \mathbf{m}^T \mathbf{B}_u d\Omega$$

$$\mathbf{C}_{ww} = - \int_{\Omega} \mathbf{N}_p^T n S_g \frac{M_w}{RT} \frac{\partial P_{gw}}{\partial P_c} \mathbf{N}_p d\Omega - \int_{\Omega} \mathbf{N}_p^T \left[ n \rho_{gw} \frac{\partial S_g}{\partial P_c} + n \rho_w \frac{\partial S_w}{\partial P_c} + n \rho_i \frac{\partial S_i}{\partial P_c} \right] \mathbf{N}_p d\Omega$$

$$\mathbf{C}_{wg} = \int_{\Omega} \mathbf{N}_p^T n S_g \frac{M_w}{RT} \frac{\partial P_{gw}}{\partial P_c} \mathbf{N}_p d\Omega + \int_{\Omega} \mathbf{N}_p^T \left[ n \rho_{gw} \frac{\partial S_g}{\partial P_c} + n \rho_w \frac{\partial S_w}{\partial P_c} + n \rho_i \frac{\partial S_i}{\partial P_c} \right] \mathbf{N}_p d\Omega$$

$$\begin{aligned} \mathbf{C}_{wt} = & \int_{\Omega} \mathbf{N}_p^T \left[ n S_g \frac{M_w}{RT} \left( \frac{\partial P_{gw}}{\partial T} - \frac{P_{gw}}{T} \right) \right] \mathbf{N}_t d\Omega \\ & + \int_{\Omega} \mathbf{N}_p^T \left[ n \rho_{gw} \frac{\partial S_g}{\partial T} + n \rho_w \frac{\partial S_w}{\partial T} + n \rho_i \frac{\partial S_i}{\partial T} \right] \mathbf{N}_t d\Omega - \int_{\Omega} \mathbf{N}_p^T \beta_{swgi} \mathbf{N}_t d\Omega \end{aligned}$$

$$\mathbf{K}_{ww} = \int_{\Omega} (\nabla \mathbf{N}_p)^T \left[ -\rho_g \frac{M_a M_w}{M_g^2} \mathbf{D}_{gw} \frac{1}{P_g} \frac{\partial P_{gw}}{\partial P_c} + \rho_w \frac{\mathbf{k}k_{rw}}{\mu_w} \right] \nabla \mathbf{N}_p d\Omega$$

$$\begin{aligned} \mathbf{K}_{wg} = & \int_{\Omega} (\nabla \mathbf{N}_p)^T \left[ \rho_g \frac{M_a M_w}{M_g^2} \mathbf{D}_{gw} \frac{1}{P_g} \frac{\partial P_{gw}}{\partial P_c} + \rho_{gw} \frac{\mathbf{k}k_{rg}}{\mu_g} \right] \nabla \mathbf{N}_p d\Omega \\ & - \int_{\Omega} (\nabla \mathbf{N}_p)^T \rho_g \frac{M_a M_w}{M_g^2} \mathbf{D}_{gw} \frac{P_{gw}}{(P_g)^2} \nabla \mathbf{N}_p d\Omega \end{aligned}$$

$$\mathbf{K}_{wt} = \int_{\Omega} (\nabla \mathbf{N}_p)^T \rho_g \frac{M_a M_w}{M_g^2} \mathbf{D}_{gw} \frac{1}{P_g} \frac{\partial P_{gw}}{\partial T} \nabla \mathbf{N}_t d\Omega$$

$$\mathbf{f}_w = \int_{\Omega} (\nabla \mathbf{N}_p)^T \rho_w \frac{\mathbf{k}k_{rw}}{\mu_w} (\rho_w \mathbf{g}) d\Omega + \int_{\Omega} (\nabla \mathbf{N}_p)^T \rho_{gw} \frac{\mathbf{k}k_{rg}}{\mu_g} (\rho_g \mathbf{g}) d\Omega - \int_{\Gamma_w^q} \mathbf{N}_p^T [\bar{q}_w + \bar{q}_{gw}] d\Gamma$$

- Mass balance equation of dry air

$$\mathbf{C}_{gu} = \int_{\Omega} \mathbf{N}_p^T S_g \rho_{ga} \mathbf{m}^T \mathbf{B}_u d\Omega$$

$$\mathbf{C}_{gw} = \int_{\Omega} \mathbf{N}_p^T \left[ nS_g \frac{M_a}{RT} \frac{\partial P_{gw}}{\partial P_c} - n\rho_{ga} \frac{\partial S_g}{\partial P_c} \right] \mathbf{N}_p d\Omega$$

$$\mathbf{C}_{gg} = \int_{\Omega} \mathbf{N}_p^T \left[ nS_g \frac{M_a}{RT} - nS_g \frac{M_a}{RT} \frac{\partial P_{gw}}{\partial P_c} + n\rho_{ga} \frac{\partial S_g}{\partial P_c} \right] \mathbf{N}_p d\Omega$$

$$\mathbf{C}_{gt} = \int_{\Omega} \mathbf{N}_p^T \left[ -nS_g \frac{M_a P_g}{RT^2} - nS_g \frac{M_a}{RT} \left( \frac{\partial P_{gw}}{\partial T} - \frac{P_{gw}}{T} \right) + n\rho_{ga} \frac{\partial S_g}{\partial T} - \beta_{sg} \right] \mathbf{N}_t d\Omega$$

$$\mathbf{K}_{gw} = \int_{\Omega} (\nabla \mathbf{N}_p)^T \rho_g \frac{M_a M_w}{M_g^2} \mathbf{D}_{gw} \frac{1}{P_g} \frac{\partial P_{gw}}{\partial P_c} \nabla \mathbf{N}_p d\Omega$$

$$\begin{aligned} \mathbf{K}_{gg} = \int_{\Omega} (\nabla \mathbf{N}_p)^T \rho_{ga} \frac{\mathbf{k}k_{rg}}{\mu_g} \nabla \mathbf{N}_p d\Omega \\ + \int_{\Omega} (\nabla \mathbf{N}_p)^T \left[ -\rho_g \frac{M_a M_w}{M_g^2} \mathbf{D}_{gw} \frac{1}{P_g} \frac{\partial P_{gw}}{\partial P_c} + \rho_g \frac{M_a M_w}{M_g^2} \mathbf{D}_{gw} \frac{P_{gw}}{(P_g)^2} \right] \nabla \mathbf{N}_p d\Omega \end{aligned}$$

$$\mathbf{K}_{gt} = - \int_{\Omega} (\nabla \mathbf{N}_p)^T \rho_g \frac{M_a M_w}{M_g^2} \mathbf{D}_{gw} \frac{1}{P_g} \frac{\partial P_{gw}}{\partial T} \nabla \mathbf{N}_t d\Omega$$

$$\mathbf{f}_g = \int_{\Omega} (\nabla \mathbf{N}_p)^T \rho_{ga} \frac{\mathbf{k}k_{rg}}{\mu_g} \rho_g \mathbf{g} d\Omega - \int_{\Gamma_g^q} \mathbf{N}_p^T \bar{q}_{ga} d\Gamma$$

- Energy balance equation

$$\mathbf{C}_{tu} = - \int_{\Omega} \mathbf{N}_t^T L_f \rho_i (1-n) S_i \mathbf{m}^T \mathbf{B}_u d\Omega$$

$$\mathbf{C}_{tw} = \int_{\Omega} \mathbf{N}_t^T L_f \rho_i n \frac{\partial S_i}{\partial P_c} \mathbf{N}_p d\Omega$$

$$\mathbf{C}_{tg} = - \int_{\Omega} \mathbf{N}_t^T L_f \rho_i n \frac{\partial S_i}{\partial P_c} \mathbf{N}_p d\Omega$$

$$\mathbf{C}_{tt} = \int_{\Omega} \mathbf{N}_t^T \left[ (\rho C_p)_{\text{eff}} - L_f \rho_i n \frac{\partial S_i}{\partial T} \right] \mathbf{N}_t d\Omega$$

$$\begin{aligned} \mathbf{K}_{tt} = & \int_{\Omega} (\nabla \mathbf{N}_t)^T \lambda_{\text{eff}} \nabla \mathbf{N}_t d\Omega + \int_{\Omega} \mathbf{N}_t^T \left[ \rho_w C_p^w \frac{\mathbf{k} k_{rw}}{\mu_w} (-\nabla P_w + \rho_w \mathbf{g}) \right] \cdot \nabla \mathbf{N}_t d\Omega \\ & + \int_{\Omega} \mathbf{N}_t^T \left[ \rho_g C_p^g \frac{\mathbf{k} k_{rg}}{\mu_g} (-\nabla P_g + \rho_g \mathbf{g}) \right] \cdot \nabla \mathbf{N}_t d\Omega \end{aligned}$$

$$\mathbf{f}_t = - \int_{\Gamma_t^q} \mathbf{N}_t^T [\bar{q}_T] d\Gamma$$

## Preface to Chapter 5

Permafrost regions are facing significant challenges due to global warming, leading to ground instability and other environmental issues. This chapter evaluates the potential of Ground Source Heat Pump (GSHP) systems as a solution for mitigating ground subsidence in thawing permafrost areas. Focusing on a case study in Umiujaq, Quebec, Canada, we employ a two-dimensional Thermo-Hydro-Mechanical (THM) coupled finite element analysis to investigate the interactions between thermal regulation and ground stability. The study examines the effects of different GSHP operation strategies, highlighting the need for careful design and operation to balance thermal benefits with mechanical stresses. By providing a foundational understanding of GSHP impacts in cold climates, this chapter contributes to the development of sustainable energy solutions and climate adaptation strategies in Arctic and subarctic regions.

## Chapter 5

# 5 Numerical evaluation of ground source heat pumps in a thawing permafrost region<sup>3</sup>

### 5.1 Abstract

Permafrost degradation poses significant environmental and geological challenges in Arctic and subarctic regions, particularly in areas like Umiujaq, Canada. The warming climate leads to thawing permafrost, causing ground instability, disrupting hydrology, and impacting local built environment. This study evaluates the use of Ground Source Heat Pump (GSHP) operation for mitigating ground subsidence in a permafrost region using a two-dimensional Thermo-Hydro-Mechanical (THM) coupled finite element analysis considering the ground poro-elastic and poro-plastic responses. The research uses a single-well scenario to demonstrate the interactions among thermal, hydraulic, and mechanical processes. The impact of GSHP operation under different temperature management strategies, including a scenario with a constant GSHP temperature of -5 °C throughout the year is numerically investigated. Results indicate that GSHP operation exacerbates ground deformation near the borehole, particularly during winter months. However, maintaining GSHP operation throughout the entire year can mitigate extreme subsidence fluctuations, leading to a more stable subsurface environment. While GSHP systems provide

---

<sup>3</sup> A version of this manuscript has been published in the Journal of Building Engineering (2024).

effective thermal regulation, their operation can introduce mechanical stresses that potentially disturb the ground close to the borehole. Therefore, careful design, operation, and further research are essential to balance thermal benefits with ground stability in permafrost regions.

**Keywords:** Shallow geothermal energy, Permafrost, Ground subsidence, Thermo-hydro-mechanical coupled analysis

## 5.2 Introduction

The warming climate leads to thawing permafrost, which causes significant changes in slope stability, alters hydrology, and disrupts local ecosystems and built environment (Gruber and Haerberli, 2007). This is especially concerning as permafrost plays an essential role in maintaining ground stability. The degradation of permafrost due to warming temperatures is evidenced by increasing active layer thickness and the northward retreat of permafrost extent, with climatic factors playing a major role (Vasiliev et al., 2020). Further impacts include major implications for hydrology and groundwater dynamics in these regions (Dagenais et al., 2020). Permafrost loss is expected to continue throughout the 21st century, posing a threat to the stability of Arctic infrastructure and the sustainable development of Arctic communities (Hjort et al., 2018; Minsley et al., 2022). Releasing carbon from Arctic permafrost due to warming is also a significant threat as it can impact the climate (Miner et al., 2022). Additionally, thawing permafrost affects vegetation growth, with surface thaw onset changes affecting different stages of the growing season in the Arctic permafrost region (Chen and Jeong, 2024; Young et al., 2020). Also, the release of plant-available nitrogen from thawing permafrost in subarctic peatlands leads to changes in vegetation composition and biomass production (Keuper et al., 2017, 2012), which poses a significant threat to the ecology and environment (Qaidi et al., 2022). Consequently, implementing stabilizing measures in these regions is imperative to mitigate foreseeable geohazards. Recently,

there has been an increase in the use of renewable energy sources for permafrost stabilization. Among these, the Ground Source Heat Pump (GSHP) system has garnered significant attention as it can be a viable option for renewable energy generation for space heating in subarctic regions and could potentially maintain the ground frozen when used in heating mode. With almost 14,045 inhabitants in 2021, Nunavik, which is mostly covered by permafrost, has a good potential to utilize the GSHP systems for heating to reduce the consumption of fuel (Gunawan et al., 2020). GSHP utilizes the stable temperature of the ground to provide heating, cooling, and hot water for residential and commercial buildings. As illustrated in Figure 5-1, a GSHP system comprises ground heat exchangers, a heat pump unit, and a heat distribution system. The ground heat exchangers transfer heat between the ground and the fluid circulating in the system, while the heat pump unit uses this heat to provide heating or remove heat for cooling.

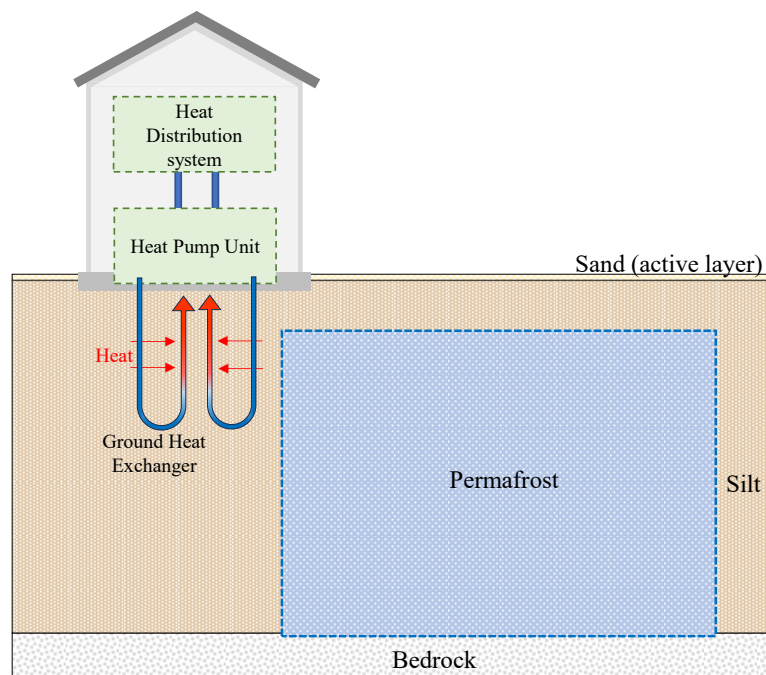


Figure 5-1 Schematic of a ground source heat pump system in a discontinuous permafrost region. GSHPs have emerged as a prominent renewable energy technology for building heating and cooling due to their high energy efficiency and environmental benefits. Sarbu and Sebarchievici,

(2014) provide a comprehensive review of GSHP systems, highlighting their increasing application globally in both residential and commercial buildings. The study highlights the versatility of GSHPs, which can be effectively employed in various climates, contributing to significant reductions in CO<sub>2</sub> emissions. Similarly, [Maghrabie et al., \(2023\)](#) delve into the materials, models, and applications of GSHPs, emphasizing the importance of optimizing thermal performance through careful selection of working fluids and backfill materials. This research indicates that the efficiency of GSHP systems can be significantly enhanced by improving the thermal properties of the ground and reducing the borehole thermal resistance. The findings align with the research of [Ozgener and Hepbasli, \(2007\)](#), which supports the viability of GSHPs as a sustainable energy solution.

Expanding on the potential of GSHP systems, recent studies have explored hybrid configurations to improve performance in specific climates. [Li et al., \(2018\)](#) developed an integrated predictive model to assess the long-term performance of GSHP systems, accounting for dynamic operation characteristics and thermal imbalance effects. Their findings reveal that neglecting these factors can lead to significant performance degradation, underscoring the need for comprehensive modeling in system design. Additionally, [Milenić et al., \(2010\)](#) discuss the application of low enthalpy geothermal energy in Serbia, highlighting the potential for GSHPs to improve energy efficiency in existing residential buildings through the strategic use of subgeothermal groundwater resources. Meanwhile, [Rad et al., \(2013\)](#) investigated the feasibility of combining solar thermal collectors with GSHP systems in cold climates. Their study demonstrates that this hybrid approach can reduce the required ground heat exchanger length by up to 15%, though the economic benefits remain modest. This marks the potential benefits and challenges of GSHP systems in cold regions, highlighting the necessity for more focused studies on optimizing these systems for Arctic and

subarctic environments, where ground temperature stability presents unique design and operational challenges.

In Arctic and subarctic regions, GSHP systems have been less experienced due to the relatively stable ground temperatures. However, numerous experimental and numerical studies have been conducted to evaluate what can be the benefits of geothermal energy systems such as Borehole Thermal Energy Storage (BTES), Ground-coupled heat pump (GCHP), and GSHP system under different near permafrost conditions and have focused on the practical application and energy savings of GSHP systems ([Baser and McCartney, 2015](#); [Bidarmaghz et al., 2016](#); [Catolico et al., 2016](#); [Langevin et al., 2024](#); [Maranghi et al., 2023](#); [Moradi et al., 2015](#); [Moreno et al., 2022](#)). A comprehensive literature review can be found in ([Giordano and Raymond, 2019](#)).

GSHP technology is particularly effective in areas with extreme temperature variations, demonstrating its adaptability and potential environmental benefits in Arctic and subarctic conditions affected by recent climate change ([Baba et al., 2022](#); [Yang et al., 2023](#)). Therefore, the understanding of the complex behavior of frozen soil under freezing and thawing is necessary to simulate permafrost and predict its behavior with and without the exploitation of GSHP systems. Numerical models can help simulate the impacts of freezing and thawing on permafrost, providing insights into future changes and potential impacts on ground stability. Frozen soil poses unique challenges due to its complex behavior under changing thermal, hydraulic, and mechanical conditions. The numerical modeling of THM processes in frozen soil has gathered significant research interest. Thomas et al. and Nishimura et al. explored the THM behavior of soils under seasonal temperature variations in permafrost and seasonally frozen conditions ([Nishimura et al., 2009](#); [Thomas et al., 2009](#)). [Sweidan et al., \(2022\)](#) conducted an experimental and numerical study on THM processes during soil freezing, while [Kebria and Na, \(2024\)](#) proposed a refined THM

framework for modeling frozen soil. Teng et al. provided a review of research development on THM coupling mechanisms in frozen soil (Teng et al., 2022). Bekele et al., 2017 and Fu et al., 2023 proposed fully coupled THM models for frozen soil, while Zheng et al., (2019) developed a finite-element model for freezing processes in saturated soils. Yan et al., (2020) conducted numerical simulations to deepen the understanding of the thawing process in frozen soil. Additionally, models need to incorporate climate-warming-induced changes to accurately simulate permafrost dynamics under changing climatic conditions (Perreault et al., 2021; Thomas et al., 2009). Using phase change strain, Li et al., (2024) also verified their numerical model with field data of highly unsaturated loess located in the northwest of China, using the poro-elastic THM model. Introducing a coefficient to adjust the phase change strain in an unsaturated frozen medium, Norouzi and Li, (2024) developed a poro-plastic numerical model and verified their model with experimental data. Giordano et al., (2019) and Langevin et al., (2024) simulated GSHP operations in the Canadian subarctic climate (using FeFlow). However, their simulations were only for flow and heat transport without considering the geomechanical aspect. The thermally induced irreversible ground deformation (plastic) during the operation of GSHP systems has not been investigated in previous studies.

To fully understand the behavior of Arctic and subarctic regions in the presence of GSHP systems and to address the settlement issues prevalent in these regions, more sophisticated THM models are needed. Preferred models would not only help in predicting and managing the effects of permafrost degradation but also optimize the design and implementation of GSHP systems to ensure they contribute positively to ground stabilization and environmental sustainability. Currently, there is a lack of studies investigating the poro-elastic and poro-plastic response of frozen ground under GSHP operations in cold regions. Without comprehensive multiphysics

modeling of permafrost in geothermal engineering projects, the associated geo-risks are likely to be underestimated. In this study, a THM-coupled FEM model is utilized and boundary conditions are imposed based on the actual site conditions in Umiujaq, Quebec, Canada, where GSHP could potentially be installed. This study introduces a fully coupled THM modeling framework, incorporating freeze-thaw cycles to analyze variables over time. A plasticity model is added to study the irreversible deformation of permafrost. The research focuses on short to long-term analysis, considering seasonal changes and climate change scenarios to assess the sustainability and resilience of GSHP systems. Despite the need for improved field data, existing material properties and data sources were utilized. Also, in the discussion section, two approaches of GSHP operation designs are examined to study permafrost stability, for a comprehensive view of GSHP deployment and environmental sustainability to find an effective and optimum way that keep the stability of the ground.

### 5.3 THM model of saturated frozen soil

This section studies the governing equations of THM-coupled processes in saturated permafrost during freeze-thaw actions. In a saturated frozen medium, comprising soil ( $s$ ), water ( $w$ ), and ice ( $i$ ) phases, the volumetric content is defined as the ratio of the volume of the phase over the total volume. As porosity ( $n$ ) represents the volume of the void over the total volume, water, and ice saturations are the volumetric content over the porosity:

$$S_{\alpha} = \frac{\theta_{\alpha}}{n} = \frac{V_{\alpha}}{V_{void}}, \quad \alpha = w, i \quad (5.89)$$

Based on the physical properties of the freezing and thawing, the governing equations of the THM model are conservation of mass, conservation of energy, and conservation of momentum equations

that are introduced here. A comprehensive explanation of these equations can be found in (Bekele et al., 2017; Lewis and Schrefler, 1998; E Norouzi et al., 2022; Norouzi et al., 2019)

### 5.3.1 Conservation of mass

Given the equality in mass change rates between water and ice during freeze-thaw action, the conservation of the mass equation for water and ice can be expressed as follows:

$$n\rho_w \frac{\partial S_w}{\partial t} + n\rho_i \frac{\partial S_i}{\partial t} - \nabla \cdot (\rho_w n S_w \mathbf{v}_{w,s}) - \beta_{swi} \frac{\partial T}{\partial t} + (S_w \rho_w + S_i \rho_i) \nabla \cdot \frac{d\mathbf{u}}{dt} = 0 \quad (5.90)$$

Here,  $\rho_\alpha$  denotes the density of phase  $\alpha$ ,  $\mathbf{v}_{w,s}$  represents the velocity of water relative to soil,  $\beta_{swi}$  stands for the equivalent thermal expansion coefficient, and  $\mathbf{u}$  signifies the displacement of the medium (Gawin et al., 2020).

#### 5.3.1.1 Modified Clausius-Clapeyron equation

Considering  $L_f$  is the latent heat and  $T_0 = 273.15$  K represents the reference temperature, the modified Clausius-Clapeyron equation delineates the correlation among temperature ( $T$ ), ice pressure ( $P_i$ ), and pore water pressure ( $P_w$ ) within frozen soil as follows (Kurylyk and Watanabe, 2013):

$$\frac{L_f}{T_0} dT = \frac{dP_w}{\rho_w} - \frac{dP_i}{\rho_i} \quad (5.91)$$

#### 5.3.1.2 Soil-freezing characteristic curve

In this study, a Soil-Freezing Characteristic Curve (SFCC) is defined based on model of Van Genuchten, (1980). Under freezing point temperature, the degree of saturation of water and ice can be estimated as follows:

$$S_e = (1 + [\alpha_v(P_i - P_w)]^{n_v})^{-m_v}$$

$$S_w = S_{wr} + (1 - S_{wr})S_e \quad (5.92)$$

$$S_i = 1 - S_w$$

where  $S_e$  and  $S_{wr}$  denote effective and residual water phase saturation. Also,  $\alpha_v$ ,  $m_v$ , and  $n_v$  represent the curve fitting parameters.

### 5.3.1.3 Darcy's law

To determine the hydraulic conductivity at a specific temperature, a relative hydraulic conductivity parameter is introduced. At the macro-scale level, the volume-averaged advective flux of liquid water, driven by pressure gradients, can be expressed using Darcy's law (Gawin et al., 2019):

$$nS_w \mathbf{v}_{w,s} = \frac{\mathbf{k}k_{rw}}{\mu_w} (-\nabla P_w + \rho_w \mathbf{g}) \quad (5.93)$$

in which  $\mathbf{k} = k\mathbf{I}$  denotes intrinsic permeability,  $\mu_w$  is viscosity,  $\mathbf{g}$  represents gravity acceleration, and  $k_{rw}$  is the relative permeability for water:

$$k_{rw} = \sqrt{S_e} \left[ 1 - \left( 1 - S_e^{\frac{1}{m_v}} \right)^{m_v} \right]^2 \quad (5.94)$$

### 5.3.2 Conservation of energy

The energy balance equation for the medium assumes that all phases are in a state of local thermodynamic equilibrium and ignores heat transfer between the phases. It can be expressed as:

$$(\rho C_p)_{\text{eff}} \frac{\partial T}{\partial t} + \mathbf{a} \cdot \nabla T + \nabla \cdot \tilde{\mathbf{q}} - L_f \rho_i \frac{\partial \theta_i}{\partial t} = 0 \quad (5.95)$$

The effective heat capacity  $(\rho C_p)_{\text{eff}}$  in Equation 5.7 is defined as a combination of the solid, water, and ice phase heat capacities, weighted by their respective volumetric fractions:

$$(\rho C_p)_{\text{eff}} = (1 - n)\rho_s C_p^s + nS_w \rho_w C_p^w + nS_i \rho_i C_p^i \quad (5.96)$$

The advection term  $\mathbf{a}$  in Equation 5.9 represents the heat transfer due to relative velocities between water and solid:

$$\mathbf{a} = nS_w \rho_w C_p^w \mathbf{v}_{w,s} \quad (5.97)$$

Also, the conductive heat flux term ( $\tilde{\mathbf{q}}$ ) in the energy balance equation is assumed to follow Fourier's law below the freezing point of water and can be expressed as:

$$\tilde{\mathbf{q}} = -\lambda_{\text{eff}} \nabla T \quad (5.98)$$

Here,  $\lambda_{\text{eff}}$  is the overall thermal conductivity of porous media depends on the thermal conductivities of the individual phases and their corresponding volumetric fractions:

$$\lambda_{\text{eff}} = \lambda_s^{1-n} \lambda_w^{nS_w} \lambda_i^{nS_i} \quad (5.99)$$

### 5.3.3 Conservation of linear momentum

Considering  $\nabla = \langle \partial/\partial x \quad \partial/\partial y \quad \partial/\partial z \rangle$  as the gradient operation and " $\cdot$ " denotes the dot product, the balance between the divergence of the total stress tensor ( $\boldsymbol{\sigma}$ ) and body force ( $\mathbf{b}$ ) is defined by the conservation of linear momentum equation as follow:

$$\nabla \cdot \boldsymbol{\sigma} + \mathbf{b} = \mathbf{0} \quad (5.100)$$

The total stress can be approximated using the effective stress ( $\boldsymbol{\sigma}'$ ) and pore pressure components the saturations of each of them is used as weight coefficients (Bekele et al., 2017; Yin et al., 2023):

$$\boldsymbol{\sigma} = \boldsymbol{\sigma}' - S_w P_w \mathbf{I} - S_i P_i \mathbf{I} \quad (5.101)$$

Introducing  $\mathbf{D}_T$  as the tangential constitutive matrix, a relation between effective stress and effective strain can be established as follow:

$$d\boldsymbol{\sigma}' = \mathbf{D}_T (d\boldsymbol{\varepsilon} - d\boldsymbol{\varepsilon}^{\text{ph}} - d\boldsymbol{\varepsilon}^T) \quad (5.102)$$

where:

$$d\boldsymbol{\varepsilon}^{\text{ph}} = \frac{1}{3} \left( \frac{n(\rho_w - \rho_i)}{\rho_w S_w + \rho_i S_i} ds_i \right) \mathbf{I} \quad (5.103)$$

$$d\boldsymbol{\varepsilon}^T = \frac{\beta_s}{3} dT \mathbf{I} \quad (5.104)$$

Here,  $d\boldsymbol{\varepsilon}$  represents the total strain increment vector and  $d\boldsymbol{\varepsilon}^{\text{ph}}$  denotes the increment strain due to phase change based on the mass balance of water and ice. Additionally,  $d\boldsymbol{\varepsilon}^T$  is the thermal strain increment while  $\beta_s$  as the thermal expansion coefficient of the solid skeleton.

The nonlinear behavior of saturated frozen soil is modeled using an associative Drucker-Prager model. The yield function, described as follows, encapsulates this approach:

$$\Pi(\boldsymbol{\sigma}', c) = \sqrt{\frac{1}{2} \mathbf{s}(\boldsymbol{\sigma}') : \mathbf{s}(\boldsymbol{\sigma}') + \eta p'(\boldsymbol{\sigma}') - \xi c} \quad (5.105)$$

In this model,  $\mathbf{s}(\boldsymbol{\sigma}')$  and  $p'(\boldsymbol{\sigma}')$  correspond to the deviatoric stress and hydrostatic pressure of the effective stress, respectively, while  $c$  represents cohesion. Parameters  $\eta$  and  $\xi$  are adjusted based on the Mohr-Coulomb plasticity model for a 2D plane strain:

$$\eta = \frac{3 \tan \phi}{\sqrt{9 + 12 \tan \phi}} \quad (5.106)$$

$$\xi = \frac{3}{\sqrt{9 + 12 \tan \phi}}$$

where  $\phi$  is the friction angle. Details about adjustments in stress-strain behavior and the formulation of the tangential stiffness matrix are further elaborated by [de Souza Neto et al., \(2011\)](#), emphasizing the hardening parameters are a function of temperature.

### 5.3.4 Spatial and time discretization

Following the introduction of the governing and auxiliary equations, the next step is to derive the weak forms of the governing equations (i.e., [Equations 5.2, 5.7, and 5.12](#)). By considering both the essential and natural boundary conditions, the collection of coupled equations can then be reformulated into a discretized nonlinear differential equation in terms of time:

$$\mathbf{KX} + \mathbf{C} \frac{d\mathbf{X}}{dt} = \mathbf{F} \quad (5.107)$$

where  $\mathbf{X}^T = [\mathbf{u} \quad \mathbf{P}_w \quad \mathbf{T}]$  represents the vector of principal variables including displacement, pore water pressure, and temperature. Additionally,  $\mathbf{F}$  stands as the force vector, and  $\mathbf{K}$  and  $\mathbf{C}$  are coefficients that depend on the primary parameters of the system. Consequently, [Equation 5.19](#) exhibits significant nonlinearity.

To handle the numerical solution of this nonlinear differential equation, a fully implicit method is employed for time discretization. This approach ensures stability and accuracy for stiff equations. The solution to [Equation 5.19](#) is then obtained using the Newton-Raphson scheme, which efficiently tackles the nonlinearities by iteratively linearizing the equations at each time step. Details including the numerical stability treatments can be found in ([Goudarzi and Mohammadi, 2015](#); [Lewis and Schrefler, 1998](#)).

## 5.4 Validation of the numerical tool

Based on the equations of the THM model explained in Section 2 an in-house MATLAB code is developed. To validate the numerical model, an experiment conducted by [Fukuda et al., \(1997\)](#) is selected. In this experiment, a cylindrical specimen measuring 100 mm in diameter and 70 mm in height comprised 60 % clay, 37 % silt, and 3 % sand is utilized. The specimen with an initial porosity of 0.43 and specific gravity of 2.62 is subjected to a controlled temperature gradient for one step-freezing test. Some other THM coupled numerical models also used this experimental data for numerical validations ([Vosoughian and Balieu, 2023](#); [Zhang and Michalowski, 2015](#)). However, it should be noted that the thermally induced plastic deformation behavior was not involved in the previous numerical models.

Initially, the temperature of the sample is set at 5 °C, and hydraulic pressure is assumed along the sample. The test commenced by rapidly reducing the temperature on the bottom side to -5 °C. The numerical model and boundary conditions are depicted in [Figure 5-2](#). In this model, a structured mesh with a size of 10 mm × 10 mm has been chosen for a 2D plane strain model with dimensions of 100 mm × 700 mm. To increase the accuracy of the displacement field, second-order shape functions have been selected for displacement, while linear shape functions are used for pressure and temperature.

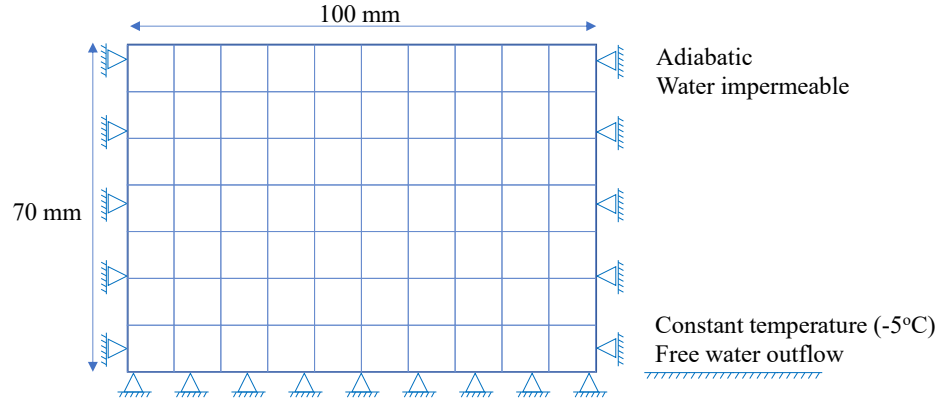


Figure 5-2 The numerical mesh and boundary conditions of the numerical test for validation. The SFCC model parameters are extracted from Fukuda et al.'s dataset by fitting them with van Genuchten's function based on Vosoughian and Balieu, (2023). The effective elastic modulus and Poisson's ratio are defined as a function of ice elastic properties of soil and ice as well as ice saturation that should be recalculated at each time step.

$$E = \left(\frac{E_i}{E_s}\right)^{s_i^\eta} E_s \quad (5.108)$$

$$\nu = \left(\frac{\nu_i}{\nu_s}\right)^{s_i^\eta} \nu_s$$

In Equation 5.20,  $E_i$  and  $E_s$  are the elastic modulus of ice and soil,  $\nu_i$  and  $\nu_s$  are the Poisson's ratio of ice and soil, and  $\eta$  is a model parameter. Table 5-1 presents the thermal, hydraulic, and mechanical characteristics of the soil.

Table 5-1 Thermal, hydraulic, and mechanical properties of the numerical THM model.

Properties	Value
Initial porosity	$n = 0.43 (-)$
Density of soil	$\rho_s = 2620 (\text{kg/m}^3)$
Density of ice	$\rho_i = 910 (\text{kg/m}^3)$
Density of water	$\rho_w = 1000 (\text{kg/m}^3)$
Intrinsic permeability	$\mathbf{k} = 1 \times 10^{-14} (\text{m}^2)$
Dynamic viscosity of water	$\mu_w = 1 \times 10^{-3} (\text{Pa}\cdot\text{s})$
van Genuchten's model parameter	$\alpha_v = 2.6 \times 10^{-7} (\text{Pa}^{-1})$
van Genuchten's model parameter	$n_v = 1.85 (-)$

van Genuchten's model parameter	$m_v = 0.46 (-)$
Elastic modulus of soil	$E_s = 7.5 \text{ (MPa)}$
Elastic modulus of soil	$E_i = 9.1 \text{ (GPa)}$
Poisson's ratio of soil	$\nu_s = 0.2(-)$
Poisson's ratio of soil	$\nu_i = 0.4 (-)$
Model parameter	$\eta = 2.4 (-)$
Specific heat capacity of soil	$C_s = 2360 \text{ (J/kg/K)}$
Specific heat capacity of ice	$C_i = 1930 \text{ (J/kg/K)}$
Specific heat capacity of water	$C_w = 4180 \text{ (J/kg/K)}$
Thermal conductivity of soil	$\lambda_s = 1.95 \text{ (W/m/K)}$
Thermal conductivity of ice	$\lambda_i = 2.24 \text{ (W/m/K)}$
Thermal conductivity of water	$\lambda_w = 0.56 \text{ (W/m/K)}$
Latent heat of fusion	$L_f = 3.34 \times 10^5 \text{ (J/kg)}$
Reference temperature	$T_0 = 273.15 \text{ (K)}$

---

The freezing process test continued for 115 hours. The comparison between the simulated curve and the experimental data is illustrated in [Figure 5-3](#). As depicted in [Figure 5-3](#), the comparison between the simulated results and the experimental data demonstrated a notable degree of alignment. This alignment signifies a positive validation of the model's predictive capacity, highlighting its accuracy in capturing the thermal, hydraulic, and mechanical behavior of the soil under freezing conditions.

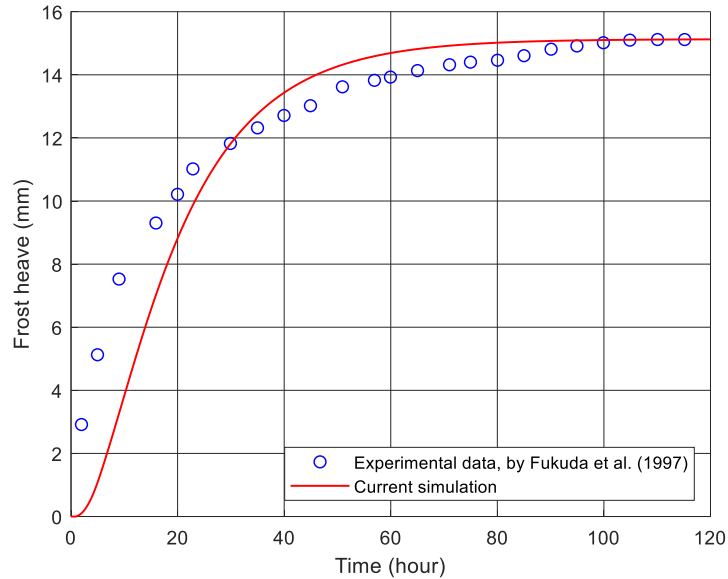


Figure 5-3 Comparison of simulated and experimental data for the freezing test.

## 5.5 FEM modeling of a GSHP well in Umiujaq

Umiujaq is an Inuit community of approximately 440 residents situated north of Tasiujaq Lake and near the eastern shore of Hudson Bay, a large, shallow intracratonic sea in the central Canadian Shield. This region lies in an area of discontinuous permafrost, which is currently degrading due to climate warming (Wang et al., 2020). Dominant permafrost landforms in Umiujaq include lithalsas (mineral permafrost mounds), permafrost plateaus (broad, elongated mineral permafrost formations), palsas (permafrost mounds covered with peat), and peat plateaus (broad, elongated peaty permafrost formations) (Jolivel and Allard, 2013). Most village infrastructure is constructed on raised sandy beaches, which are thaw-stable materials, while roads and airfields are partially built on frozen, ice-rich marine sediments—thaw-unstable materials—either exposed or covered by sand (Fortier et al., 2011). Umiujaq experiences a subarctic climate with a mean annual air temperature of about  $-3\text{ }^{\circ}\text{C}$ . Winters are very cold, and summers are cool, with average monthly temperatures of  $-24\text{ }^{\circ}\text{C}$  in January and  $10\text{ }^{\circ}\text{C}$  in August. The mean annual precipitation is around 645 mm, with most occurring from July to January, and snowfall accounts for about 50% of the

total precipitation (Wang et al., 2020). We have selected Umiujaq as the site to simulate a GSHP borehole, utilizing available geological and hydrothermal characterization data (Giordano and Raymond, 2019).

### 5.5.1 Model description

To investigate the subsidence of a GSHP system, a 2D plane strain model was created. The numerical model's parameters were primarily sourced from research projects conducted in Umiujaq, located in Nunavik, Quebec, Canada (Dagenais et al., 2020; Perreault et al., 2021). The discontinuous ice-rich permafrost layer was characterized based on findings from study of Perreault et al., (2021), encased within silty sediment. The dimensions of the model, as depicted in Figure 5-4a, were selected to be sufficiently large to ensure compliance with infinite boundary conditions, spanning an area of 15 m × 30 m. Because of the complexities of drilling boreholes in permafrost zones, it was assumed that the GSHP system operates within the silty sediment layer (Figure 5-4a). Given the model's symmetry, the borehole was positioned at the top left side, extending to a depth of 7.5 m. The stratigraphy includes an active sand layer at the surface, a silt layer, and a substantial permafrost layer overlying bedrock. This configuration simulates the interactions between the GSHP system and the surrounding permafrost, providing valuable insights into the THM behavior of the system.

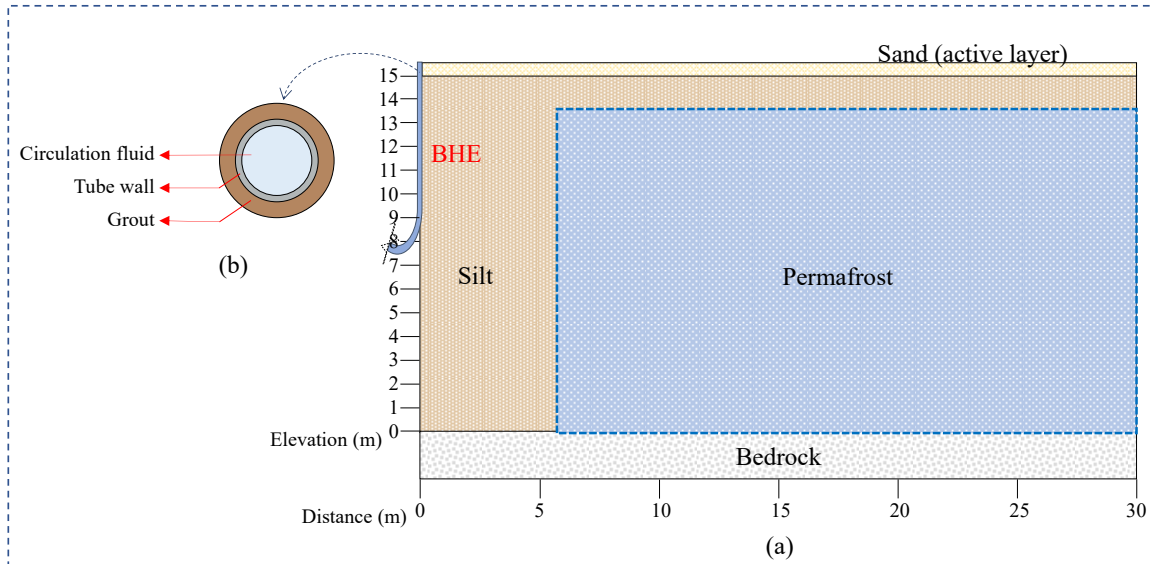


Figure 5-4 (a) Schematic representation of the 2D model used for investigating the ground response of a GSHP system in Umiujaq and (b) a cross section of a borehole heat exchanger.

In this study, a borehole heat exchanger with a single U-shaped pipe (1U) is assumed which consists of one inlet and one outlet pipe embedded in the tube wall filled with grout material (Figure 5-4(b)). The thermal characteristics of the tube wall, grout, and circulating fluid can be found in (Diersch et al., 2011; Jiang et al., 2022; Liu et al., 2024).

The temperature of the Borehole Heat Exchanger (BHE) was imposed on the borehole's boundary condition as the Robin-type boundary condition of heat flux (i.e.,  $q = \lambda_b(T - T_e)$ ), where as  $\lambda_b \cong 7.5$  (W/m/K) represents the average heat conductivity of borehole components, and  $T_e$  denotes the constant temperature of the GSHP). Additionally, seasonal temperature variations were applied as Dirichlet boundary conditions at the top surface for each time step. Based on the ground surface, imposed seasonal temperature should be adjusted using a coefficient that is different in freezing and thawing conditions.

Daily air temperatures were extracted from the local weather station (QC\_7108564) in Umiujaq, covering the period from June 2021 to June 2023. Figure 5-5a depicts the minimum, maximum,

and mean temperatures in Umiujaq during this period. During the winter months from November to May, with air temperature falling below 0°C, the climate sees minimum temperatures plunging below -30°C, mean temperatures normally ranging around -25 °C to -5 °C, and maximum temperatures barely reaching 0°C. The summer months of Umiujaq from June to September are usually cool, with minimum temperatures around 10°C, mean temperatures below 20°C, and maximum temperatures approaching 25°C. In the numerical model, air temperature variations were assumed to be linear, as shown in [Figure 5-5b](#). Additionally, the GSHP temperature was maintained at a constant -5°C, except for June and July when the system was shut down ([Figure 5-5b](#)). Based on [Figure 5-5a](#), the onset of air temperatures dropping below -5°C, typically begins in early to mid-November and lasts until temperatures climb above -5°C by mid to late April.

Climate change-induced variations in the freezing and thawing patterns could significantly impact the long-term performance and sustainability of GSHP systems in permafrost regions. A shorter cold season, delayed freezing, deeper thawing, and increased temperature variability would likely reduce system efficiency, intensify permafrost degradation, and increase mechanical stress on the ground. To mitigate these effects, the design and operational strategies of GSHP systems must evolve to account for changing climate conditions, ensuring that they continue to function effectively while minimizing their impact on permafrost stability. Therefore, in the Discussion section, another approach for GSHP operation is introduced and compared with the current model.

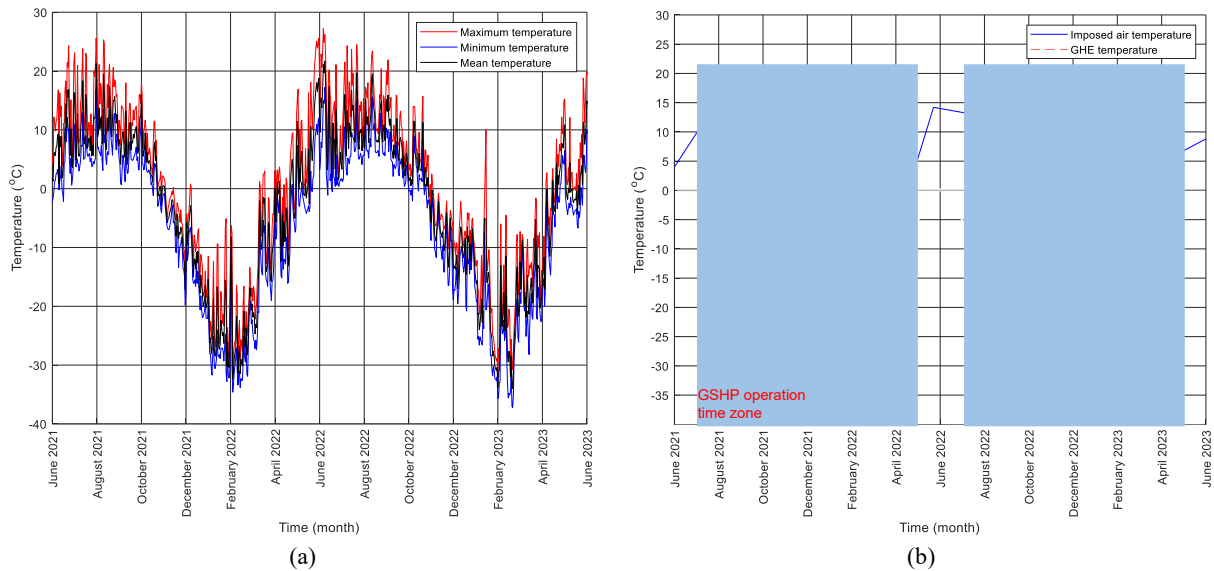


Figure 5-5 (a) Maximum, minimum, and mean measured air temperatures in Umiujaq and (b) temperature variations of air and GHE in the current simulation.

In order to estimate the ground temperature, different methods have been introduced recently. [Gheysari et al., \(2021\)](#), introduced an AI framework to assess the ground temperature trained by air and ground temperature measurements at the nearby weather station. Also, [Perreault et al., \(2021\)](#) has assessed coefficients at both above and under freezing points for different ground surfaces. In this study, the ground surface condition on the top of the permafrost mound is assumed moss and lichen coverage. The coefficients (during freezing and thawing) of transferring air temperature to the ground surface temperature are included in [Table 5-2](#). The right edge was maintained adiabatic, while the bottom side retained a constant temperature. Regarding displacement boundary conditions, horizontal and vertical displacements were restricted at the bottom, while horizontal displacement was fixed on the right and left sides. Apart from the top edge, which was drained, other boundaries were considered impermeable.

Initially, the temperature of the permafrost region and silty sediment was set at  $-2\text{ }^{\circ}\text{C}$  and  $7\text{ }^{\circ}\text{C}$ , respectively, with pore water pressure distributed according to hydrostatic conditions ([Perreault et al., 2021](#)). In this study, the van Genuchten's parameters of the SFCC model are extracted by fitting

the curve on data of silty clay provided by Wang et al., (2021) as shown in Figure 5-6. Other thermal and hydraulic properties of the model, obtained from various references, are detailed in Table 5-2.

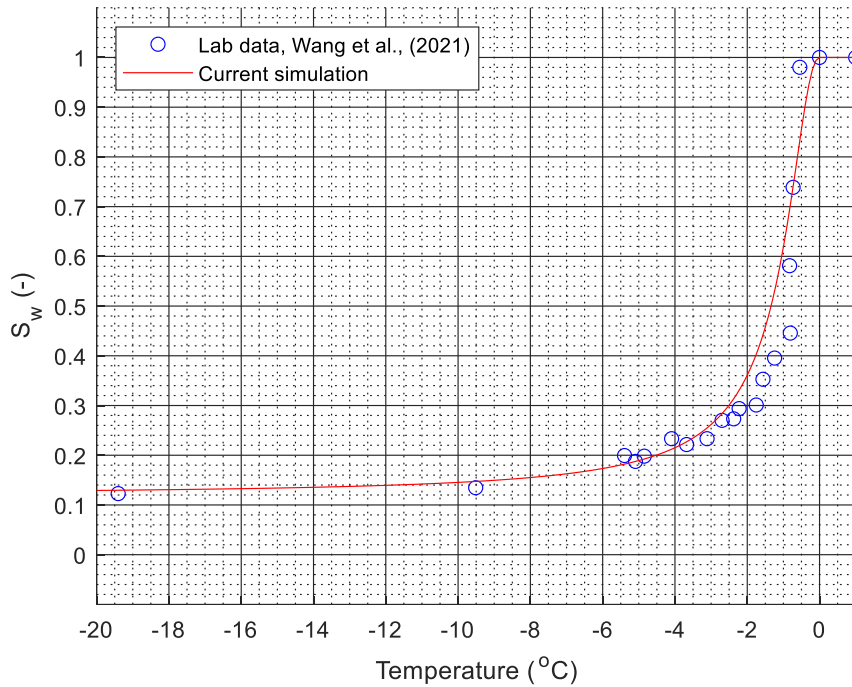


Figure 5-6 Calibration of the SFCC model parameters based on lab data.

Table 5-2 Thermal and hydraulic properties of the current simulation

Properties	Value
Initial porosity (Perreault et al., 2021)	$n = 0.4$ (-)
Intrinsic permeability (Perreault et al., 2021)	$\mathbf{k} = 1 \times 10^{-13}$ (m <sup>2</sup> )
Density of soil	$\rho_s = 2630$ (kg/m <sup>3</sup> )
Density of ice	$\rho_i = 910$ (kg/m <sup>3</sup> )
Density of water	$\rho_w = 1000$ (kg/m <sup>3</sup> )
Dynamic viscosity of water	$\mu_w = 1 \times 10^{-3}$ (Pa.s)
van Genuchten's model parameter	$\alpha_v = 1.0 \times 10^{-6}$ (Pa <sup>-1</sup> )
van Genuchten's model parameter	$n_v = 2.1$ (-)
van Genuchten's model parameter	$m_v = 0.7$ (-)
Specific heat capacity of soil	$C_s = 2400$ (J/kg/K)
Specific heat capacity of ice	$C_i = 1874$ (J/kg/K)
Specific heat capacity of water	$C_w = 4180$ (J/kg/K)
Thermal conductivity of soil (Perreault et al., 2021)	$\lambda_s = 2.7$ (W/m/K)
Thermal conductivity of ice	$\lambda_i = 2.22$ (W/m/K)

Thermal conductivity of water	$\lambda_w = 0.58$ (W/m/K)
Latent heat of fusion	$L_f = 3.45 \times 10^5$ (J/kg)
Reference temperature	$T_0 = 273.15$ (K)
Freezing adjusting coefficient (Perreault et al., 2021)	$m_{\text{freezing}} = 0.655$
Thawing adjusting coefficient (Perreault et al., 2021)	$m_{\text{thawing}} = 0.636$

Additionally, the mechanical properties of the model at different temperatures are provided in Table 5-3. Linear interpolation and extrapolation were used to calculate the mechanical properties (Zheng et al., 2010). Currently, measured temperature-dependent mechanical properties are not available. The mechanical properties are estimated based on the information on porosity and mineralogical composition that are closely related to deformation properties and strength (Li and Wong, 2016). Data on the mechanical properties of frozen soils at different geological origins are collected as a database for matching with the similarity in petrophysical properties (Andersland and Ladanyi, 2003; Zheng et al., 2010).

Table 5-3 Temperature-dependent mechanical parameters of geomaterials used in the modeling at the Umiujaq site.

Temperature (°C)	-20	-10	-5	-2	-1	-0.05	0	20
Elastic modulus (MPa)	72.6	61.3	50.8	45.0	40.0	36.9	34	34
Poisson's ratio (-)	0.13	0.13	0.13	0.14	0.16	0.35	0.45	0.45
Cohesion (MPa)	0.6	0.6	0.6	0.6	0.6	0.15	0.003	0.003
Friction angle (°)	34	34	34	34	34	31	30	30

### 5.5.2 Mesh sensitivity analysis

In this study structured rectangular meshes with same size are selected. In order to increase the stability of the problem, linear shape function for interpolation of water pressure and temperature and second order shape function for interpolation of displacement has been chosen. Additionally, a mesh sensitivity analysis is conducted to ensure that the selected mesh resolution is sufficient for accurately capturing THM processes in the GSHP operation and surrounding permafrost. The mesh sensitivity study involved testing various mesh sizes: starting from a coarser mesh of 1.5 m

× 0.5 m, then refining the mesh through 1 m × 0.5 m, 0.75 m × 0.5 m, 0.6 m × 0.5 m, and finally 0.5 m × 0.5 m. Figure 5-7 shows an example of the numerical meshing.



Figure 5-7 The selected FEM mesh and monitoring points for numerical analysis.

To conduct mesh sensitivity analysis, two monitoring points have been selected as shown in Figure 5-7: ground displacement around the borehole (P1) and temperature at the right edge of the model at a depth of 3 m (P6). The results of mesh sensitivity analysis of two monitoring points during the analysis are depicted in Figure 5-8.

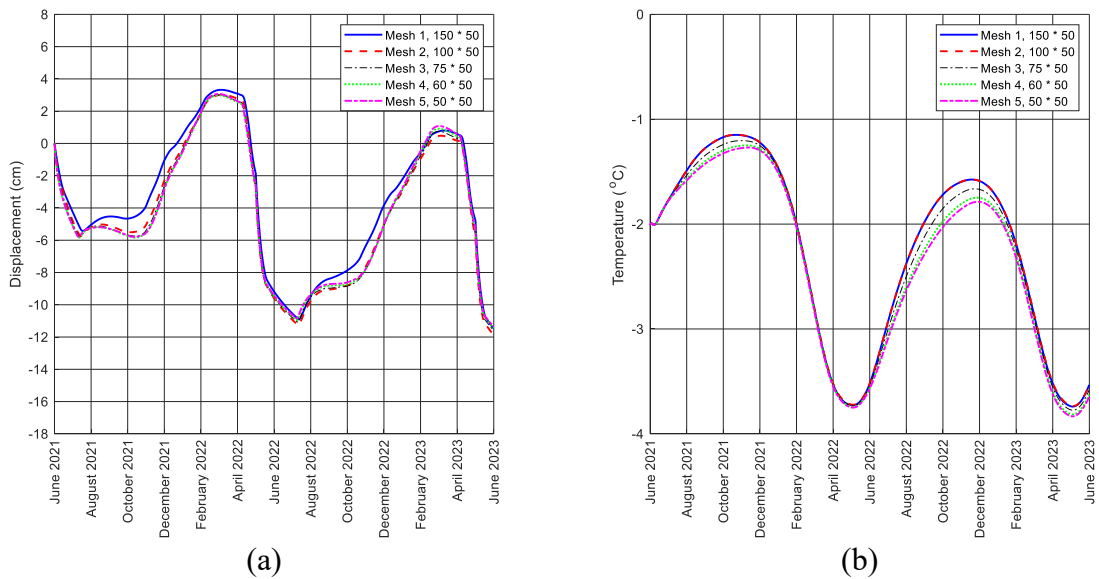


Figure 5-8 Curves showing the mesh sensitivity analysis results: (a) the displacement around borehole (P1), and (b) the temperature at the right edge with a depth of 3 m (P6).

The mesh sensitivity study demonstrates that the model results converge as the mesh is refined, particularly at a resolution of  $0.5 \text{ m} \times 0.5 \text{ m}$ . Given the minimal differences in both temperature and displacement results between the finer meshes, the  $0.5 \text{ m} \times 0.5 \text{ m}$  mesh size is selected for this simulation, providing a good balance between accuracy and computational efficiency. This resolution is sufficient to accurately capture the THM processes in the context of the modeled GSHP system and permafrost environment.

Following the mesh sensitivity analysis, contours of temperature variations, water pressure distributions, ice saturation, and ground deformation were analyzed at specific time frames over the two-year period. The time frames were captured in mid-July, September, February, and April, representing the hot days after GSHP activation, the beginning of fall, the coldest days in winter, and spring days before GSHP deactivation, respectively.

### **5.5.3 Temperature variations**

As shown in [Figure 5-9](#), the simulated temperature contours from July 2021 to April 2023 demonstrate significant seasonal fluctuations within the permafrost and silty sediment layers. In the middle of July 2021 and July 2022, after the GSHP system was turned on, the temperature profiles indicate warmer conditions at the surface, with temperatures reaching up to  $9 \text{ }^\circ\text{C}$  while the permafrost remained below freezing.

During the hottest periods at the middle of September 2021 and 2022, the ground surface experiences the warming, which extends deeper into the subsurface. However, the cooling effect of the GSHP system can be observed, particularly around the borehole area, where temperatures are relatively lower. In contrast, during the cold periods at the middle of February 2022 and 2023, the entire subsurface, including the permafrost and silty sediment, experiences significant cooling

and widespread freezing conditions, with temperatures dropping as low as  $-19\text{ }^{\circ}\text{C}$ . By April 2022 and 2023, the transition from winter to summer is evident as temperatures begin to rise again, particularly near the surface. The ground starts to warm up, but the deeper layers remain relatively cooler, maintaining the integrity of the permafrost.

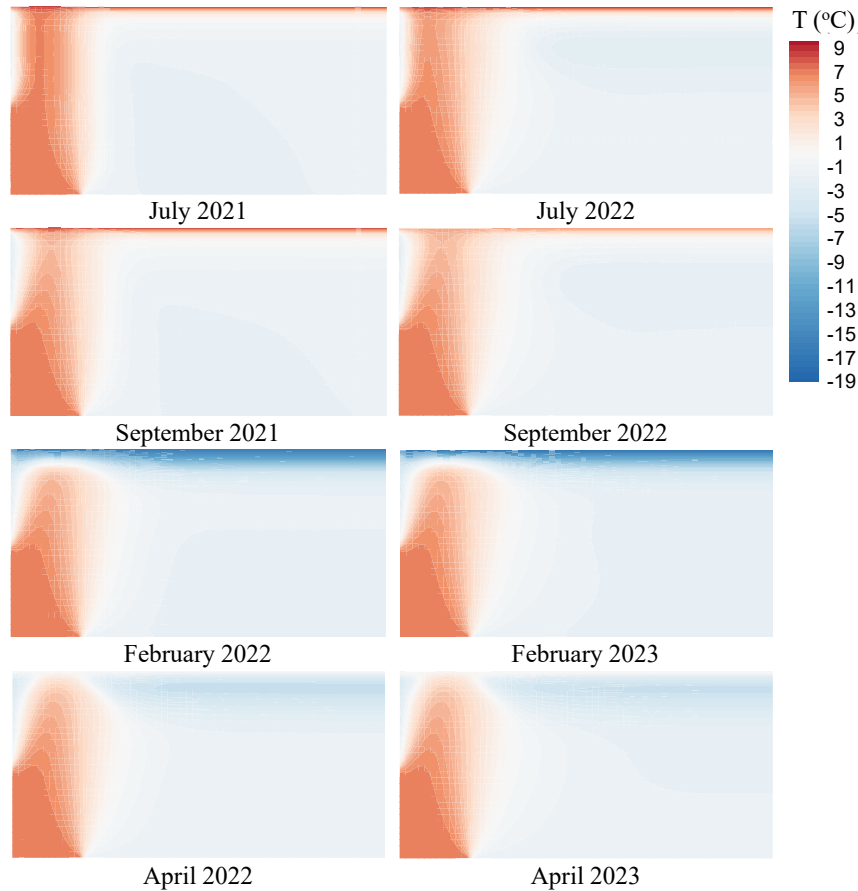


Figure 5-9 Simulated temperature ( $^{\circ}\text{C}$ ) contours over selected time frames within two years.

#### 5.5.4 Pore water pressure distributions

The contours of pore water pressure distributions are shown in [Figure 5-10](#) for the selected time frames. As mentioned in [Section 5.5.1](#), the model assumes an initial hydrostatic pressure. During both summer periods, the pore water pressure distribution is largely positive, with values reaching

up to 150 kPa near the surface. This high pore water pressure indicates thawing permafrost and elevated groundwater levels. As expected, during the warm months, the frozen ground thaws, allowing pore water pressure to increase as liquid water becomes more prevalent within the soil matrix. As the ground begins to cool, the contours show a slight reduction in pressure values, particularly in the upper soil layers, indicating the onset of ground freezing, which reduces pore water pressure as ice formation restricts water movement.

The winter months exhibit the most significant changes in pore water pressure. During this period, pore water pressure drops sharply, with values as low as -490 kPa. This is consistent with the freezing of groundwater in the permafrost layer, leading to negative pore water pressures as water freezes, expands, and reduces the volume of liquid water, creating suction pressures. The extent of this negative pressure is most pronounced in the upper soil layers, where freeze-thaw cycles are most active.

By spring, pore water pressure begins to recover from its winter lows. The contour maps for April 2022 and 2023 show a gradual increase in pressure, especially near the surface. This reflects the thawing of the active layer as temperatures rise, allowing water to flow more freely, resulting in positive pore water pressures. However, the pressure values remain lower than during the summer months, indicating that the ground has not fully thawed.

Although the GSHP reduces the temperature around the borehole and causes freezing, its impact is negligible in September. However, as shown in February, since the temperature around the borehole is warmer than at the surface, the pore water pressure is slightly higher near the borehole than on the rest of the surface. The observed patterns of pore water pressure variation align with

expectations for permafrost environments subjected to both natural seasonal temperature variations and artificial thermal stresses induced by GSHP operations.

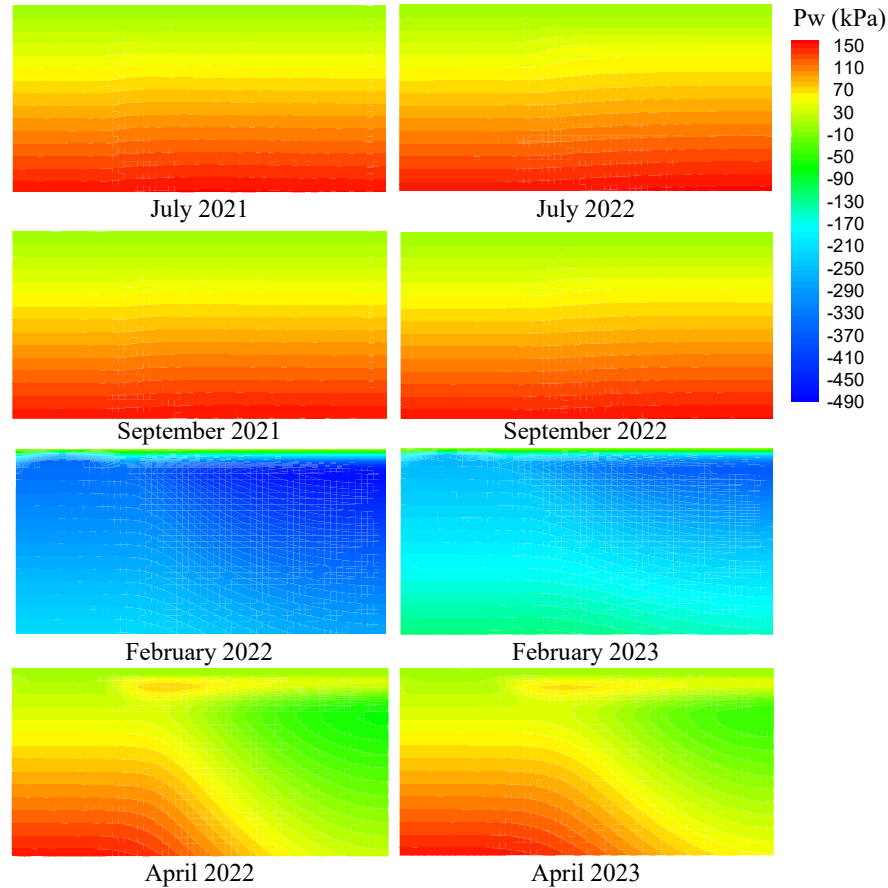


Figure 5-10 Water pressure distribution contours over selected time frames within two years.

### 5.5.5 Ice saturation variations

The contours of ice saturation profiles from July 2021 to April 2023 are depicted in [Figure 5-11](#).

The ice saturation value is high in the deeper permafrost regions, with values close to 0.85. The near-surface layers, however, exhibited lower ice saturation due to the summer warming, as indicated by the red and yellow regions. This pattern of reduced ice content near the surface during the summer months is consistent across both years. However, the effect of ice growing around the borehole after activation of GSHP system in July 2021 and July 2022 is shown, after the GSHP system was activated.

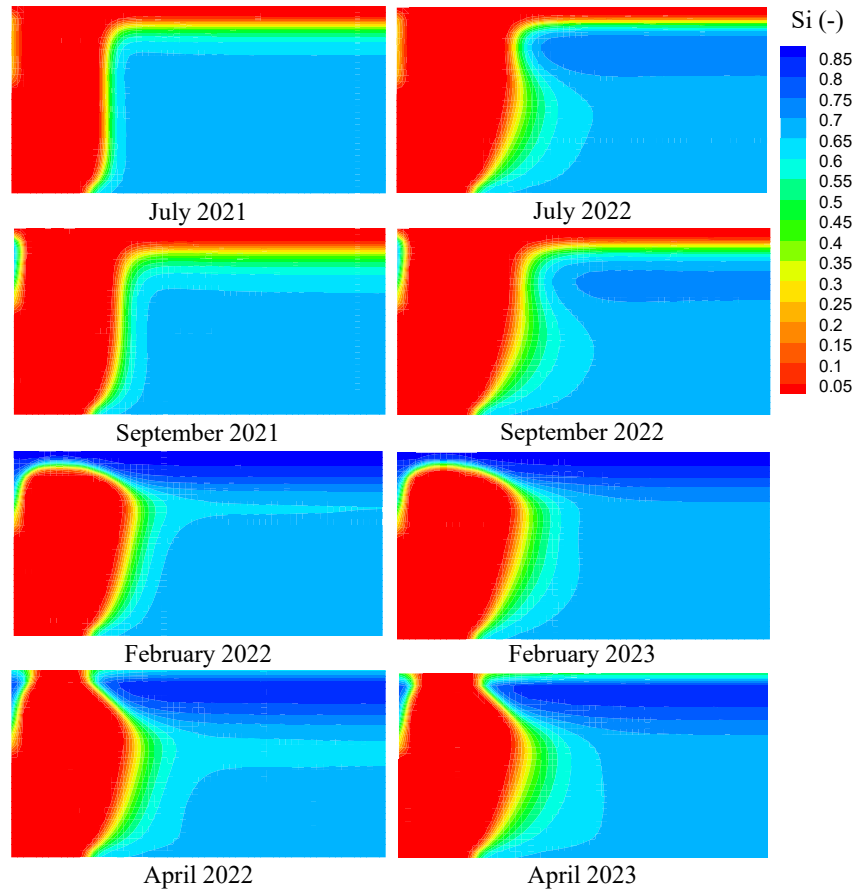


Figure 5-11 Simulated ice saturation over selected time frames within two years

During September 2021 and 2022, the ice saturation near the surface remains low, and because of the warm temperature during summer, the size of permafrost reduced, while the ice saturation around the borehole is still growing and it is around 50 percent of the void medium. By February 2022 and 2023, the coldest periods, the ice saturation increases significantly near the surface, as indicated by the expanded blue regions. Permafrost maintains high ice saturation levels throughout these cold periods. By May 2022 and 2023, the transition from winter to summer results in a gradual decrease in ice saturation near the surface, though deeper layers remain largely unaffected. However, the ice-saturated region in May 2023 is slightly less than in May 2022 due to the warming climate. Also, as shown in April and July 2022, during the time that GSHP is deactivated,

the ice around the borehole is thawed very fast, which may create noticeable drop in settlement of the borehole region shown in following sections.

### 5.5.6 Ground subsidence

Figure 5-12 presents the ground deformation from July 2021 to April 2023 and demonstrates the impact of seasonal temperature changes and the operation of the GSHP system on subsurface deformation. In July 2021, after activating the GSHP system, the subsidence is relatively uniform with minimal deformation which is due to the thawing of permafrost and the associated settlement of the ground, as indicated in Figure 5-12. The settlement of silty region is more than permafrost region because of its lower stiffness. In September 2021, the effect of frost heave due to GSHP operation around the borehole is highlighted and can help to the stabilization of the borehole. The coldest periods in February 2022 and 2023 show the most noticeable subsidence in the silty region, while the silty layers above the permafrost experience considerable frost heave due to cold season. The frost heave due to the GSHP system's cooling effect around the borehole has also been highlighted.

By April 2022 and 2023, as temperatures start to rise again, subsidence patterns stabilize but still show significant deformation, particularly around the borehole. Compared to the results from April 2022, the settlement of both the silty layer and permafrost is greater in April 2023, indicating permafrost degradation.

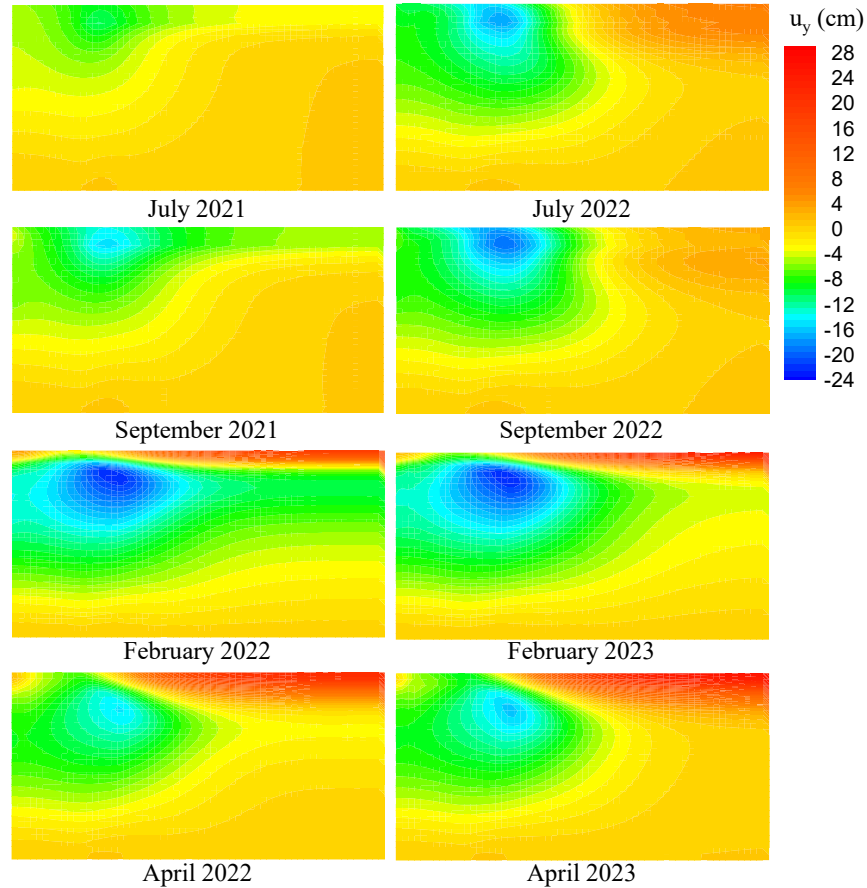
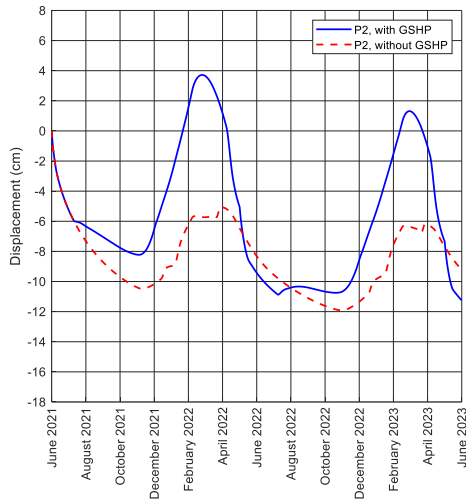


Figure 5-12 Ground subsidence contours over selected time frames within two years

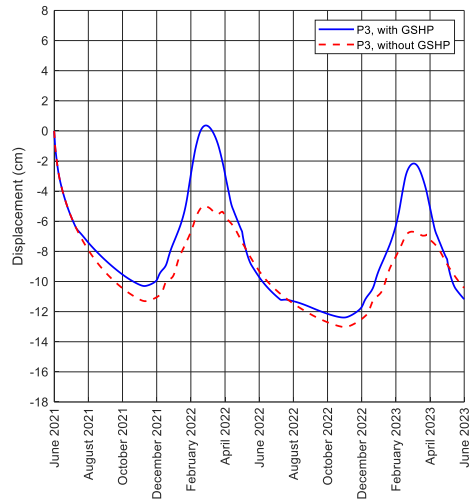
## 5.6 Discussions

### 5.6.1 Effect of GSHP operation on the ground subsidence

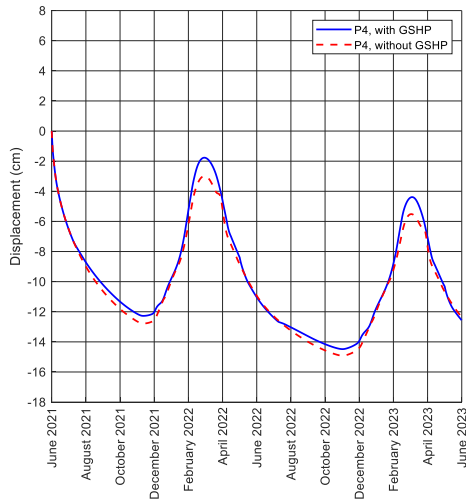
To analyze the impact of GSHP operation on ground subsidence, the results from the four monitoring points mentioned at 1.5 m, 3 m, 4.5 m, and 6 m (i.e., P2, P3, P4, and P5, respectively in Figure 5-7) are presented in Figure 5-13. Each graph shows the time series of ground displacement at the respective points. For comparison purposes, an additional simulation was conducted without the GSHP operation to assess the differences in displacements.



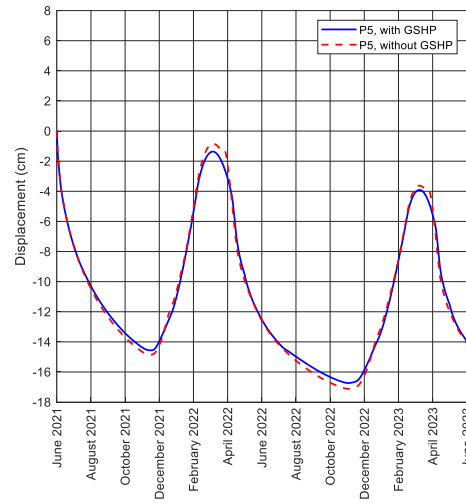
(a)



(b)



(c)



(d)

Figure 5-13 Displacement data for the three monitoring points: (a) P2, (b) P3, (c) P4, and (d) P5 over the two years, with and without GSHP operation.

Each graph compares ground deformation with and without the operation of the GSHP system. P2 and P3 (i.e., 1.5 m and 3 m from the borehole) display a similar trend. At P2 and P3, after the activation of the GSHP, the rate of subsidence is lower, showing more stable behavior compared to the case without GSHP. Additionally, during the cold season, the frost heave around the

borehole in the GSHP scenario shows a higher amplitude of deformation than in the scenario without GSHP. However, after the deactivation of the GSHP, a sudden settlement occurs because of thawing of ice around the borehole, which decrease the extent of deformation to even less than in the case without GSHP. A similar pattern emerges at P3 (3 m from the borehole), although the displacement is slightly lower than at P2. The GSHP's influence remains substantial, with larger deformations observed compared to the non-GSHP scenario.

At P4 (4.5 m from the borehole), the effects of GSHP are less pronounced but still noticeable. Both frost heave and subsidence occur with reduced magnitude. Finally, at P5 (6 m from the borehole), the displacement in both GSHP and non-GSHP scenarios becomes nearly identical, indicating that the influence of the GSHP diminishes significantly at this distance. The GSHP system's thermal influence weakens with distance, becoming negligible by 6 m (P5). These results suggest that increased subsidence and frost heave near the borehole must be considered in GSHP system designs, particularly for infrastructure planning, as deformation is localized within a few meters of the borehole.

To further understand the effect of GSHP operation on ground deformation, [Figure 5-14](#) compares the accumulated plastic strain in the model at the end of the simulation with and without GSHP operation. The results show a noticeable difference in plastic strain distribution, with higher values near the borehole when the GSHP is operating. This indicates that the GSHP system introduces additional mechanical stress, leading to increased plastic deformation in the surrounding ground. However, the maximum accumulated plastic strain in the permafrost region is slightly lower than in the case without GSHP operation.

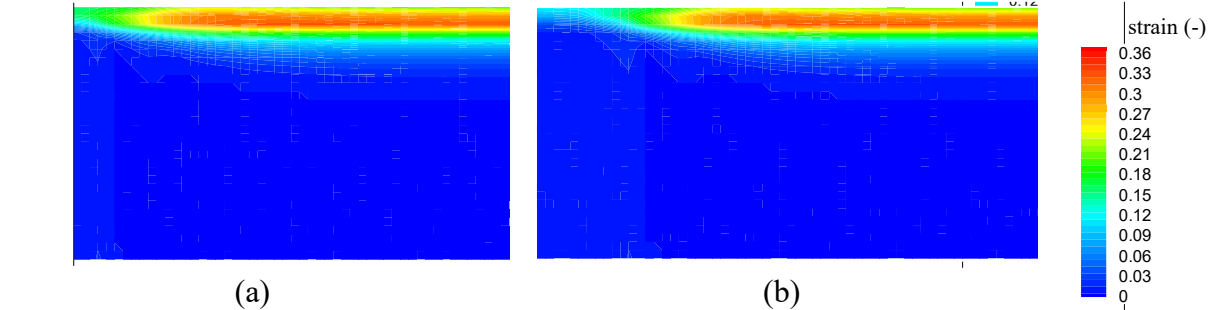


Figure 5-14 Comparison between the accumulated plastic strain of the model at the end of the simulation (a) with GSHP operation, and (b) without GSHP operation.

It can be concluded from [Figure 5-13](#) and [Figure 5-14](#) that while the GSHP system is effective in providing thermal regulation, it introduces additional mechanical stress on the ground around the borehole. Overall, this additional mechanical stress helps ground stability but when the GSHP is off, the rate of the ground subsidence will be more than the case without the application of GSHP. This highlights a trade-off between thermal management and ground stability. To mitigate these effects, it is necessary to optimize the GSHP operation parameters or consider supplementary ground stabilization measures to reduce subsidence, particularly in regions close to the borehole. By incorporating seasonal storage techniques and reinforcing the ground using grouting or thermal barriers, the risks of subsidence and frost heave can be significantly reduced. Monitoring systems and predictive modeling provide the data needed to maintain stable ground conditions and ensure the long-term sustainability of GSHP systems. Additionally, adjusting GSHP operations, as discussed in the next section, can also be useful.

### 5.6.2 Effect of GSHP running time on ground subsidence

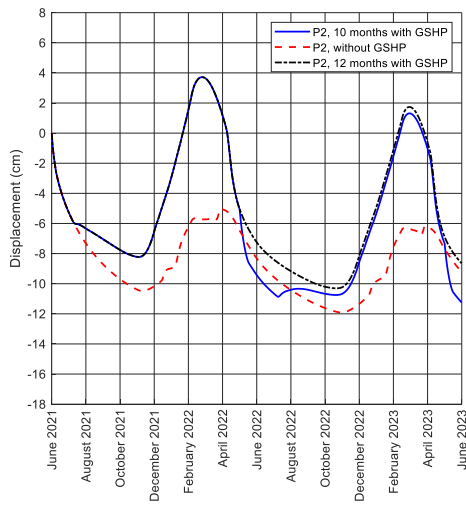
As described in the previous section, the GSHP system operates for 10 months from July to the end of May at a temperature of  $-5^{\circ}\text{C}$  and is turned off for the remaining 2 months. In this section, an alternative scenario is considered where the GSHP maintains a constant temperature of  $-5^{\circ}\text{C}$  throughout the entire year. The displacement data for the monitoring points P2, P3, P4, and P5

under this constant temperature scenario, compared to the original intermittent scenario, are presented in [Figure 5-15](#).

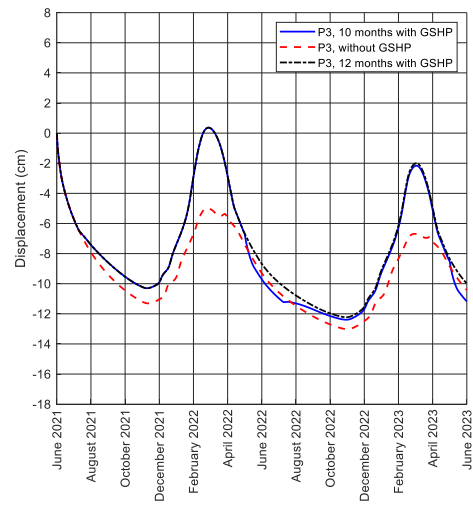
In the original scenario, where the GSHP operates for 10 months and is off for 2 months, the displacement follows a seasonal pattern. Significant subsidence occurs during the periods when the GSHP is off, as the ground experiences additional thawing during the warmer months. In contrast, the constant temperature scenario shows a more consistent and stable displacement pattern with reduced fluctuations in subsidence. This indicates that maintaining a year-round constant GSHP temperature helps mitigate extreme subsidence, leading to more stable ground conditions.

At P2 and P3, the closest points to the borehole, the effect of the constant temperature scenario is most noticeable, with the subsidence amplitude significantly reduced compared to the original scenario. The graphs reveal a smoother displacement curve, indicating that this approach can effectively stabilize the ground near the borehole by minimizing seasonal variations.

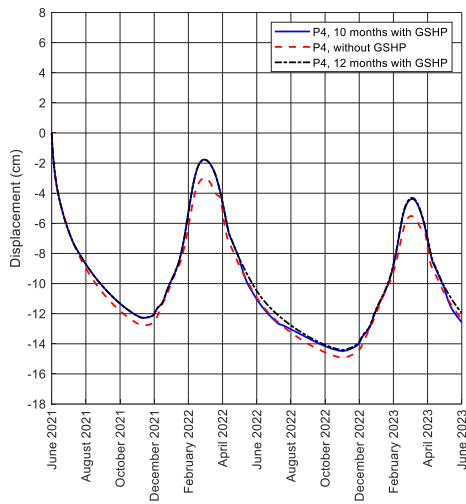
At P4 and P5 (4.5 m and 6 m from the borehole), the displacement patterns are less pronounced, as these points are further from the GSHP. Although the difference in subsidence amplitude between the constant temperature and original scenarios is less significant here, the constant temperature scenario still displays a reduction in subsidence. This supports the conclusion that maintaining a constant GSHP temperature can help reduce ground subsidence, particularly near the borehole, and could be an effective strategy for improving ground stability in permafrost regions by minimizing mechanical stresses induced by seasonal temperature changes.



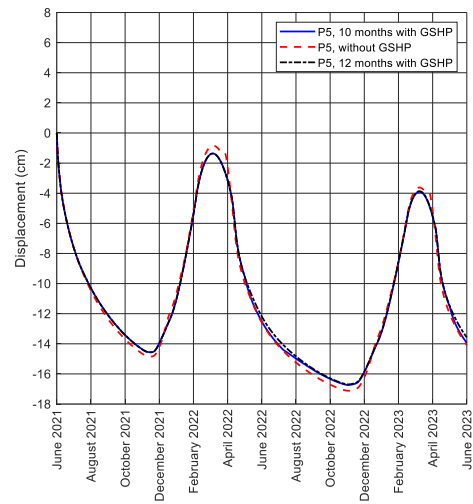
(a)



(b)



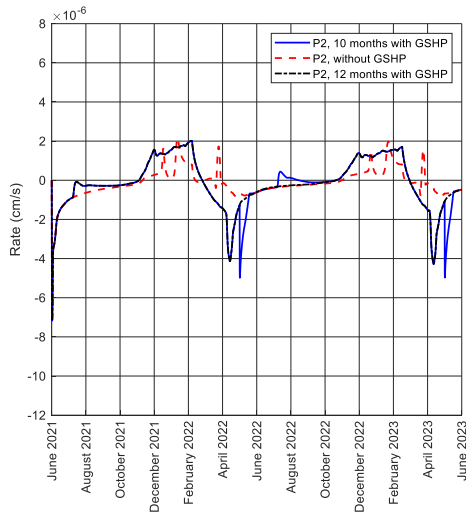
(c)



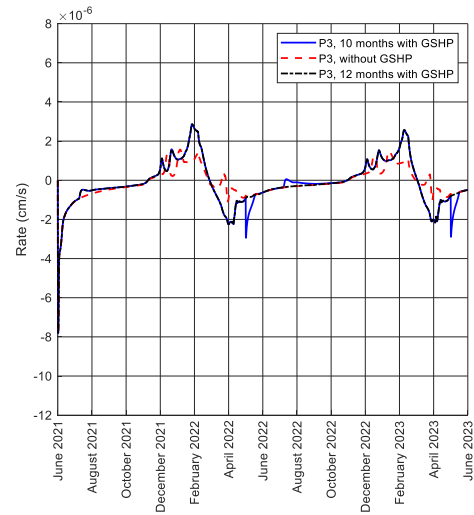
(d)

Figure 5-15 Displacement data for monitoring points: (a) P2, (b) P3, (c) P4, and (d) P5 over the two years under three scenarios: with GSHP operation for 10 months, without GSHP operation, and with GSHP temperature kept constant at  $-5^{\circ}\text{C}$ .

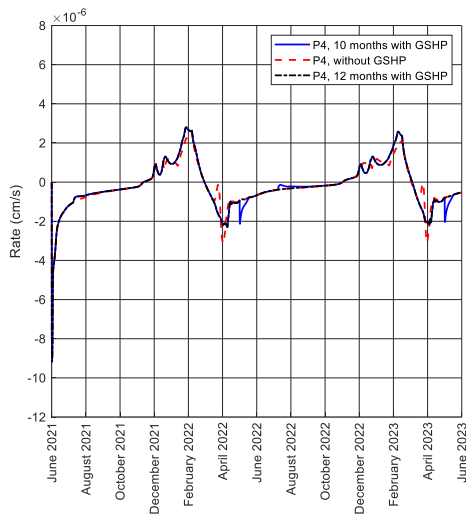
Additionally, [Figure 5-16](#) shows the rate of displacement in similar scenarios at the same monitoring points (i.e., P2, P3, P4, and P5, located at varying distances from the borehole: 1.5 m, 3 m, 4.5 m, and 6 m, respectively). The rate of displacement helps illustrate the intensity and timing of ground movements, particularly subsidence and frost heave, under different thermal regimes.



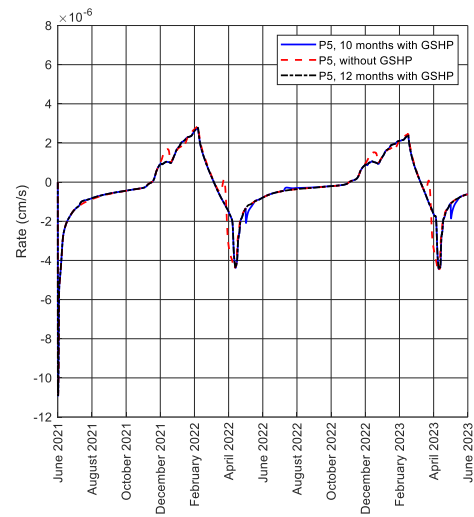
(a)



(b)



(c)



(d)

Figure 5-16 Simulated displacement rates at monitoring points: (a) P2, (b) P3, (c) P4, and (d) P5 over two years under three different scenarios.

The rate of displacement is highly sensitive to the operating schedule of the GSHP system, particularly at the points closest to the borehole (P2 and P3). The constant GSHP temperature scenario helps stabilize the ground, reducing extreme fluctuations in the rate of displacement compared to when the GSHP is turned off for part of the year. This steady operation minimizes rapid changes in subsidence and frost heave, thereby maintaining ground stability. Further from the borehole (P4 and P5), the influence of the GSHP system on the rate of displacement diminishes, with minimal differences between the scenarios.

Maintaining year-round operation of GSHP systems to mitigate subsidence fluctuations could provide significant benefits for subsurface stability in permafrost regions like Umiujaq. However, the feasibility of this approach, from both an energy demand and economic perspective, requires careful consideration of several factors, including energy needs, costs, system design, and environmental conditions. Therefore, year-round GSHP operation in Umiujaq requires a balanced approach to ensure both economic viability and long-term sustainability.

### 5.6.3 Limitations

While this study provides valuable insights into the effects of GSHP operation on ground subsidence in permafrost regions, several limitations should be noted:

- This study is based on the simulation of a single well. While this provides a focused analysis, it does not capture the complexities that might arise in a multi-well system. Multi-well systems introduce complex interactions that significantly impact long-term performance and environmental sustainability. These systems can lead to thermal interference, increased ground deformation, hydraulic changes, and cumulative permafrost degradation if not properly managed. By carefully considering well spacing, operational strategies, and environmental monitoring, the adverse cumulative effects of multiple GSHP systems can be minimized, ensuring more stable and sustainable use in permafrost regions.
- The current analysis is limited to a specific site in Umiujaq. Regional variations in soil composition, temperature profiles, and permafrost characteristics can significantly impact the results. Conducting a regional analysis would provide a more comprehensive understanding of the GSHP's impact across different permafrost environments.
- The ground structure in this study is relatively simplified, focusing on layers of silty sediment and permafrost. Real-world scenarios often involve more complex stratigraphy,

including varying soil types, bedrock features, and discontinuities. Incorporating a more detailed and realistic ground structure in future simulations would enhance the accuracy of the results. Frozen soils are considered as a non-homogenous material where the compounds are present with different volumetric ratio, which changes the mechanical and thermal properties of the medium. Ultimately, the model would need to account for these heterogeneities to provide more accurate and reliable results for infrastructure planning and the sustainable operation of GSHP systems. Recently, numerical methods like numerical homogenization are introduced to calculate the effective mechanical, hydraulic and thermal properties (Erkmen et al., 2020; Norouzi et al., 2022; Norouzi et al., 2024). Incorporating of these methods, the accuracy of the model can be elevated.

- While the study explored scenarios with constant GSHP temperatures and seasonal variations, it did not delve into the effects of more dynamic temperature management strategies. Investigating different temperature regulation techniques could help optimize GSHP operation for both thermal efficiency and ground stability.
- A Two-year simulation provides a snapshot of the seasonal and short-term impacts. However, long-term studies are essential to understand the cumulative effects of GSHP systems on permafrost and ground stability over decades. Extending the simulation period to longer time scales would likely reveal more pronounced cumulative effects, including increased plastic deformation, ground subsidence, and reduced GSHP efficiency due to climate change. Long-term permafrost degradation, driven by rising temperatures and more frequent thaw cycles, would compound the challenges of operating GSHP systems in cold regions.

The model parameters were primarily sourced from literature and previous studies. Calibration and validation against actual field data would increase the reliability of the simulation results. Field experiments and monitoring should be integrated into future studies to refine and validate the model predictions. The field measurements should be collected, focusing on the thermal, hydraulic, and mechanical properties of the permafrost and surrounding soils such as temperature profile, deformation measurements, porosity and permeability of the layers, soil moisture and ice content, and permafrost depth and active layer thickness. By obtaining these field measurements using instruments like thermistors, piezometers, TDR sensors, fiber optic sensing technology, and inclinometers, the model can be calibrated and validated more effectively, ensuring more accurate predictions of GSHP impacts in a permafrost environment (Li et al., 2024).

## 5.7 Conclusions

This study provides a foundational understanding of the thermal, hydraulic, and mechanical behaviors influenced by GSHP systems in cold climates, highlighting both the potential and the challenges of using geothermal energy in Arctic and subarctic environments. A two-dimensional plane strain fully coupled THM model based on the FEM was utilized to investigate the effects of thawing and freezing cycles around a GSHP in Umiujaq, northern Quebec, focusing on evaluating the ground subsidence during two years of operation. Here are the key conclusions:

- Key factors such as ice saturation, phase change strain, and pore pressure are quantified to provide comprehensive ground deformation results. Our in-house developed FEM numerical tool demonstrates the necessity and feasibility of modeling THM coupled ground responses associated with GSHP operations in permafrost regions. Validation of our numerical model against a laboratory freezing test confirms its effectiveness in

quantifying frost heave behavior. Thermally induced plastic deformation can be explicitly modeled using the temperature-dependent mechanical properties of frozen soils.

- Our approach integrates both poro-elastic (reversible) and poro-plastic (irreversible) responses. By including poro-plastic behavior, our model accounts for the permanent ground deformations that occur due to freeze-thaw cycles associated with GSHP operations in permafrost regions. Phase change strain (the strain caused by the freezing and thawing of water in the soil) is explicitly modeled. This adds a level of realism to the mechanical behavior of frozen ground, where the transition between ice and water causes both elastic and plastic deformations in the soil structure. Additionally, the inclusion of temperature-dependent mechanical properties in the stress-strain relationship provides a more detailed understanding of how frozen soil behaves under varying temperature conditions, allowing for more accurate simulations.
- Monitored air temperature data at the Umiujaq site shows significant fluctuations, with ambient temperatures contributing to permafrost thawing. Our study compared three different GSHP operation scenarios and concluded that to effectively control ground settlement, it is preferable to maintain GSHP operation year-round rather than shutting it down during the summer months. Our numerical results also quantify the potential plastic deformation in the ground surrounding the borehole due to GSHP operations.
- Future studies should consider models with multiple wells, which are more representative of typical GSHP installations, to understand the cumulative effects and interactions between wells. Also, incorporating regional analysis of mechanical properties can further improve the accuracy of the model. Additionally, models incorporating different layers and varied Soil-Freezing Characteristic Curves (SFCC) could provide deeper insights into the

application of GSHP systems in Arctic and subarctic regions. Finally, future work should incorporate climate projection data and develop adaptive strategies to ensure the sustainability of GSHP systems considering long-term environmental changes.

- While the study focuses on the mechanical impacts of GSHP systems, the potential ecological impacts of altering the thermal regime of permafrost are significant, particularly those that arise from altering the thermal regime of the permafrost. Changes in ground temperature, permafrost degradation, and subsurface water flow can have significant ecological consequences, including effects on local hydrology and vegetation patterns. These impacts include changes to local hydrology, vegetation patterns, and wildlife habitats, as well as broader implications for greenhouse gas emissions and soil stability. To fully understand and manage the consequences of GSHP operations in permafrost regions, future studies should consider these ecological factors alongside the mechanical effects, incorporating field measurements, ecosystem monitoring, and predictive modeling to mitigate potential risks to the environment.

As GSHP systems offer significant potential for sustainable energy development in permafrost regions, they must be carefully designed, monitored, and managed to prevent adverse impacts on ground stability, local hydrology, and ecosystems. By incorporating site-specific assessments, monitoring systems, and adaptive management strategies, policymakers and engineers can ensure that GSHP systems contribute to long-term sustainable energy development without causing significant harm to the sensitive permafrost environment. These recommendations build on careful design, real-time monitoring, environmental protection, and climate resilience that can form the foundation of best practices for GSHP deployment in Arctic and subarctic regions, ensuring both energy efficiency and environmental sustainability in these fragile ecosystems.

## Chapter 6

# 6 Conclusions, limitations, and recommendations for future work

## 6.1 Conclusion

This thesis has explored various aspects of soil mechanics and thermal-hydro-mechanical (THM) interactions in frozen and freezing soils. Through detailed numerical simulations and computational models, several key findings have been identified:

### 6.1.1 Estimating Equivalent Elastic Properties of Frozen Clay Soils Using an XFEM-Based Computational Homogenization (Chapter 3):

- The XFEM-based numerical homogenization approach provides a reliable method to estimate the elastic properties of frozen clay soils, particularly by considering the imperfect bonds between clay-water composites and nonclay minerals. The results highlight the critical impact of inclusion volume fraction on the accuracy of elastic property estimation.
- The study showed that when the volume fraction of clay-water composites exceeds 0.7, the estimated elastic properties are reliable. For lower volume fractions, the reliability decreases, emphasizing the need for careful consideration of the composite's volumetric content in practical applications.
- The calibrated interface stiffness parameter, essential for accurate predictions, increases as temperature decreases, mirroring the behavior of the elastic modulus. This insight is crucial for understanding the mechanical behavior of frozen soils under varying thermal conditions.

### **6.1.2 Finite Element Modeling of Thermal-Hydro-Mechanical Coupled Processes in Unsaturated Freezing Soils Considering Air-Water Capillary Pressure and Cryosuction (Chapter 4):**

- A comprehensive finite element model has been developed to simulate the complex interactions between thermal, hydraulic, and mechanical processes in unsaturated freezing soils. The study successfully validated the model against experimental data and underscored the importance of considering phase change-induced strain and total pore pressure components in predicting soil behavior under frost conditions.
- The introduction of a new soil freezing characteristic curve (SFCC) model, combining the van Genuchten soil water characteristic curve and the Clapeyron equation, allows for a more accurate representation of the suctions from air-water capillary pressure and water-ice cryosuction.
- The research demonstrated that neglecting phase change-induced strain leads to inaccurate frost heave predictions. Incorporating this factor is essential for realistic modeling of unsaturated soils under freeze-thaw cycles.

### **6.1.3 Numerical Evaluation of Using Ground Source Heat Pump for Renewable Energy Generation and Climate Adaptation in a Thawing Permafrost Region (Chapter 5):**

- The use of Ground Source Heat Pump (GSHP) systems can mitigate ground subsidence in permafrost regions, particularly when operated throughout the year. However, the mechanical stresses induced by GSHP operation necessitate careful design and ongoing monitoring to ensure ground stability.
- The study revealed that maintaining GSHP operation throughout the year, rather than only during winter months, helps in stabilizing the subsurface environment and mitigating extreme subsidence fluctuations.
- While GSHP systems offer effective thermal regulation, they introduce mechanical stresses that can disturb the ground. Therefore, balancing the thermal benefits with ground stability is crucial for the successful implementation of GSHP systems in permafrost regions.

## **6.2 Limitations**

Despite the valuable insights provided by this research, several limitations must be acknowledged:

### **6.2.1 Simplified Models:**

The models developed in this thesis often rely on simplified representations of soil structures and conditions. For instance, the single-well scenario in Chapter 5 does not capture the complexities of multi-well systems or the full range of soil stratigraphy found in real-world environments. Realistic modeling would benefit from incorporating detailed geological features and multi-well interactions.

### **6.2.2 Scope of Validation:**

While the models have been validated against available experimental data, the scope of validation is limited. The absence of validation against data with explicit plastic deformation records (Chapter 4) and the reliance on literature-sourced parameters (Chapter 5) highlight areas where further empirical validation is necessary. Validation with comprehensive experimental datasets would enhance the reliability and applicability of the models.

### **6.2.3 Geographical and Temporal Constraints:**

The site-specific focus, particularly in Chapter 5, means the findings may not be directly applicable to other permafrost regions with different soil compositions and environmental conditions. Additionally, the simulations cover relatively short periods (e.g., two years), which may not fully capture long-term effects. Long-term studies across various geographical locations are essential to generalize the findings.

## **6.3 Recommendations for Future Work**

To address the limitations and build upon the findings of this thesis, the following recommendations for future research are proposed:

### **6.3.1 Enhanced Model Complexity:**

Future studies should incorporate more complex soil structures and multi-well systems to better reflect real-world conditions. Including detailed stratigraphy and varying soil types will improve the accuracy and applicability of the models. Additionally, considering the interactions between multiple wells and the cumulative effects of GSHP systems will provide a more comprehensive understanding of their impact.

### **6.3.2 Broader Validation Efforts:**

Extensive validation against a wider range of experimental data, including those with explicit records of plastic deformation and long-term monitoring, is essential. Field experiments and site-specific data collection should be integrated into future research efforts to refine model predictions. This includes in-situ measurements of soil properties and environmental conditions to validate and calibrate the models.

### **6.3.3 Exploration of Dynamic Temperature Management:**

Investigating dynamic temperature management strategies for GSHP systems could optimize their operation for both thermal efficiency and ground stability. This includes exploring seasonal and more nuanced temperature regulation techniques, such as variable temperature settings and adaptive control systems, to enhance the performance and reduce the mechanical stresses on the ground.

### **6.3.4 Regional and Long-Term Studies:**

Conducting regional analyses and long-term studies will provide a more comprehensive understanding of the impacts of GSHP systems and other interventions across different permafrost environments and over extended periods. This will help in developing sustainable and resilient

solutions for climate adaptation. Long-term monitoring and modeling of soil behavior under changing climatic conditions are crucial for predicting future trends and mitigating potential risks.

### **6.3.5 Interfacial and Micromechanical Investigations:**

Further research should focus on the interfacial aspects between frozen and unfrozen soil parts, particularly in relation to ice lens generation and micromechanical failure processes. Techniques like the eXtended Finite Element Method (XFEM) can be applied to characterize these complex interactions more accurately. Understanding the micromechanical behavior of soil-ice interfaces and the formation of ice lenses will enhance the predictive capability of the models.

### **6.3.6 Integration of Field Data:**

Incorporating real-time field data into numerical models will enhance their predictive accuracy and reliability. Continuous monitoring of temperature, moisture content, and ground deformation in permafrost regions can provide valuable insights for model calibration and validation. Developing robust data assimilation techniques to integrate field measurements with model simulations will improve the overall understanding of frozen soil mechanics.

### **6.3.7 Development of User-Friendly Simulation Tools:**

Creating user-friendly simulation tools and software based on the developed models can facilitate their application in engineering practice. These tools should be accessible to engineers and researchers, allowing them to easily input site-specific data, run simulations, and interpret the results. Providing comprehensive documentation and training materials will further enhance the usability and adoption of these tools in the field.

By addressing these recommendations, future research can enhance our understanding of frozen soil mechanics, improve predictive models, and contribute to the development of effective

engineering solutions in cold regions. The advancements in modeling techniques and practical applications will ultimately support the sustainable and resilient development of infrastructure in permafrost-affected areas.

## Bibliography

- An, R., Zhang, X., Wang, Y., Liu, X., Chen, C., Gong, J., 2022. Freeze–thaw impact on sandy clay in artificial frozen walls: An investigation of shear strength and pore-size distribution. *Int. J. Geomech.* 22, 04022230.
- Andersland, O.B., Ladanyi, B., 2013. *An Introduction to Frozen Ground Engineering*. Springer; 1994th edition (Aug. 21 2013).
- Andersland, O.B., Ladanyi, B., 2003. *Frozen ground engineering*. John Wiley & Sons.
- Arzanfudi, M.M., Al-Khoury, R., 2018. Freezing-thawing of porous media: An extended finite element approach for soil freezing and thawing. *Adv. Water Resour.* 119, 210–226.  
<https://doi.org/10.1016/j.advwatres.2018.07.013>
- Baba, F.M., Ge, H., Wang, L.L., Zmeureanu, R., 2022. Do high energy-efficient buildings increase overheating risk in cold climates? Causes and mitigation measures required under recent and future climates. *Build. Environ.* 219, 109230.
- Bai, R., Lai, Y., Pei, W., Zhang, M., 2020. Investigation on frost heave of saturated–unsaturated soils. *Acta Geotech.* 15, 3295–3306.
- Baser, T., McCartney, J.S., 2015. Development of a full-scale soil-borehole thermal energy storage system, in: *IFCEE 2015*. pp. 1608–1617.

- Bekele, Y.W., Kyokawa, H., Kvarving, A.M., Kvamsdal, T., Nordal, S., 2017. Isogeometric analysis of THM coupled processes in ground freezing. *Comput. Geotech.* 88, 129–145.
- Bi, J., Wang, G., Wu, Z., Wen, H., Zhang, Y., Lin, G., Sun, T., 2023. Investigation on unfrozen water content models of freezing soils. *Front. Earth Sci.* 10, 1039330.
- Bidarmaghz, A., Narsilio, G.A., Johnston, I.W., Colls, S., 2016. The importance of surface air temperature fluctuations on long-term performance of vertical ground heat exchangers. *Geomech. Energy Environ.* 6, 35–44.
- Brooks, A.N., Hughes, T.J.R., 1982. Streamline upwind/Petrov-Galerkin formulations for convection dominated flows with particular emphasis on the incompressible Navier-Stokes equations. *Comput. Methods Appl. Mech. Eng.* 32, 199–259.
- Catolico, N., Ge, S., McCartney, J.S., 2016. Numerical Modeling of a Soil-Borehole Thermal Energy Storage System. *Vadose Zo. J.* 15, 1–17.
- Chang, D., Lai, Y., Zhang, M., 2019. A meso-macroscopic constitutive model of frozen saline sandy soil based on homogenization theory. *Int. J. Mech. Sci.* 159, 246–259.
- Chen, X., Jeong, S., 2024. Asymmetric impacts of surface thaw onset change on seasonal vegetation growth in Arctic permafrost. *Glob. Ecol. Biogeogr.* 33, 131–140.
- Chen, Y., Lai, Y., Li, H., Pei, W., 2022. Finite element analysis of heat and mass transfer in unsaturated freezing soils: Formulation and verification. *Comput. Geotech.* 149, 104848.
- Cleary, M.P., Lee, S.-M., Chen, I.-W., 1980. Self-consistent techniques for heterogeneous media. *J. Eng. Mech. Div.* 106, 861–887.

- Dagenais, S., Molson, J., Lemieux, J.-M., Fortier, R., Therrien, R., 2020. Coupled cryo-hydrogeological modelling of permafrost dynamics near Umiujaq (Nunavik, Canada). *Hydrogeol. J.* 28, 887–904.
- Dall’Amico, M., Endrizzi, S., Gruber, S., Rigon, R., 2011. A robust and energy-conserving model of freezing variably-saturated soil. *Cryosph.* 5, 469–484.
- de Souza Neto, E.A., Peric, D., Owen, D.R.J., 2011. *Computational methods for plasticity: theory and applications*. John Wiley & Sons.
- Diersch, H.-J., Bauer, D., Heidemann, W., Rühaak, W., Schätzl, P., 2011. Finite element modeling of borehole heat exchanger systems: Part 1. Fundamentals. *Comput. Geosci.* 37, 1122–1135.
- Drucker, D.C., Prager, W., 1952. Soil mechanics and plastic analysis or limit design. *Q. Appl. Math.* 10, 157–165.
- Erkmen, E., Dias-da-Costa, D., 2022. Alleviation of the Oscillatory Traction in the Extended Finite Element Method, in: *Canadian Society of Civil Engineering Annual Conference*. Springer, pp. 715–731.
- Erkmen, E., Malek, S., Ayranci, C., 2020. An XFEM-based computational homogenization framework for thermal conductivity evaluation of composites with imperfectly bonded inclusions. *Eng. Res. Express*.
- Erkmen, R.E., Dias-da-Costa, D., 2021. Stabilization of the extended finite element method for stiff embedded interfaces and inclusions. *Int. J. Numer. Methods Eng.* 122, 7378–7408.

- Fortier, R., LeBlanc, A.-M., Yu, W., 2011. Impacts of permafrost degradation on a road embankment at Umiujaq in Nunavik (Quebec), Canada. *Can. Geotech. J.* 48, 720–740.
- Fu, H., Song, E., Tong, R., 2023. Numerical simulation of frost heave of saturated soil considering thermo-hydro-mechanical coupling. *Int. J. Numer. Anal. Methods Geomech.* 48, 3–27.
- Fukuda, M., KIM, H.-S., KIM, Y.-C., 1997. Preliminary results of frost heave experiments using standard test sample provided by TC8, in: *Ground Freezing 97: Frost Action in Soils*. pp. 25–30.
- Gawin, D., Pesavento, F., Koniorczyk, M., Schrefler, B.A., 2020. Poro-mechanical model of strain hysteresis due to cyclic water freezing in partially saturated porous media. *Int. J. Solids Struct.* 206, 322–339.
- Gawin, D., Pesavento, F., Koniorczyk, M., Schrefler, B.A., 2019. Non-equilibrium modeling hysteresis of water freezing: Ice thawing in partially saturated porous building materials. *J. Build. Phys.* 43, 61–98.
- Geers, Marc G D, Kouznetsova, V.G., Brekelmans, W.A.M., 2010. Multi-scale computational homogenization: Trends and challenges. *J. Comput. Appl. Math.* 234, 2175–2182.
- Geers, M. G.D., Kouznetsova, V.G., Brekelmans, W.A.M., 2010. Computational homogenization, in: *CISM International Centre for Mechanical Sciences, Courses and Lectures*. Springer, pp. 327–394. [https://doi.org/10.1007/978-3-7091-0283-1\\_7](https://doi.org/10.1007/978-3-7091-0283-1_7)
- Gheysari, A.F., Holländer, H.M., Maghoul, P., Shalaby, A., 2021. Sustainability, climate

- resiliency, and mitigation capacity of geothermal heat pump systems in cold regions. *Geothermics* 91, 101979. [https://doi.org/https://doi.org/10.1016/j.geothermics.2020.101979](https://doi.org/10.1016/j.geothermics.2020.101979)
- Giordano, N., Raymond, J., 2019. Alternative and sustainable heat production for drinking water needs in a subarctic climate (Nunavik, Canada): Borehole thermal energy storage to reduce fossil fuel dependency in off-grid communities. *Appl. Energy* 252, 113463.
- Giordano, N., Riggi, L., Della Valentina, S., Casasso, A., Mandrone, G., Raymond, J., 2019. Efficiency evaluation of borehole heat exchangers in Nunavik, Québec, Canada. 1511637 2019, 4381–4388.
- Girgis, N., 2019. Experimental investigations on temperature-dependent mechanical properties of artificially frozen sandy clay soils. Concordia University.
- Girgis, N., Li, B., Akhtar, S., Courcelles, B., 2020. Experimental study of rate-dependent uniaxial compressive behaviors of two artificial frozen sandy clay soils. *Cold Reg. Sci. Technol.* 180, 103166. <https://doi.org/10.1016/j.coldregions.2020.103166>
- Goudarzi, M., Mohammadi, S., 2015. Analysis of cohesive cracking in saturated porous media using an extrinsically enriched EFG method. *Comput. Geotech.* 63, 183–198.
- Gruber, S., Haeberli, W., 2007. Permafrost in steep bedrock slopes and its temperature-related destabilization following climate change. *J. Geophys. Res. Earth Surf.* 112.
- Gunawan, E., Giordano, N., Jensson, P., Newson, J., Raymond, J., 2020. Alternative heating systems for northern remote communities: Techno-economic analysis of ground-coupled heat pumps in Kuujuaq, Nunavik, Canada. *Renew. Energy* 147, 1540–1553.

- Hansson, K., Šimůnek, J., Mizoguchi, M., Lundin, L., Van Genuchten, M.T., 2004. Water flow and heat transport in frozen soil: Numerical solution and freeze–thaw applications. *Vadose Zo. J.* 3, 693–704.
- Hassani, B., Hinton, E., 1998. A review of homogenization and topology optimization I - Homogenization theory for media with periodic structure. *Comput. Struct.* 69, 707–717. [https://doi.org/10.1016/S0045-7949\(98\)00131-X](https://doi.org/10.1016/S0045-7949(98)00131-X)
- He, Z., Teng, J., Yang, Z., Liang, L., Li, H., Zhang, S., 2020. An analysis of vapour transfer in unsaturated freezing soils. *Cold Reg. Sci. Technol.* 169, 102914.
- Hjort, J., Karjalainen, O., Aalto, J., Westermann, S., Romanovsky, V.E., Nelson, F.E., Etzelmüller, B., Luoto, M., 2018. Degrading permafrost puts Arctic infrastructure at risk by mid-century. *Nat. Commun.* 9, 5147.
- Hjort, J., Streletskiy, D., Doré, G., Wu, Q., Bjella, K., Luoto, M., 2022. Impacts of permafrost degradation on infrastructure. *Nat. Rev. Earth Environ.* 3, 24–38.
- Huang, X., Rudolph, D.L., 2021. Coupled model for water, vapour, heat, stress and strain fields in variably saturated freezing soils. *Adv. Water Resour.* 154, 103945.
- Jame, Y., Norum, D.I., 1980. Heat and mass transfer in a freezing unsaturated porous medium. *Water Resour. Res.* 16, 811–819.
- Jiang, J., Wang, F., Yang, X., Zhang, Y., Deng, J., Wei, Q., Cai, W., Chen, C., 2022. Evaluation of the long-term performance of the deep U-type borehole heat exchanger on different geological parameters using the Taguchi method. *J. Build. Eng.* 59, 105122.

- Jolivel, M., Allard, M., 2013. Thermokarst and export of sediment and organic carbon in the Sheldrake River watershed, Nunavik, Canada. *J. Geophys. Res. Earth Surf.* 118, 1729–1745.
- Kadivar, M., Manahiloh, K.N., 2019. Revisiting parameters that dictate the mechanical behavior of frozen soils. *Cold Reg. Sci. Technol.* 163, 34–43.  
<https://doi.org/https://doi.org/10.1016/j.coldregions.2019.04.005>
- Kay, B.D., Groenevelt, P.H., 1974. On the interaction of water and heat transport in frozen and unfrozen soils: I. Basic theory; the vapor phase. *Soil Sci. Soc. Am. J.* 38, 395–400.
- Kebria, M.M., Na, S., 2024. A coupled phase-field method (PFM) and thermo-hydro-mechanics (THM) based framework for analyzing saturated ice-rich porous materials. *Int. J. Numer. Anal. Methods Geomech.*
- Kelly, D.W., Nakazawa, S., Zienkiewicz, O.C., Heinrich, J., 1980. A note on upwinding and anisotropic balancing dissipation in finite element approximations to convective diffusion problems. *Int. J. Numer. Methods Eng.* 15, 1705–1711.
- Keuper, F., Dorrepaal, E., van Bodegom, P.M., van Logtestijn, R., Venhuizen, G., van Hal, J., Aerts, R., 2017. Experimentally increased nutrient availability at the permafrost thaw front selectively enhances biomass production of deep-rooting subarctic peatland species. *Glob. Chang. Biol.* 23, 4257–4266.
- Keuper, F., van Bodegom, P.M., Dorrepaal, E., Weedon, J.T., van Hal, J., van Logtestijn, R.S.P., Aerts, R., 2012. A frozen feast: Thawing permafrost increases plant-available nitrogen in subarctic peatlands. *Glob. Chang. Biol.* 18, 1998–2007.

- Khoei, A.R., Amini, D., Mortazavi, S.M.S., 2021. Modeling non-isothermal two-phase fluid flow with phase change in deformable fractured porous media using extended finite element method. *Int. J. Numer. Methods Eng.* 122, 4378–4426.
- Khoei, A.R., Mortazavi, S.M.S., 2020. Thermo-hydro-mechanical modeling of fracturing porous media with two-phase fluid flow using X-FEM technique. *Int. J. Numer. Anal. Methods Geomech.* 44, 2430–2472.
- Koniorczyk, M., Gawin, D., Schrefler, B.A., 2015. Modeling evolution of frost damage in fully saturated porous materials exposed to variable hygro-thermal conditions. *Comput. Methods Appl. Mech. Eng.* 297, 38–61.
- Kurylyk, B.L., Watanabe, K., 2013. The mathematical representation of freezing and thawing processes in variably-saturated, non-deformable soils. *Adv. Water Resour.* 60, 160–177.
- Langevin, H., Giordano, N., Raymond, J., Gosselin, L., Bourbonnais, M., 2024. Geothermal heat pumps to reduce diesel consumption in an off-grid subarctic community: Comparison of solar assisted systems with optional underground energy storage. *Geothermics* 116, 102846.
- Lewis, R.W., Schrefler, B.A., 1998. *The finite element method in the static and dynamic deformation and consolidation of porous media.* John Wiley & Sons.
- Li, B., Akhtar, S., 2022. Characterizations of tensile yield and failure processes of frozen clay soils: laboratory testing and numerical modeling. *Bull. Eng. Geol. Environ.* 81, 429.  
<https://doi.org/10.1007/s10064-022-02942-2>
- Li, B., Norouzi, E., Zhu, H.-H., Wu, B., 2024. A thermo-poromechanical model for simulating

- freeze–thaw actions in unsaturated soils. *Adv. Water Resour.* 184, 104624.
- Li, B., Wong, R.C.K., 2017. Modeling anisotropic static elastic properties of soft mudrocks with different clay fractions. *Geophysics* 82, MR27–MR37. <https://doi.org/10.1190/GEO2015-0575.1>
- Li, B., Wong, R.C.K., 2016. Quantifying structural states of soft mudrocks. *J. Geophys. Res. Solid Earth* 121, 3324–3347.
- Li, H., Zhu, Y., Zhang, J., Lin, C., 2004. Effects of temperature, strain rate and dry density on compressive strength of saturated frozen clay. *Cold Reg. Sci. Technol.* 39, 39–45.
- Li, W., Li, X., Wang, Y., Tu, J., 2018. An integrated predictive model of the long-term performance of ground source heat pump (GSHP) systems. *Energy Build.* 159, 309–318.
- Li, Z., Chen, J., Tang, A., Sugimoto, M., 2021. A novel model of heat-water-air-stress coupling in unsaturated frozen soil. *Int. J. Heat Mass Transf.* 175, 121375.
- Liu, B., Wang, J., Li, H., Liu, J., Wang, P., Cai, W., Sun, X., Chen, C., 2024. In-situ test and numerical investigation on the long-term performance of deep borehole heat exchanger coupled heat pump heating system. *Case Stud. Therm. Eng.* 61, 104855.
- Liu, Z., Yu, X., 2011. Coupled thermo-hydro-mechanical model for porous materials under frost action: theory and implementation. *Acta Geotech.* 6, 51–65. <https://doi.org/10.1007/s11440-011-0135-6>
- Ma, D., Ma, Q., Yuan, P., 2017. SHPB tests and dynamic constitutive model of artificial frozen sandy clay under confining pressure and temperature state. *Cold Reg. Sci. Technol.* 136,

37–43.

Ma, J., Huang, K., Zou, B., Li, X., Deng, Y., 2023. The influence of tunnel insulation measures on the temperature spatiotemporal variation of frozen soil during artificial ground freezing. *Cold Reg. Sci. Technol.* 103942.

Maghrabie, H.M., Abdeltwab, M.M., Tawfik, M.H.M., 2023. Ground-source heat pumps (GSHPs): Materials, models, applications, and sustainability. *Energy Build.* 113560.

Maranghi, F., Gosselin, L., Raymond, J., Bourbonnais, M., 2023. Modeling of solar-assisted ground-coupled heat pumps with or without batteries in remote high north communities. *Renew. Energy* 207, 484–498.

Markov, G., Mukerji, T., Dvorkin, J., 2009. *The rock physics handbook.*

Meng, Q., Wang, H., Cai, M., Xu, W., Zhuang, X., Rabczuk, T., 2020. Three-dimensional mesoscale computational modeling of soil-rock mixtures with concave particles. *Eng. Geol.* 277, 105802. <https://doi.org/10.1016/j.enggeo.2020.105802>

Meng, Q.X., Wang, H.L., Xu, W.Y., Cai, M., 2018. A numerical homogenization study of the elastic property of a soil-rock mixture using random mesostructure generation. *Comput. Geotech.* 98, 48–57. <https://doi.org/10.1016/j.compgeo.2018.01.015>

Michalowski, R.L., Zhu, M., 2006. Frost heave modelling using porosity rate function. *Int. J. Numer. Anal. methods Geomech.* 30, 703–722.

Mikkola, M., Hartikainen, J., 2001. Mathematical model of soil freezing and its numerical implementation. *Int. J. Numer. Methods Eng.* 52, 543–557.

- Milenić, D., Vasiljević, P., Vranješ, A., 2010. Criteria for use of groundwater as renewable energy source in geothermal heat pump systems for building heating/cooling purposes. *Energy Build.* 42, 649–657.
- Miner, K.R., Turetsky, M.R., Malina, E., Bartsch, A., Tamminen, J., McGuire, A.D., Fix, A., Sweeney, C., Elder, C.D., Miller, C.E., 2022. Permafrost carbon emissions in a changing Arctic. *Nat. Rev. Earth Environ.* 3, 55–67.
- Minsley, B.J., Pastick, N.J., James, S.R., Brown, D.R.N., Wylie, B.K., Kass, M.A., Romanovsky, V.E., 2022. Rapid and gradual permafrost thaw: A tale of two sites. *Geophys. Res. Lett.* 49, e2022GL100285.
- Mizoguchi, M., 1990. Water, heat and salt transport in freezing soil. Univ. Tokyo, Tokyo.
- Moradi, A., Smits, K.M., Massey, J., Cihan, A., McCartney, J., 2015. Impact of coupled heat transfer and water flow on soil borehole thermal energy storage (SBTES) systems: Experimental and modeling investigation. *Geothermics* 57, 56–72.
- Moran, M.J., Shapiro, H.N., Boettner, D.D., Bailey, M.B., 2010. Fundamentals of engineering thermodynamics. John Wiley & Sons.
- Moreno, D., Raymond, J., Comeau, F.-A., Gosselin, L., 2022. Life cycle cost analysis of heating system alternatives for residential buildings in subarctic climate (Nunavik, Canada). *GRC Trans.* 46, 2005–2028.
- Mortazavi, S.M.S., Beydokhti, O.R., Khoei, A.R., 2023. Modeling enhanced geothermal systems using a hybrid XFEM–ECM technique. *Appl. Therm. Eng.* 230, 120755.

- Na, S.H., Sun, W.C., 2017. Computational thermo-hydro-mechanics for multiphase freezing and thawing porous media in the finite deformation range. *Comput. Methods Appl. Mech. Eng.* 318, 667–700. <https://doi.org/10.1016/j.cma.2017.01.028>
- Nguyen, T.N., Erkmen, R.E., Sanchez, L.F.M., Li, J., 2020. Stiffness Degradation of Concrete Due to Alkali-Silica Reaction: A Computational Homogenization Approach. *Mater. J.* 117, 65–76.
- Nishimura, S., Gens, A., Olivella, S., Jardine, R.J., 2009. Thm-coupled finite element analysis of frozen soil: Formulation and application. *Geotechnique* 59, 159–171. <https://doi.org/10.1680/geot.2009.59.3.159>
- Norouzi, E., Li, B., 2024. Finite element modeling of thermal-hydro-mechanical coupled processes in unsaturated freezing soils considering air-water capillary pressure and cryosuction. *Int. J. Numer. Anal. Methods Geomech.* 48, 2944–2970.
- Norouzi, E., Li, B., Erkmen, R.E., 2024. Estimating equivalent elastic properties of frozen clay soils using an XFEM-based computational homogenization. *Cold Reg. Sci. Technol.* 226, 104292. <https://doi.org/https://doi.org/10.1016/j.coldregions.2024.104292>
- Norouzi, Emad, Li, B., Erkmen, R.E., 2022. Modelling equivalent elastic properties of imperfectly bonded soil-rock mixtures using an XFEM-based computational homogenization. *Comput. Geotech.* 144, 104638.
- Norouzi, E, Li, B., Raymond, J., 2022. Numerical modeling of thermo-hydro-mechanical processes related to geothermal heat pump operations in a subarctic climate, in: *ARMA US Rock Mechanics/Geomechanics Symposium*. ARMA, p. ARMA-2022.

- Norouzi, E., Moslemzadeh, H., Mohammadi, S., 2019. Maximum entropy based finite element analysis of porous media. *Front. Struct. Civ. Eng.* 13, 364–379.
- Norris, A.N., Callegari, A.J., Sheng, P., 1985. A generalized differential effective medium theory. *J. Mech. Phys. Solids* 33, 525–543.
- Otero, F., Oller, S., Martinez, X., 2018. Multiscale computational homogenization: review and proposal of a new enhanced-first-order method. *Arch. Comput. Methods Eng.* 25, 479–505.
- Ozgener, O., Hepbasli, A., 2007. Modeling and performance evaluation of ground source (geothermal) heat pump systems. *Energy Build.* 39, 66–75.
- Painter, S.L., 2011. Three-phase numerical model of water migration in partially frozen geological media: model formulation, validation, and applications. *Comput. Geosci.* 15, 69–85.
- Painter, S.L., Karra, S., 2014. Constitutive model for unfrozen water content in subfreezing unsaturated soils. *Vadose Zo. J.* 13, 1–8.
- Peng, Z., Tian, F., Wu, J., Huang, J., Hu, H., Darnault, C.J.G., 2016. A numerical model for water and heat transport in freezing soils with nonequilibrium ice-water interfaces. *Water Resour. Res.* 52, 7366–7381.
- Perreault, J., Fortier, R., Molson, J.W., 2021. Numerical modelling of permafrost dynamics under climate change and evolving ground surface conditions: application to an instrumented permafrost mound at Umiujaq, Nunavik (Québec), Canada. *Écoscience* 28, 377–397.

- Qaidi, S.M.A., Tayeh, B.A., Zeyad, A.M., de Azevedo, A.R.G., Ahmed, H.U., Emad, W., 2022. Recycling of mine tailings for the geopolymers production: A systematic review. *Case Stud. Constr. Mater.* 16, e00933. <https://doi.org/https://doi.org/10.1016/j.cscm.2022.e00933>
- Rad, F.M., Fung, A.S., Leong, W.H., 2013. Feasibility of combined solar thermal and ground source heat pump systems in cold climate, Canada. *Energy Build.* 61, 224–232.
- Sanei, M., Devloo, P.R.B., Forti, T.L.D., Durán, O., Santos, E.S.R., 2022. An innovative scheme to make an initial guess for iterative optimization methods to calibrate material parameters of strain-hardening elastoplastic models. *Rock Mech. Rock Eng.* 1–23.
- Sarbu, I., Sebarchievici, C., 2014. General review of ground-source heat pump systems for heating and cooling of buildings. *Energy Build.* 70, 441–454.
- Semnani, S.J., White, J.A., Borja, R.I., 2016. Thermoplasticity and strain localization in transversely isotropic materials based on anisotropic critical state plasticity. *Int. J. Numer. Anal. Methods Geomech.* 40, 2423–2449.
- Shi, S., Zhang, F., Feng, D., Lin, C., 2023. Investigation of mechanical properties and elastoplastic numerical calculation model of frozen soil containing ice lenses. *Cold Reg. Sci. Technol.* 210, 103843.
- Stuuroop, J.C., van der Zee, S.E.A.T.M., Voss, C.I., French, H.K., 2021. Simulating water and heat transport with freezing and cryosuction in unsaturated soil: Comparing an empirical, semi-empirical and physically-based approach. *Adv. Water Resour.* 149, 103846.
- Sweidan, A.H., Niggemann, K., Heider, Y., Ziegler, M., Markert, B., 2022. Experimental study

and numerical modeling of the thermo-hydro-mechanical processes in soil freezing with different frost penetration directions. *Acta Geotech.* 17, 231–255.

Teng, J., Liu, J., Zhang, S., Sheng, D., 2020. Modelling frost heave in unsaturated coarse-grained soils. *Acta Geotech.* 15, 3307–3320.

Teng, Y.C., Teng, Z.C., Liu, Y., Liu, X.Y., Zhou, Y.D., Liu, J.L., Li, B., 2022. A review of the research on thermo-hydro-mechanical coupling for the frozen soil. *Geofluids* 2022.

Thomas, H.R., Cleall, P., Li, Y.-C., Harris, C., Kern-Luetschg, M., 2009. Modelling of cryogenic processes in permafrost and seasonally frozen soils. *Geotechnique* 59, 173–184.

Van Genuchten, M.T., 1980. A closed-form equation for predicting the hydraulic conductivity of unsaturated soils. *Soil Sci. Soc. Am. J.* 44, 892–898.

Vasiliev, A.A., Drozdov, D.S., Gravis, A.G., Malkova, G. V, Nyland, K.E., Streletskiy, D.A., 2020. Permafrost degradation in the western Russian arctic. *Environ. Res. Lett.* 15, 045001.

Vitel, M., Rouabhi, A., Tijani, M., Guérin, F., 2015. Modeling heat transfer between a freeze pipe and the surrounding ground during artificial ground freezing activities. *Comput. Geotech.* 63, 99–111.

Vosoughian, S., Balieu, R., 2023. Thermo-mechanical simulation of frost heave in saturated soils. *Front. Struct. Civ. Eng.* 17, 1400–1412.

Wang, B., Paudel, B., Li, H., 2016. Behaviour of retrogressive thaw slumps in northern Canada—three-year monitoring results from 18 sites. *Landslides* 13, 1–8.

Wang, L., Marzahn, P., Bernier, M., Ludwig, R., 2020. Sentinel-1 InSAR measurements of

- deformation over discontinuous permafrost terrain, Northern Quebec, Canada. *Remote Sens. Environ.* 248, 111965.
- Wang, M., Li, X., Xu, X., 2021. An implicit Heat-Pulse-Probe method for measuring the soil ice content. *Appl. Therm. Eng.* 196, 117186.
- Wang, S., Lv, Q., Baaj, H., Li, X., Zhao, Y., 2016. Volume change behaviour and microstructure of stabilized loess under cyclic freeze–thaw conditions. *Can. J. Civ. Eng.* 43, 865–874.
- Wu, Y., Ishikawa, T., 2022. Thermal-Hydro-Mechanical coupled analysis of unsaturated frost susceptible soils. *Res. Cold Arid Reg.* 14, 223–234.
- Xu, X., Li, Q., Lai, Y., Pang, W., Zhang, R., 2019. Effect of moisture content on mechanical and damage behavior of frozen loess under triaxial condition along with different confining pressures. *Cold Reg. Sci. Technol.* 157, 110–118.  
<https://doi.org/https://doi.org/10.1016/j.coldregions.2018.10.004>
- Xu, X., Wang, Y., Yin, Z., Zhang, H., 2017. Effect of temperature and strain rate on mechanical characteristics and constitutive model of frozen Helin loess. *Cold Reg. Sci. Technol.* 136, 44–51.
- Yan, Z., Pan, W., Fang, J., Liu, Z., 2020. Numerical simulation of thawing process in frozen soil. *Geofluids* 2020, 1–7.
- Yang, H., Zhou, Z., Wang, X., Zhang, Q., 2015. Elastic modulus calculation model of a soil-rock mixture at normal or freezing temperature based on micromechanics approach. *Adv. Mater. Sci. Eng.* 2015. <https://doi.org/10.1155/2015/576080>

- Yang, S., Wang, L.L., Stathopoulos, T., Marey, A.M., 2023. Urban microclimate and its impact on built environment—a review. *Build. Environ.* 238, 110334.
- Yin, X., Lai, Y., Liu, E., 2023. Microstructure-based effective stress for unsaturated frozen soils. *Int. J. Numer. Anal. Methods Geomech.* 47, 261–274.
- Young, N.L., Lemieux, J., Delottier, H., Fortier, R., Fortier, P., 2020. A conceptual model for anticipating the impact of landscape evolution on groundwater recharge in degrading permafrost environments. *Geophys. Res. Lett.* 47, e2020GL087695.
- Yu, F., Guo, P., Na, S., 2022. A framework for constructing elasto-plastic constitutive models for frozen and unfrozen soils. *Int. J. Numer. Anal. Methods Geomech.* 46, 436–466.
- Zhang, D., Liu, E., Yu, D., 2020. A micromechanics-based elastoplastic constitutive model for frozen sands based on homogenization theory. *Int. J. Damage Mech.* 29, 689–714.
- Zhang, G., Liu, E., Chen, S., Song, B., 2019. Micromechanical analysis of frozen silty clay-sand mixtures with different sand contents by triaxial compression testing combined with real-time CT scanning. *Cold Reg. Sci. Technol.* 168, 102872.
- Zhang, Y., Michalowski, R.L., 2015. Thermal-hydro-mechanical analysis of frost heave and thaw settlement. *J. Geotech. geoenvironmental Eng.* 141, 4015027.
- Zheng, B., Zhang, J., Qin, Y., 2010. Investigation for the deformation of embankment underlain by warm and ice-rich permafrost. *Cold Reg. Sci. Technol.* 60, 161–168.
- Zheng, T., Miao, X.-Y., Naumov, D., Shao, H., Kolditz, O., Nagel, T., 2019. A thermo-hydro-mechanical finite-element model with freezing processes in saturated soils. *Environ.*

Geotech. 9, 502–514.

Zhou, M.-M., Meschke, G., 2018. A multiscale homogenization model for strength predictions of fully and partially frozen soils. *Acta Geotech.* 13, 175–193.

Zhou, M.M., Meschke, G., 2013. A three-phase thermo-hydro-mechanical finite element model for freezing soils. *Int. J. Numer. Anal. methods Geomech.* 37, 3173–3193.

Zhu, Z., Jia, J., Zhang, F., 2020. A damage and elastic-viscoplastic constitutive model of frozen soil under uniaxial impact loading and its numerical implementation. *Cold Reg. Sci. Technol.* 175, 103081.

Zienkiewicz, O.C., Shiomi, T., 1984. Dynamic behaviour of saturated porous media; the generalized Biot formulation and its numerical solution. *Int. J. Numer. Anal. methods Geomech.* 8, 71–96.

Zimmerman, R.W., 1984. Elastic moduli of a solid with spherical pores: new self-consistent method, in: *International Journal of Rock Mechanics and Mining Sciences & Geomechanics Abstracts*. Elsevier, pp. 339–343.